

STUDY OF LOCALIZED SURFACE PLASMON AND
GRATING-COUPLED SURFACE PLASMON ENHANCED
PHOTOELECTROCATALYTIC ELECTRODE AND
ORGANIC PHOTOVOLTAICS

SUPEERA NOOTCHANAT

Doctoral Program in Electrical and Information Engineering
Graduate School of Science and Technology
Niigata University

ABSTRACT

This dissertation demonstrates the usage of localized surface plasmon (LSPR) and grating-coupled surface plasmon resonance (GCSPR) to enhance the photocatalytic activity of a thin film photocatalyst, particularly TiO_2 (P25), and the performance of thin film organic photovoltaic. In the first study, we show the improvement of the photocurrent of the TiO_2 photocatalyst film in water splitting reaction by using localized surface plasmon of gold nanoparticles. We prepared plasmonic gold nanoparticle (AuNP)- TiO_2 nanocomposite and deposited on transparent-conductive electrode (indium-tin-oxide (ITO) coated glass) to obtain AuNP- TiO_2 nanocomposite photoelectrocatalytic (PEC) electrode with the thickness of ~ 460 nm. The photocurrent that originates from the water-splitting reaction catalyzed by LSPR of the gold nanoparticles affected the generation of photocurrent by TiO_2 upon illumination with visible light was systematic measured. Using electrochemical impedance spectroscopy (EIS), the results suggest that the improvement in the photocurrent generation creates from an enhancement in electron-hole pair generation, which induced by the LSPR of the plasmonic gold nanoparticles, rather than the extension of the electron lifetime. Moreover, we not only show the effect of LSPR in enhancement of the photocurrent of TiO_2 under visible illumination but also introduced a new method to enhance the photocurrent of TiO_2 by a multiple plasmonic effect, i.e., the cooperation of LSPR of plasmonic gold nanoparticles and the GCSPR of a gold grating. For the second study, we emphasize on the improvement of the photocurrent and the photo-electricity conversion efficiency of thin film P3HT:PCBM solar cells by GCSPR. The Blu-ray disc recordable (BD-R) and Blu-ray disc (BD) grating pattern ($\Lambda = 330$ nm) were created on the active layer of the solar cell using pressure-less nanoimprinting technique, following by thermal evaporation of aluminum to obtain the BD-R and BD grating back electrode. The surface plasmon (SP) reflectivity curves of the fabricated solar cell reveal the decrease of the reflection spectra of the solar cells with BD-R and BD grating compare with the flat device. This can be implied to the increase of the trapped light in the device due to the BD and BD-R grating structures that can be assigned to two regions included (i) the increase of the light trapping at 400 – 650 nm attributed to the light scattering effect. (ii) The irradiation photon can be coupled into GCSPR that propagates along the surface of the diffraction grating which can be observed as the occurrence of the dip peaks at the wavelength longer than 650 nm. The I-V characterization results show the improvement of photocurrent about 10% and 5.6% for the BD-R and BD solar cell, respectively. Moreover, the enhancement of the photoconversion efficiency of 19.3% can be obtained from BD-R

solar cell while those of solar cell with BD grating can be improve the photoconversion efficiency of 3.2% compared to flat solar cell.

KEYWORDS: gold nanoparticles, titanium dioxide, P25, nanocomposite, gold grating grating-coupled surface plasmon resonance, organic photovoltaic, organic solar cell, nanoimprinting, P3HT:PCBM, BD-R, BD, diffraction grating.

ACKNOWLEDGMENTS

This dissertation has been completed under the precious supervision of kind research staffs. First of all, I gratefully appreciate my thesis advisors, Associate Professor Dr. Akira Baba and Associate Professor Dr. Sanong Ekgasit, for kind-precious suggestions all the way through this work. Not less important than above, I would like to express my grateful thank to Professor Dr. Futao Kaneko, Professor Dr. Keizo Kato, Professor Dr. Kazunari Shinbo, from Niigata University and Associate Professor Chuchaat Thammacharoen from Chulalongkorn University for their valuable advice and support.

My thanks are given to my friends, my colleagues at research units, included Center for Transdisciplinary Research, Niigata University and Sensor Research Unit, Chulalongkorn University, for precious suggestion and helpful supports on this research.

I would like to thank Global Circus Program from Japan Society for the Promotion of Science (JSPS), Graduate School of Science and Technology Niigata University, National Research Council of Thailand (NRCT), Center of Innovation Nanotechnology Chulalongkorn University (CIN CU), Development and Promotion of Science and Technology Talents Project (DPST) for financial supports.

Last but not least, I deeply appreciate my father, my mother, charming family, and my special persons as they raise me up every time when I fall down with their precious loves understanding, support, and encouragement all the way through this work and my life.

SUPEERA NOOCHANAT

CONTENTS

	Page
ABSTRACT.....	ii
ACKNOWLEDGMENTS.....	iv
CONTENTS.....	v
LIST OF FIGURE.....	vii
LIST OF ABBREVIATIONS.....	xi
CHAPTER I	
INTRODUCTION	
1.1 RESEARCH BACKGROUND AND RATIONALE.....	
1.1.1 Titanium dioxide (TiO ₂)	1
1.1.2 Gold nanoparticles synthesis and their applications.....	2
1.1.3 Localized surface plasmon resonance (LSPR).....	6
1.1.4 Grating-coupled surface plasmon resonance (GCSPR).....	8
1.1.5 Thin film organic solar cell.....	9
1.2 OBJECTIVES.....	13
1.3 SCOPE OF THE DISSERTATION.....	13
CHAPTER II	
Investigation of localized surface plasmon/grating-coupled surface plasmon enhanced photocurrent in TiO₂ thin films.	
ABSTRACT.....	21
INTRODUCTION.....	21
EXPERIMENTAL.....	22
RESULTS AND DISCUSSION.....	24
CONDLUSIONS.....	36
ACKNOWLEDGEMENT.....	37
REFERENCES.....	37

CHAPER III**Grating-coupled SPR Enhanced NIR Activities of Organic Photovoltaic Devices****Originated by BD-R and BD grating structures.**

ABSTRACT.....	42
INTRODUCTION.....	42
EXPERIMENTAL.....	44
RESULTS AND DISCUSSION.....	45
CONDLUSIONS.....	58
ACKNOWLEDGEMENT.....	59
REFERENCES.....	59

CHAPER IV

CONCLUSIONS.....	62
SUGGESTIONS FOR FUTURE WORK.....	63
APPENDICES.....	64
APPENDIX A.....	65
APPENDIX B.....	70
VITAE.....	81

LIST OF FIGURES

Figure	Page
CHAPTER I	
INTRODUCTION	
1. Figure 1 Crystalline TiO ₂ with different polymorph (A) anatase, (B) rutile, and (C) brookite.	1
2. Figure 2 Schematic illustrate the photoinduced charge carrier species on TiO ₂ particles after irradiation by UV light.	2
3. Figure 3 (A) A 5 L batch of gold nanosheets. (B) A close-up digital photograph shows the glittering effect of the gold nanosheets. (C, D) Micrographs of the gold nanosheets under illuminations of bright field and dark field, respectively. (E–G) SEM images of the mass-scale produced gold nanosheets.	3
4. Figure 4 (A) Raman spectra of crystal violet deposited on a gold nanosheet. The Raman spectra were recorded with and without a tip. (B) The Raman spectrum of crystal violet.	4
5. Figure 5 UV–visible extinction of the AuNPs with different concentration at (A) 1000 ppm, (B) 500 ppm, and (C) 200 ppm in the present of milk protein with the concentration of with 2.93×10^{-4} to 2.93 mg/mL. The dashed line shows the original UV–visible extinction of AuNPs.	5
6. Figure 6 The diagram demonstrating of (A) the propagated surface plasmon and (B) the localized surface plasmon.	6
7. Figure 7 The calculated spectra of scattering (blue line), absorption (red line), and extinction (black line) of Ag nanoparticles with different shapes comprised of (A) a sphere (B) a cube, (C) a tetrahedron, (D) an octahedron, and (E) a triangular plate. (F) Extinction spectra of the rectangular bars with different aspect ratios: 2 (black line), 3 (red line), and 4 (blue line). Note that the non-spherical particles typically show multiple, red-shifted resonance peaks.	7
8. Figure 8 Diagram illustrated the diffraction of light by a diffraction grating.	9

9. Figure 9 (A) common type solar cells with single-junction structure, (B) inverted type solar cells with single-junction structure, and (C) common type tandem solar cells with multi-junction structure. 9
10. Figure 10 The examples of chemical structures of (A) polymer donors and (B) fullerenes acceptors used for making of the active layer of thin film organic solar cells. 10
11. Figure 11 (A) The schematic of the photoinduced charge transfers of donor polymer to fullerene acceptor. (B) The energy level diagram. After excitation, the electron is transferred to the C60 induced by electron affinity of C60. 11
12. Figure 12 I-V characteristic of a thin film organic solar cell. The dashed line and the dark line represent I-V curves without and with illuminated, respectively 12

CHAPTER II

Investigation of localized surface plasmon/grating-coupled surface plasmon enhanced photocurrent in TiO₂ thin films

1. Figure 1 TEM images of (A) TiO₂ and (B) AuNP–TiO₂ nanocomposites with 0.5% of Au–TiO₂. The scale bars in (A) and (B) indicate 20 nm. The arrows indicate AuNPs on the TiO₂ surfaces. (C) Digital photograph and (D) UV-visible absorption spectra of AuNP–TiO₂ nanocomposites with various Au–TiO₂ ratios. 26
2. (A) Short-circuit photocurrent and (B) I–V characteristics of TiO₂ and AuNP–TiO₂ nanocomposites with 0.5% Au–TiO₂ with and without white light illumination. (C) Relationship between short-circuit photocurrent and the loading amount of gold nanoparticles in the nanocomposites. 28
3. Figure 1 Short-circuit photocurrent of AuNP–TiO₂ nanocomposites with various amounts of gold nanoparticles upon irradiation with the wavelengths (A) 400 nm and (B) 530–700 nm. 29
4. Figure 4 Nyquist plots for the TiO₂ photocatalyst electrode under white light illumination. The inset shows the equivalence circuit model obtained from the Nyquist curve fitting. 30

5. Figure 5 (A) Nyquist plot and (B) Bode phase plot for AuNP-decorated TiO₂ nanocomposite photocatalyst electrodes with various loading amounts of gold nanoparticles under illumination with white light.. 30
6. Figure 2 SPR reflectivity curves of the bare gold grating irradiated with (A) s-polarization and (B) p-polarization. SPR reflectivity curves of (C) TiO₂–gold grating photocatalyst electrode and (D) AuNP–TiO₂ nanocomposites/gold grating photocatalyst electrode irradiated with p-polarization. 33
7. Figure 3 (A) Short-circuit photocurrent TiO₂–gold grating irradiated by white light with s- and p-polarization. (B) Schematic representation of the fabricated TiO₂–gold grating. 35
8. Figure 4 The short-circuit photocurrent of TiO₂–flat gold, TiO₂–gold grating, and AuNP–TiO₂ nanocomposite/gold grating irradiated by white light with p-polarization. 36

CHAPER III

Grating-coupled SPR Enhanced NIR Activities of Organic Photovoltaic Devices

Originated by BD-R and BD grating structures.

1. Figure 5 AFM micrographs of the surface of P3HT:PCBM film of (A) flat solar cell, (C) solar cell imprinted with BD-R grating pattern, and (E) solar cell imprinted with BD grating pattern. The AFM images of the surface of Al back electrode of (B) flat solar cell, (D) solar cell with BD-R grating pattern, and (F) solar cell with BD grating pattern. 47
2. Figure 6 The SPR reflectivity curves and its schematic represented the structure of the fabricated solar cells with (A) flat solar cell (B) BD-R solar cell (C) BD solar cell. spectra were collected from ITO side under irradiation of p-polarized light. 50
3. Figure 7 I-V characteristic and the schematic of the fabricated solar cells under illumination of non-polarized light with normal incident angle. 51
4. Figure 8 Relationships of (A) short-circuit photocurrent (J_{sc}) and incident angle and (B) photoconversion efficiency (PCE) and incident angle of the fabricated solar cells. The solar cells were illuminated with non-polarized light during electrical characterization. 51

5. Figure 9 P/S enhancement factors of the fabricated devices. The enhancement factor is the ratio of the short-circuit photocurrent under illumination of p-polarized light to the short-circuit photocurrent under illumination of s-polarized light. 52
6. Figure 10 IPCE enhancement spectra of (A) BD-R solar cell and (B) BD solar cell under illumination of non-polarized light. The IPCE enhancement is the ratio of the IPCE of imprinted device to the IPCE of the flat device. 54
7. Figure 11 IPCE enhancement spectra P/S of (A) flat solar cell, (B) BD-R solar cell, and (C) BD solar cell. The IPCE enhancement p/s is the ratio between the IPCE with the SP excitation (p-polarization) and without SP excitation (s-polarization). 54
8. Figure 8 IPCE spectra of the BD and flat solar cells irradiated with non-polarized light at the incident angle of (A) 0° and (B) 20°. 55
9. Figure 9 IPCE spectra of the BD-R and flat solar cells irradiated with non-polarized light at the incident angle of (A) 0° and (B) 20°. 56
10. Figure 10 IPCE spectra of (A) flat solar cell, (B) BD solar cell, and (C) BD-R solar cells under illumination of polarized light at the incident angle of 20°. The arrow in (C) indicates the increase of the IPCE enhancement by GCSPR. 57

LIST OF TABLES

CHAPTER II

Investigation of localized surface plasmon/grating-coupled surface plasmon enhanced photocurrent in TiO₂ thin films

- | | Page |
|--|------|
| 1. Table 1 EIS parameters for AuNP-decorated TiO ₂ nanocomposites | 31 |

CHAPTER III

Grating-coupled SPR Enhanced NIR Activities of Organic Photovoltaic Devices Originated by BD-R and BD grating structures.

- | | |
|--|----|
| 1. Table 1 The percentage of integration area calculated from the IPCE spectra of the fabricated devices under illumination of polarized light at the incident angle of 20°. | 58 |
|--|----|

LIST OF ABBREVIATIONS

LSPR	Localized surface plasmon resonance
GCSPR	Grating-coupled surface plasmon resonance
AuNP	Gold nanoparticle
ITO	Indium-tin-oxide
PEC	Photoelectrocatalytic
EIS	Electrochemical impedance spectroscopy
SPR	Surface plasmon resonance
BD-R	Blu-ray disc recordable
BD	Blu-ray disk
SP	Surface plasmon
UV	Ultraviolet
AuNPs	Gold nanoparticles
SERs	Surface-enhanced Raman spectroscopy
TERs	Tip-enhanced Raman spectroscopy
NP	Nanoparticles
SPP	Surface plasmon polariton
BHJ	Bulk heterojunction
PCE	Photoconversion efficiency
CT	Charge transfer
I-V	Current-voltage
PRET	Plasmon resonance energy transfer
DI-water	Deionized water
TEM	Transmission electron microscope
IEP	Isoelectric point
IPCE	Photo to current conversion efficiency

CHAPTER I

INTRODUCTION

RESEARCH BACKGROUND

1. Titanium dioxide

Titanium dioxide (TiO_2) is a well-known photocatalyst due to its chemical stability and low cost. In general, there are three main polymorphs of natural crystalline TiO_2 , consisted of anatase (tetragonal), rutile (tetragonal), and brookite (orthorhombic). Figure 1 shows the crystal structure of three main polymorphs of TiO_2 . The differences of the three crystal structure are distortion of the octahedral structure and the assembly form of the octahedral units. For the anatase, the structure is built up from the connection of octahedral vertices while the structure of rutile is constructed form the connection octahedral edges. For brookite, the structure is constructed by the connection of both vertices and edges of octahedral [1].

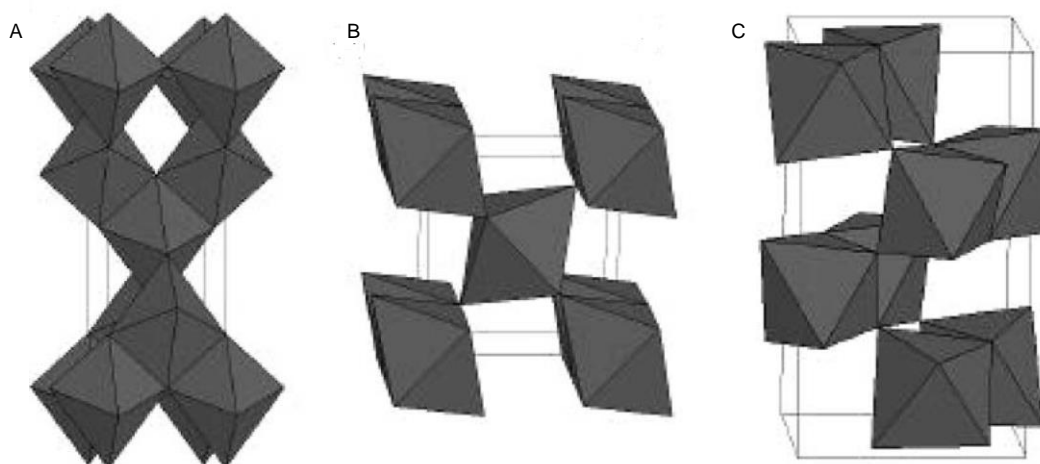


Figure 12 Crystalline TiO_2 with different polymorph (A) anatase, (B) rutile, and (C) brookite [1].

For photocatalyst applications, P-25, which is the combination between 70–80% of the anatase phase and 20–30% of the rutile phase, is the famous TiO_2 used for photocatalyst application [2, 3]. The size of P-25 is typically 20 nm. Figure 2 shows the diagram indicated the generation of charge carrier species of TiO_2 upon irradiation by ultraviolet (UV) light. The photoinduced charge carrier species are generated upon the absorption of energetic

photons with the energy equivalent to the band gap of TiO_2 . The photoinduced holes move to the surface of TiO_2 particles and consecutively react with water molecules on the surfaces of TiO_2 , resulting the generation of hydroxyl radicals ($\cdot\text{OH}$) which is a strong oxidizer. Both hydroxyl radicals and holes are strong oxidizer that can oxidize organic molecule on the surface of TiO_2 . In the meantime, photoinduced electrons can also play as a reducer by reacting with the oxygen molecules on the surface of TiO_2 to form superoxide radical anions ($\text{O}_2^{\cdot-}$) [4].

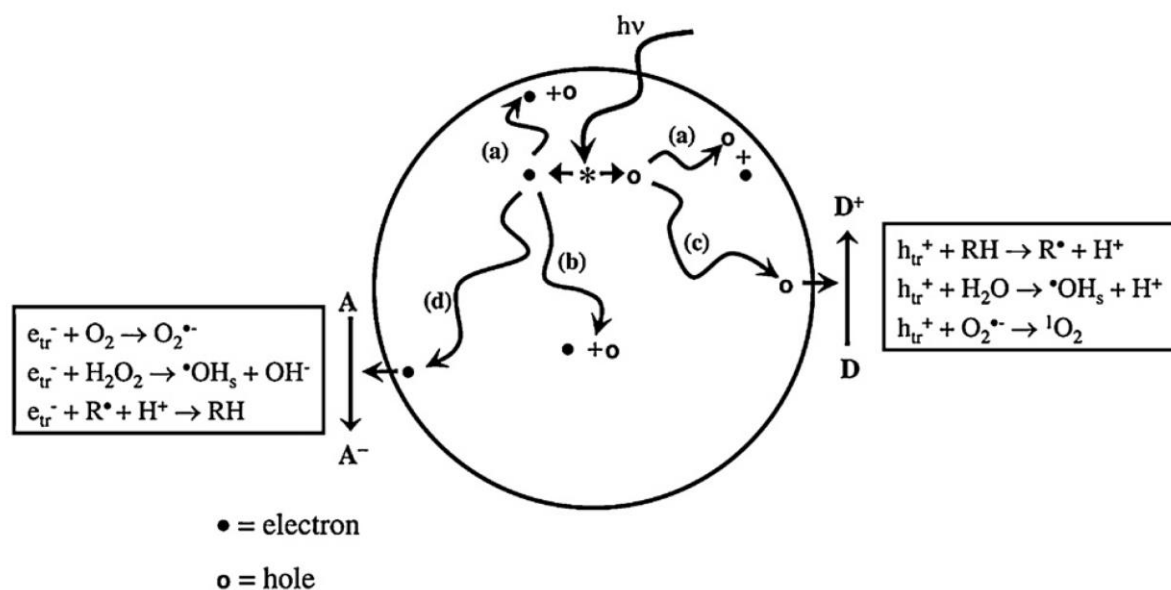


Figure 13 Schematic illustrate the photoinduced charge carrier species on TiO_2 particles after irradiation by UV light [4].

2. Gold nanoparticles synthesis and their applications

Gold nanoparticles (AuNPs) are the zero-valent gold particles with the particle size smaller than 100 nm at least one dimension. It has been laid on the field of interest of many researchers for several years due to its size- and shape- dependent properties which can be applied to potent applications [5], such as catalyst [6], colorimetric sensor [7-11], surface-enhanced Raman spectroscopy (SERS) [12-14], and Tip-enhanced Raman spectroscopy (TERS) [15, 16]. Numerous synthesis methods aiming to control the morphology AuNPs have been proposed. In addition, the reducing power of a reducing agent and the action of a stabilizer play an important role in the solution phase synthesis. Carefully selection of reducers and stabilizers are necessary to obtain AuNPs with different morphology, for example flower [17], icosahedral [18, 19], octahedral [20], rod [21-23], star [24], and plate [25-27]. Among of those synthesis approaches, Turkevich method, which was invented in 1953 by John Turkevich and co-workers, is widespread used to prepare red-wine color

AuNPs. In this method, aurochloric acid (HAuCl_4) was reduced by sodium citrate at $100\text{ }^\circ\text{C}$. The colloidal gold with spherical shape was obtained. The average size of AuNPs is about 20 nm [28]. This method was revisited again in 2006 by Kimling and co-workers [29]. It was found that the size and the optical extinction of AuNPs could be tuned by changing of the concentration ratios of gold ions versus citrate.

In consideration of environmental pollutions, the green synthesis approaches have been invented in order to prepare metal nanostructures without using of harmful chemicals. Pienpinijtham and co-workers have reported the method for the preparation of AuNPs using starch as a reducing agent and stabilizer [15, 30]. The reducing power of starch was promote by incubation of starch in an alkaline solution which cause the formation of reducing species (aldehyde or α -hydroxy ketone). The size of AuNPs can be adjusted form nanometer to submicron range with narrow size distribution by changing of pH of the solution. Nootchanat and co-workers have reported the synthesis procedure to prepare gold nanosheets by using starch as a stabilizer and H_2O_2 as a green reducing agent [31]. The size of the nanosheets is approximately $8\text{ }\mu\text{m}$ while its thickness is about 50 nm. The size of the nanosheets can be adjusted by changing the concentration of the H_2O_2 . This method can be used for an industrial-scale production as it can produce large amount of gold nanosheets without generation of toxic waste as shown in Figure 3. Due to the atomic flat surfaces, the gold nanosheets can be used as the substrate for SERs as well as the shining-glittering pigment in an ink for precious art works.

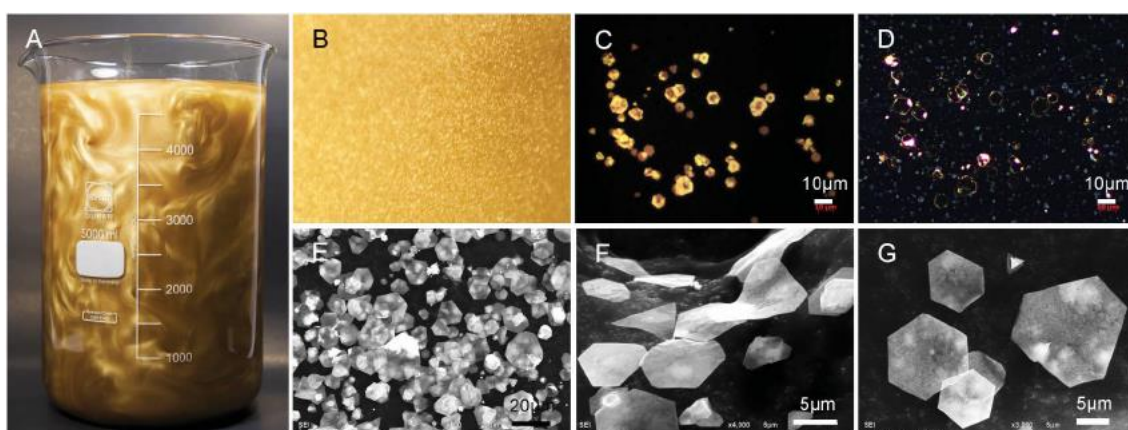


Figure 14 (A) A 5 L batch of gold nanosheets. (B) A close-up digital photograph shows the glittering effect of the gold nanosheets. (C, D) Micrographs of the gold nanosheets under illuminations of bright field and dark field, respectively. (E–G) SEM images of the mass-scale produced gold nanosheets [31].

For chemical identification application, the sample with trace amount needs a powerful characterization technique that provides the information about chemical structure or functional groups. Tip enhanced Raman spectroscopy (TERS) is not only powerful techniques for trace analysis providing the chemical structure information but also the ability to select the characterization area. Pienpinijtham and co-workers have showed the benefit of using gold nanosheets as a substrate for TERS of crystal violet molecules (Figure 4 [15]). Using of gold nanosheet provides two advantages: i) a target molecule can absorb on the surface of gold nanosheets via Au-S bonding. ii) The hot spot is generated between the metal tip and surface of the gold nanosheet which give a better enhancement factor.

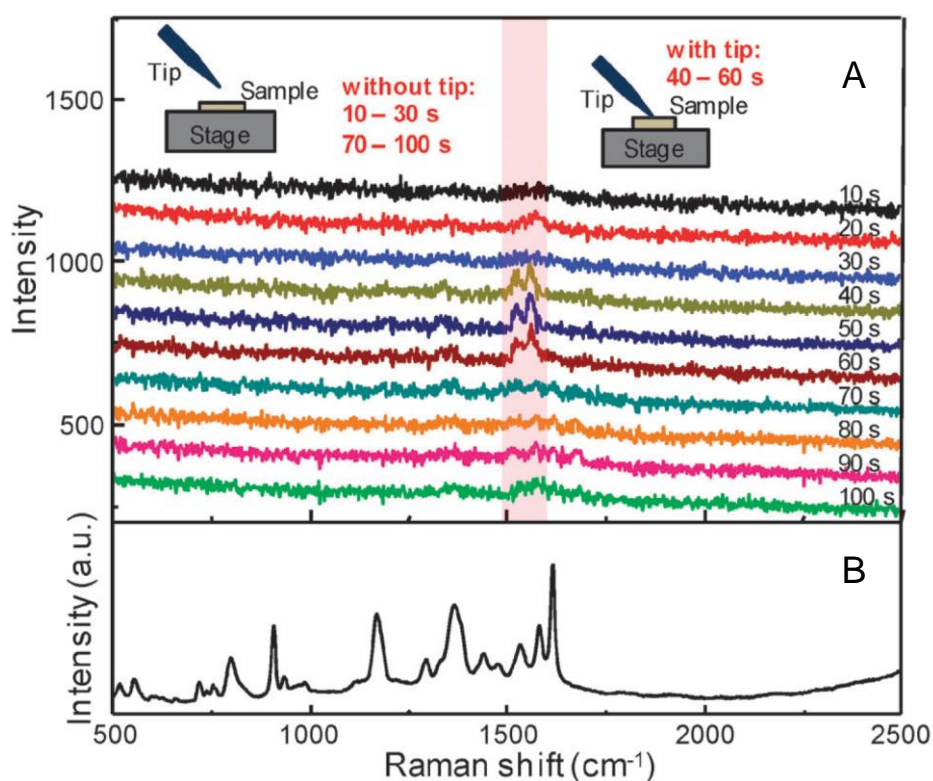


Figure 15 (A) Raman spectra of crystal violet deposited on a gold nanosheet. The Raman spectra were recorded with and without a tip. (B) The Raman spectrum of crystal violet [15].

As mention above, AuNPs provide the promising properties that suitable for sensor applications. One of those properties is changing of color inducing by aggregation of AuNPs. Vantasin and co-workers introduced the naked-eye-observable-colorimetric sensor for specification of amount of protein in milk using AuNPs [32]. The sensor is working on the principle that the stabilization power of proteins in milk can prevents the aggregation of AuNPs which is induced by hydrochloric acid. With the occurrence of milk protein, the color of AuNPs undergoes shifting from red to blue when the concentration of protein in milk decreases. This is because of the change of the degree of aggregation of AuNPs, resulting in

the change of the localized surface plasmon resonance (LSPR) excitation wavelength. Thus, the colorimetric sensor that sensitives to protein amount in milk is obtained as shown in Figure 5.

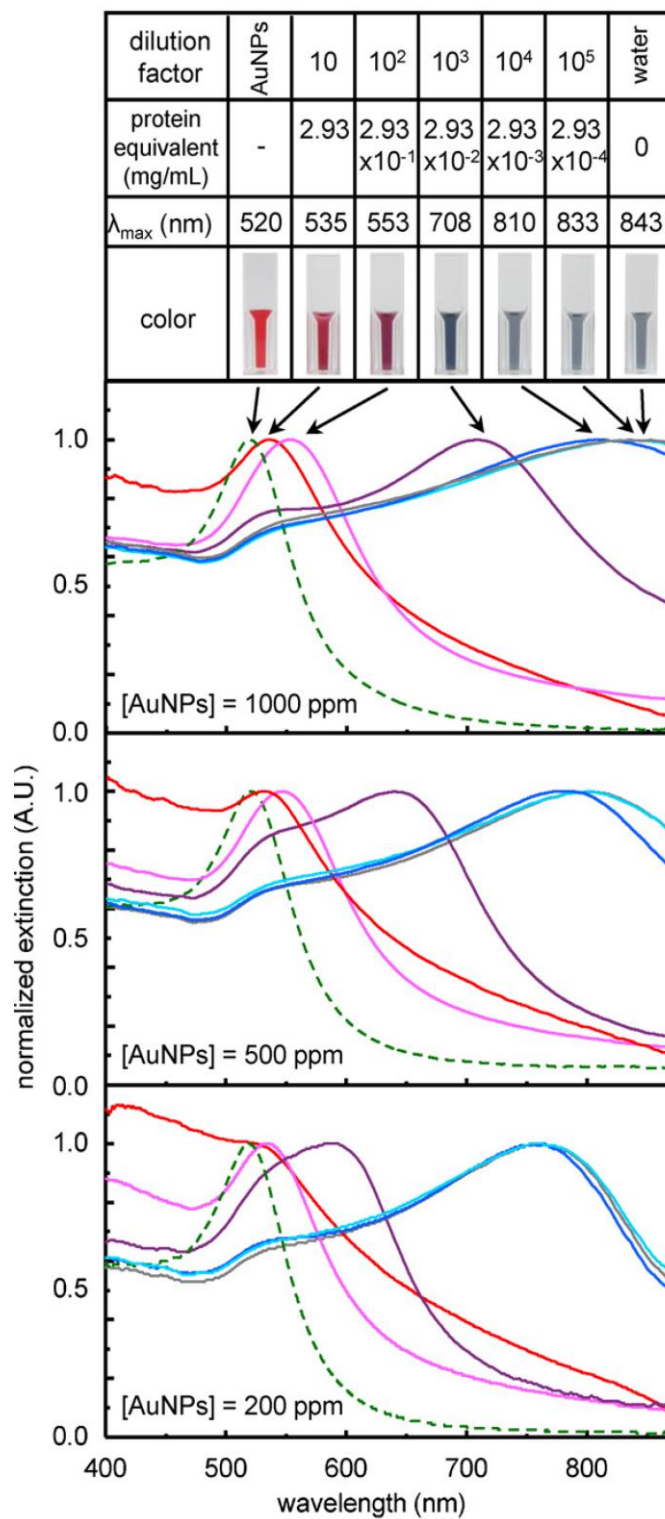


Figure 16 UV–visible extinction of the AuNPs with different concentration at (A) 1000 ppm, (B) 500 ppm, and (C) 200 ppm in the present of milk protein with the concentration of with

2.93×10^{-4} to 2.93 mg/mL. The dashed line shows the original UV–visible extinction of AuNPs [32].

3. Localized surface plasmon resonance

LSPR is a wave trapping phenomenon by metal nanoparticles with the size smaller than the wavelength of light. The LSPR is generated from the interaction between the electrons on the surfaces of metal nanoparticles and the incident light wave, Figure 6. This interaction generates the collective oscillation electron with resonance frequency against incoming light wave, resulting in some photons absorption and some photons scattering called extinction. This phenomenon strongly depends on the geometry of nanoparticle and surrounded environment, for example size, geometry, dielectric environment and inter-particle distance. Noble metal nanoparticles, such as Ag and Au, provide LSPR excitation in the visible region [33].

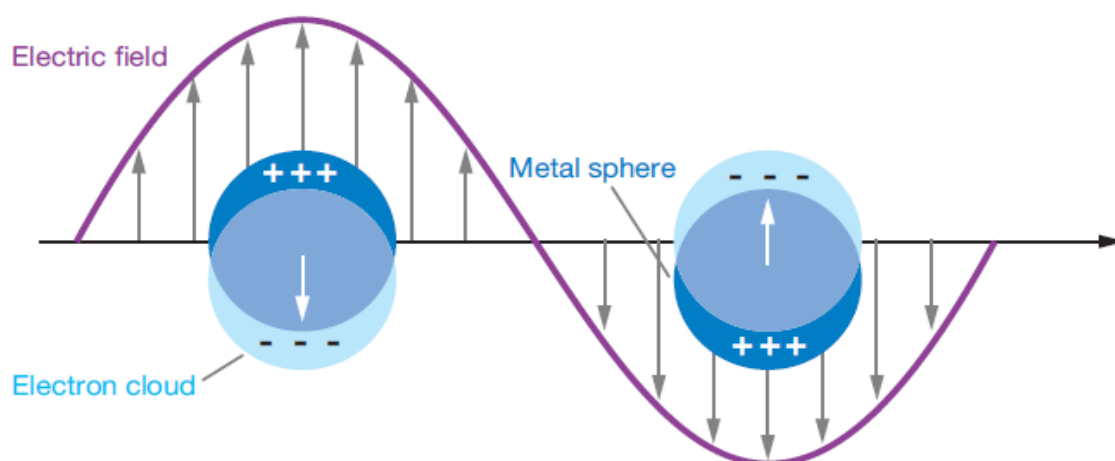


Figure 17 The diagram demonstrating of (A) the propagated surface plasmon and (B) the localized surface plasmon [34].

Besides, the size and shape of plasmonic nanoparticles affect the LSPR properties because of the difference of the surfaces polarization. Numerous synthesis approaches aiming to control the size and shapes, such as nanosphere [2] nanoring [3], octahedrons [4], nanorods [5], nanostar [6], and nanosheets [7], have been investigated in order to selectively fine-tune the LSPR spectra of those nanoparticles. Figure 7 shows the calculated spectra of Ag nanoparticles with different shape and size. The results reveal that plasmonic Ag nanoparticles with different shape have different spectrum. Upon LSPR excitation, the electric field of the incident light wave interacts with the electron cloud at the surface of nanoparticles cause the formation of polarization. The different geometry of the plasmonic

nanoparticles affects the different distribution of polarization in several ways as followed. i) The redshift of LSPR spectra can be obtained by the increase of edges or sharpness which increases the charge separation. ii) The increase of the symmetry can raise LSPR intensity. iii) The number of polarized modes determines the number of LSPR peaks. iv) the scattering effect of nanoparticles increase with the increase of particle size [33].

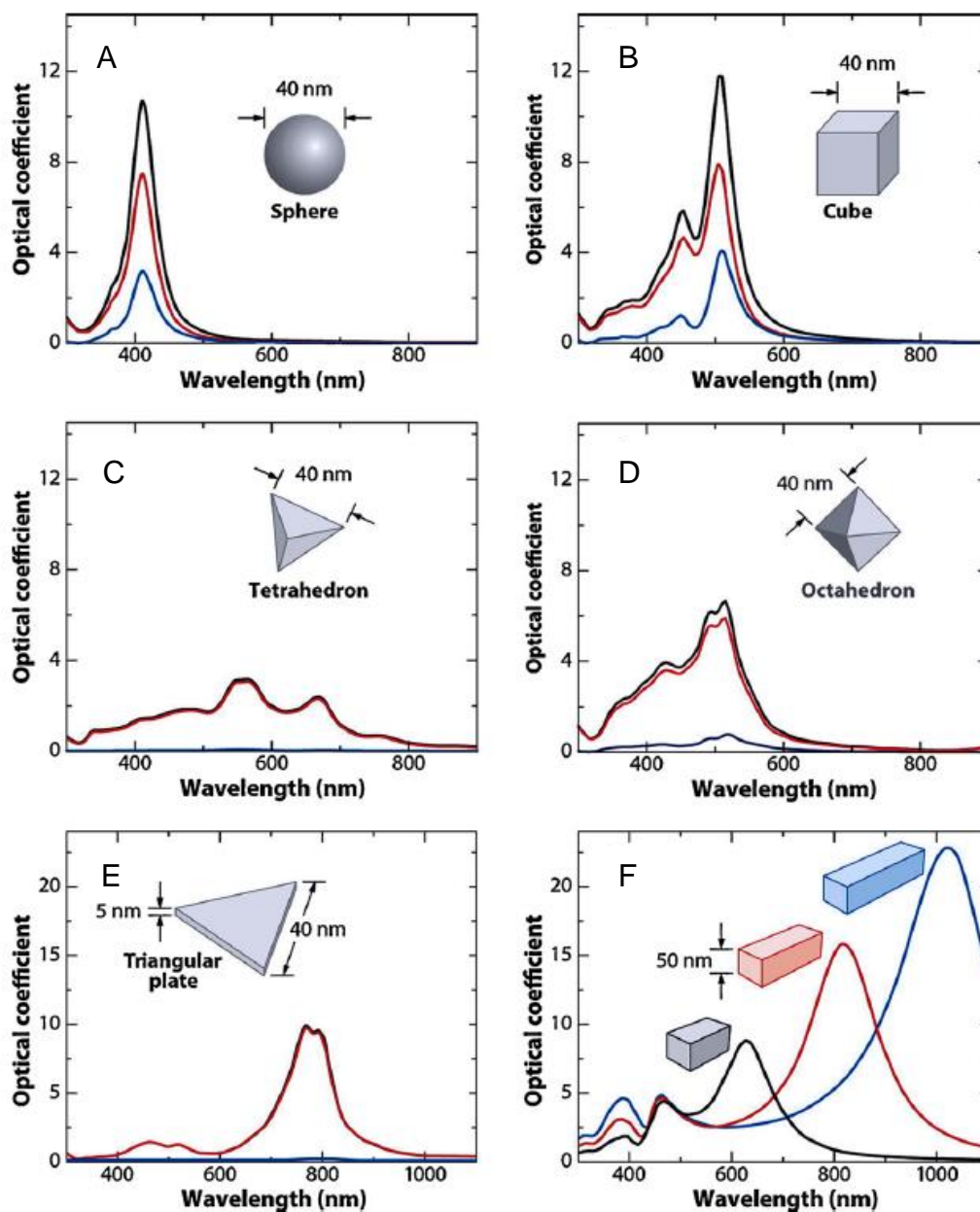


Figure 18 The calculated spectra of scattering (blue line), absorption (red line), and extinction (black line) of Ag nanoparticles with different shapes comprised of (A) a sphere (B) a cube, (C) a tetrahedron, (D) an octahedron, and (E) a triangular plate. (F) Extinction spectra of the rectangular bars with different aspect ratios: 2 (black line), 3 (red line), and 4

(blue line). Note that the non-spherical particles typically show multiple, red-shifted resonance peaks [33].

4. Grating-coupled surface plasmon

SP (in addition it should be called surface plasmon polaritons, SPP) are propagated waves that travel along the conductor surfaces. In general, light waves can be trapped on the surface on the conductor by the interaction between the free electrons on the surface of the conductor. These free electrons undergo collective oscillation in resonance with the incoming light wave. This resonant creates the SP [35].

The GCSP is a convenient method that provides propagating SP excitation without using of prism [36, 37]. In the beginning of the twentieth century, Wood has described the occurrence of irregular light diffraction on diffraction gratings that is caused by the excitation of surface plasma waves [38]. Upon the irradiation on the diffraction grating surface, the incident light beam is split into several reflected beams by the surface of the periodic corrugate structure, Figure 8 [39]. With the appropriate condition (i.e. the grating grooves perpendicularly stand on the plane of incidence and the momentum of diffracted light is raised to equivalent to the propagation constant of the SP), the SP can be occurred by coupling of the diffracted light. The coupling condition may be written as the follow equation:

$$\frac{2\pi}{\lambda}n_d \sin \theta + m\frac{2\pi}{\Lambda} = \pm \text{Re}\{\beta^{\text{SP}}\}$$

where λ is the grating period, m is numbers representing the diffraction order of the diffracted light, β^{SP} is the propagation constant of SP, Re is the real part of a complex number, and n is the refractive index. After the occurrence of the grating-coupled SP excitation, some amount of the energy of the incident wave is used and transformed into the energy of SP. The energy of SP is dissolute in the metal film. Thus, the intensity of the incident light wave is decreased and detected as a dip in the function of the angular or wavelength of reflected spectrum [39, 40].

It can be seen that the SP excitation sensitive to the modification of the relative index of the dielectric on the surface of the conductor. A modification in the refractive index of the dielectric causes a change in the propagation constant of SP, resulting in the change of the coupling condition, for example coupling angle, coupling wavelength, intensity, and phase.

Base on this knowledge, sensors which use the principle of SP can be created by monitor the change of angular, wavelength, intensity, or phase [40].

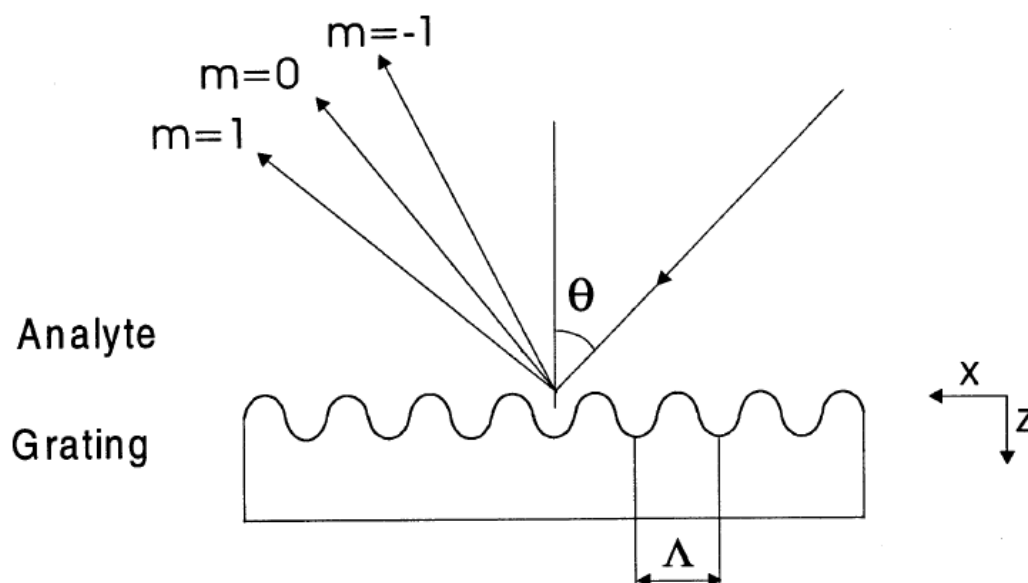


Figure 19 Diagram illustrated the diffraction of light by a diffraction grating [39].

5. Thin film bulk heterojunction organic solar cell

Thin film bulk heterojunction (BHJ) organic solar cell delivers a promising performance of light-electricity conversion. Recently, the organic photovoltaic technology has delivered the photoconversion efficiencies (PCEs) of those organic solar cells about 5-6% and rised up to 10.6% for those of tandem cell structures [41]. In gernal, the structure of thin film BHJ organic solar cell is the laminated organic thin films sandwiched between a transparent and metal electrodes, Figure 9. the bulk BHJ concept was introduced by blending two polymers having donor and acceptor properties in solution [42-44]. Figure 10 shows the polymer donors and fullerene acceptor that usually use for the fabrication the solar cell. To make a device, the mixture of the polymer is casted as a film to create the solid state mixture of donor polymer and fullerene acceptor. The lamination of two polymer layers is another method that provide a diffusive interface between donor and acceptor moieties [45].

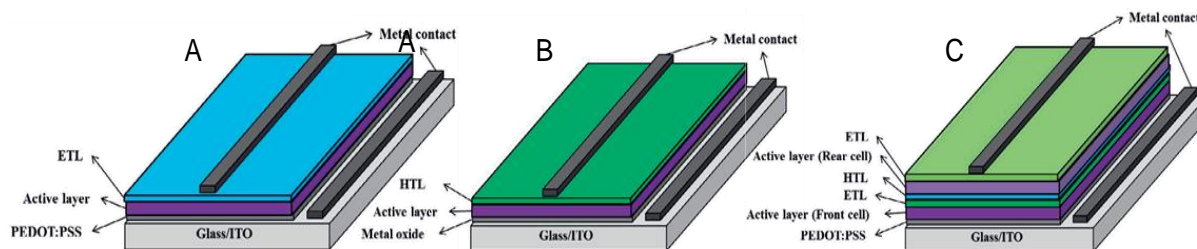
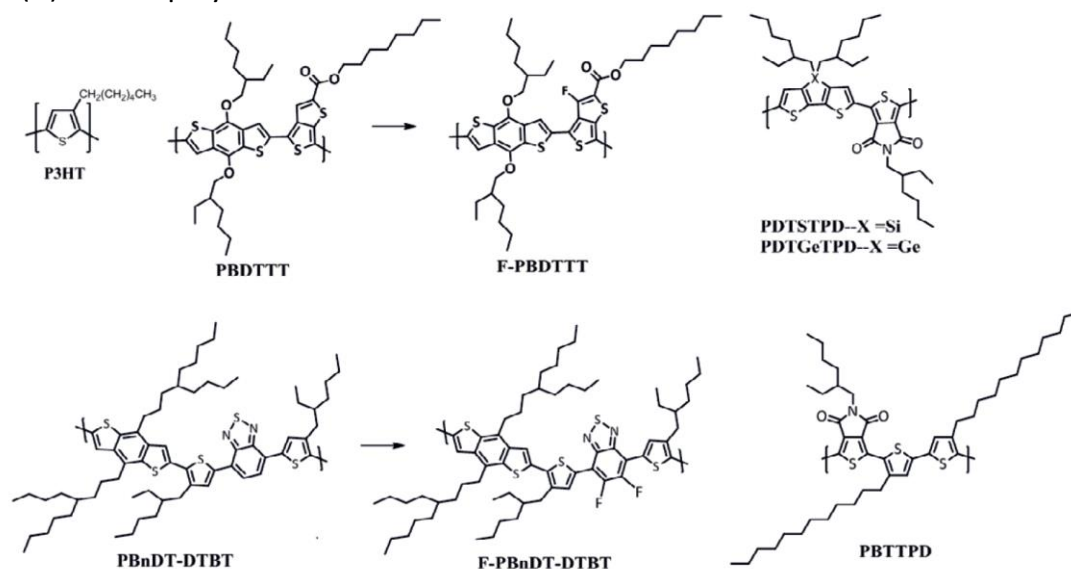


Figure 20 (A) common type solar cells with single-junction structure, (B) inverted type solar cells with single-junction structure, and (C) common type tandem solar cells with multi-junction structure [46].

(A) Donor: polymer



(B) Acceptor: fullerene

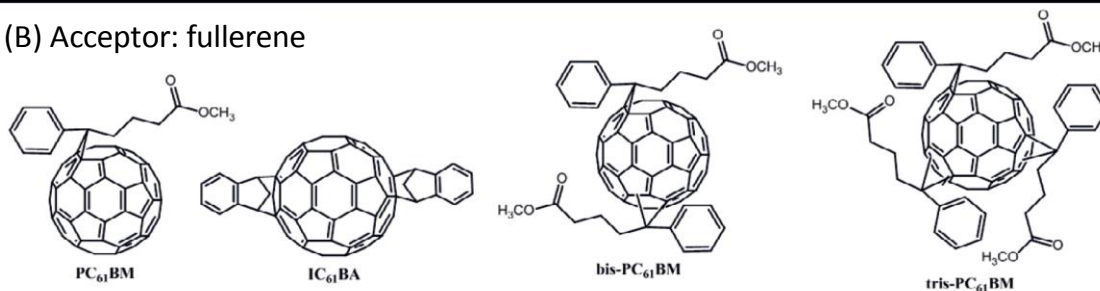


Figure 21 The examples of chemical structures of (A) polymer donors and (B) fullerenes acceptors used for making of the active layer of thin film organic solar cells [46].

Figure 11 shows the photoinduced charge transfer and its energetic description upon illumination. To generate the photocurrent, there are four fundamental steps of photon-electron conversion mechanism in organic solar cell. In the first step, under illumination, photoinduced excitation of electrons in the polymer donor occurs. The electron from the

highest occupied molecular orbital (HOMO) move to the lowest unoccupied molecular orbital (LUMO) of the polymer, resulting in the formation of a Frenkel exciton which is the electron-hole bound with coulombic interaction. For the second step, the photo-generated excitons migrate to the interfaces between the donor and acceptor within the diffusion length (L_D). In addition, the L_D value of the organic materials is normally 10 nm. Thus, the donor or acceptor domain size should be less than 20 nm to avoid the recombination. Third, charge-transfer (CT) process occurs at the donor-acceptor interface to procedure a CT exciton, where the hole remain in the donor while and the electron remain in the acceptor phases. Fourth, the last step, the CT exciton separates, causing the formation of free hole and electron, which are then move through the donor and acceptor phases, respectively, to their respective electrodes [46].

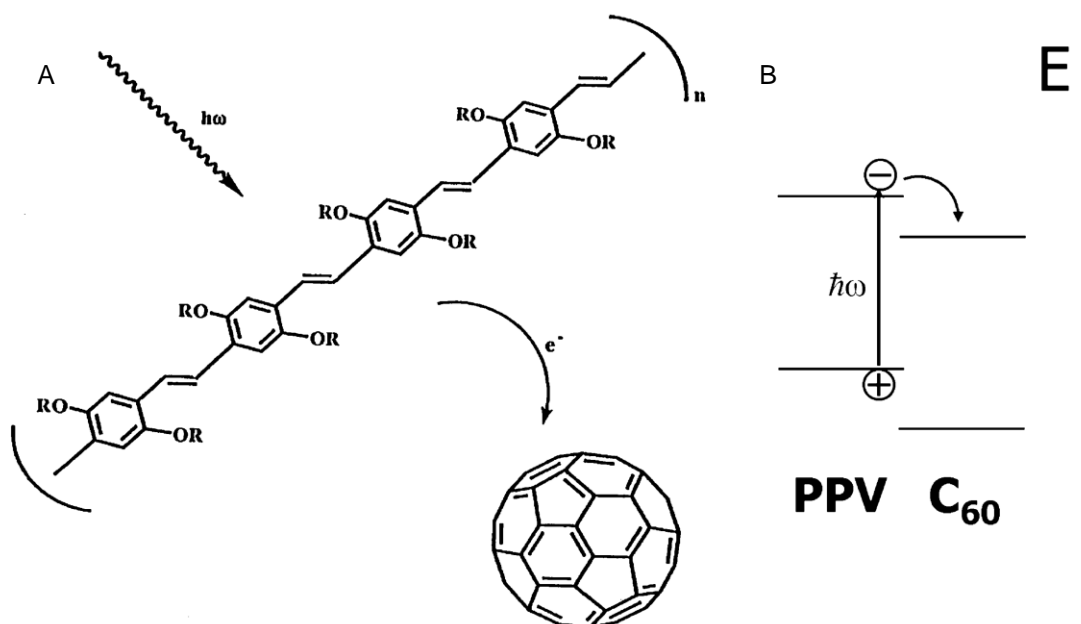


Figure 22 (A) The schematic of the photoinduced charge transfer of donor polymer to fullerene acceptor. (B) The energy level diagram. After excitation, the electron is transferred to the C₆₀ induced by electron affinity of C₆₀ [47].

To characterize the electrical properties of the solar cell, the current-voltage (I-V) measurement is performed. Figure 12 shows the I-V characteristics of the solar cell. Without illumination, I-V curve shows that the current can be obtained after the forward bias with the voltages larger than the open circuit voltage. Upon irradiation, the photocurrent flows with the reverse direction compare with the injected currents. Base on the I-V curve, in the fourth quadrant, the device can produce power (i.e., $I \times V$). At the maximum power point (I_{MMP} and

V_{MPP}), the power produced from the solar cell reaches the maximum. By comparison of the power to the incident light intensity, the efficiency of a solar cell can be evaluated. Filling factor (FF), which can be defined as the fraction of the photo-generated charge carriers that truly reach the electrodes, is given by $FF = V_{MPP} \times I_{MPP} / (V_{OC} \times I_{SC})$. Thus, the efficiency (η) of the device can be written followed equation [47]:

$$\eta_{POWER} = \frac{P_{OUT}}{P_{IN}} = \frac{I_{MPP} \cdot V_{MPP}}{P_{IN}} = \frac{FF \cdot I_{SC} \cdot V_{OC}}{P_{IN}}$$

where I_{SC} is the short-circuit current and V_{OC} is the open circuit voltage.

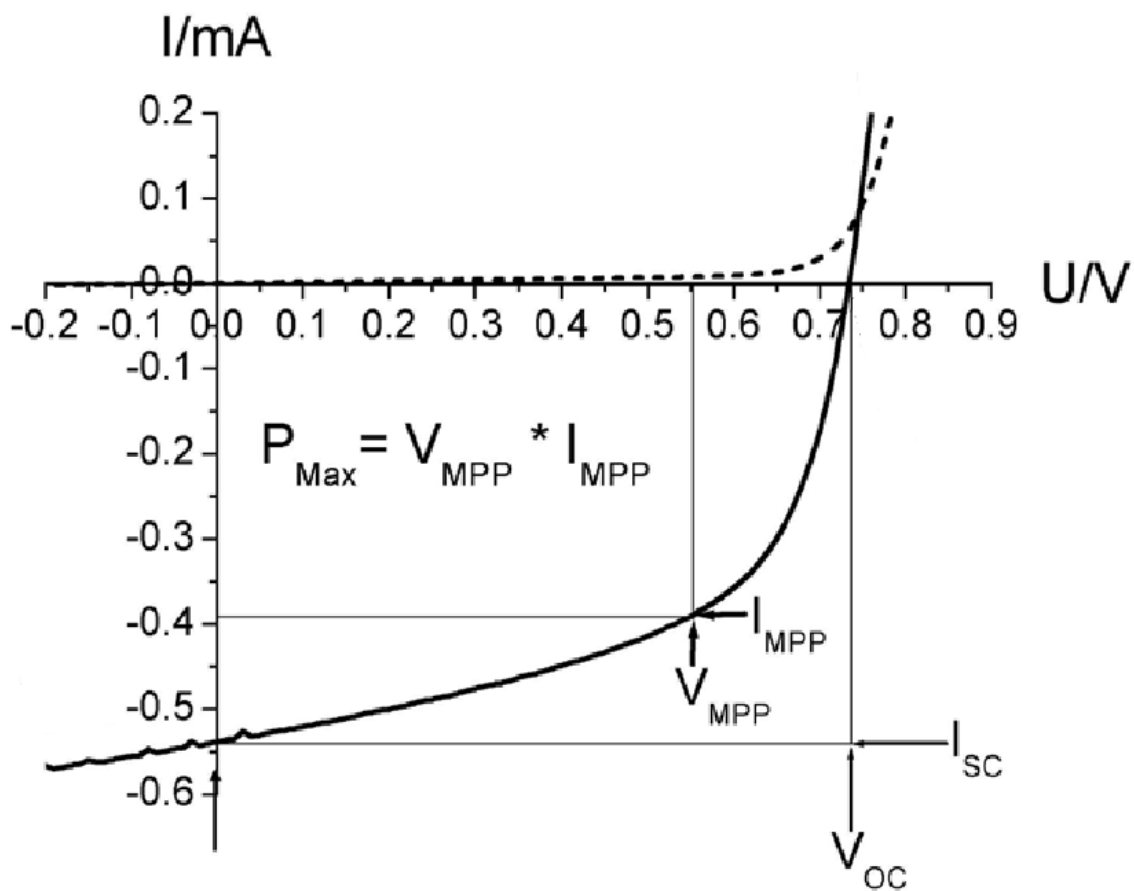


Figure 23 I-V characteristic of a thin film organic solar cell. The dashed line and the dark line represent I-V curves without and with illuminated, respectively [47].

As discussed above, the thin film organic solar cells technology provide a promising benefits of using those of organic solar cells, for example low cost of production and light weight. However, the nanometer-thin active layer lead to the low light trapping ability, resulting in the diminution of the performance. In addition, increase the thickness of the active

layer in the device can improve the light absorption, but decrease the device performance due to the increase of recombination process. To improve light trapping efficiency in photovoltaic device, numerous techniques have been developed. Introducing of nanostructures into the solar cell can improve the performance of the devices by reduce the reflected light [48, 49]. Using of plasmonic nanoparticles[50-52] as well as plasmonic grating structure [53, 54] in organic solar cells have been interested for several years as it show the promising enhancement of solar cell efficiency. However, the understanding of how plasmonic effect enhanced the organic solar cells is now being in the consideration. Thus, we have interested to study about how GCSPR improve the performance of the organic solar cell.

OBJECTIVES OF THE DISSERTATION

Because we have interested in the use of SPR property the metal nanostructures on the electronic application, i.e. photocatalyst and photovoltaic, as we mention above. Therefore we study and develop the system which uses the LSPR of metal nanoparticles, GCSPR, and the combination of LSPR and GCSPR to enhance the photocatalytic property of the photocatalyst (TiO_2). Moreover, the GCSP enhanced thin film organic photovoltaic was also studied. Thus, the key aims of this dissertation are:

1. To prepare gold nanoparticle (AuNP)- TiO_2 nanocomposite by a conventional wet-chemical reaction.
2. To study the photocurrent of the water splitting reaction originated catalyzed by AuNP- TiO_2 photocatalyst electrode under illumination of white light.
3. To study the LSPR and grating-coupled SP enhanced photocurrent of TiO_2 photocatalyst electrode.
4. To study the GCSPR enhanced thin film organic P3HT:PCBM solar cells.

SCOPE OF THE DISSERTATION

This dissertation exhibited the application of LSPR and GCSPR for the enhancement the photocatalytic activity of a thin film photocatalyst and performance of thin film organic photovoltaic. The dissertation is divided into two parts. For the first part, we focus on the use

of LSPR and GCSPR for enhancement of the photocurrent property of TiO₂ (P25). AuNP–TiO₂ nanocomposite was prepared by a simple wet-chemical reaction. The gold ions were reduced on the surface of TiO₂ using NaBH₄ as a reducer. Then the nanocomposite was deposited on transparent-conductive electrode (ITO-coated glass) to obtain AuNP–TiO₂ nanocomposite PEC electrode. The photocurrent of the water-splitting reaction catalyzed PEC with the enhancement of LSPR of the gold nanoparticles upon illumination with visible light was investigated. Moreover, we introduced a novel method to enhance the photocurrent of TiO₂ by a multiple plasmonic effect originated from the cooperation of LSPR of plasmonic gold nanoparticles and the GCSPR of a gold grating. For the second part, we study on the enhancement of the photocurrent and the efficiency of thin film P3HT:PCBM solar cells by GCSPR. The BD-R and BD grating pattern ($\Lambda = 330$ nm) were created on the active layer of the solar cell using pressure-less nanoimprinting technique, following by thermal evaporation of aluminum to obtain the BD-R and BD grating back electrode. The optical properties of the fabricated devices were investigated. The electrical properties of the solar cells were systematic studied. The discussion was separated into two topics as followed:

- 1. Investigation of localized surface plasmon/grating-coupled surface plasmon enhanced photocurrent in TiO₂ thin**
- 2. Grating-coupled SPR Enhanced NIR Activities of Organic Photovoltaic Devices Originated by BD-R and BD grating structures.**

REFERENCES

1. Carp, O., C.L. Huisman and A. Reller, *Photoinduced reactivity of titanium dioxide*. Prog. Solid State Chem., 2004. **32**(1–2): p. 33-177.
2. Nootchanat, S., H. Ninsonti, A. Baba, S. Ekgasit, C. Thammacharoen, K. Shinbo, K. Kato and F. Kaneko, *Investigation of localized surface plasmon/grating-coupled surface plasmon enhanced photocurrent in TiO₂ thin films*. PCCP, 2014. **16**(44): p. 24484-24492.
3. Ohtani, B., O.O. Prieto-Mahaney, D. Li and R. Abe, *What is Degussa (Evonik) P25? Crystalline composition analysis, reconstruction from isolated pure particles and photocatalytic activity test*. J. Photochem. Photobiol. A: Chem., 2010. **216**(2–3): p. 179-182.

4. Nakata, K. and A. Fujishima, *TiO₂ photocatalysis: Design and applications*. Journal of Photochemistry and Photobiology C: Photochemistry Reviews, 2012. **13**(3): p. 169-189.
5. Sau, T., A. Pal, N.R. Jana, Z.L. Wang and T. Pal, *Size Controlled Synthesis of Gold Nanoparticles using Photochemically Prepared Seed Particles*. J. Nanopart. Res., 2001. **3**(4): p. 257-261.
6. Tsunoyama, H., H. Sakurai, N. Ichikuni, Y. Negishi and T. Tsukuda, *Colloidal Gold Nanoparticles as Catalyst for Carbon–Carbon Bond Formation: Application to Aerobic Homocoupling of Phenylboronic Acid in Water*. Langmuir, 2004. **20**(26): p. 11293-11296.
7. Beqa, L., A.K. Singh, S.A. Khan, D. Senapati, S.R. Arumugam and P.C. Ray, *Gold Nanoparticle-Based Simple Colorimetric and Ultrasensitive Dynamic Light Scattering Assay for the Selective Detection of Pb(II) from Paints, Plastics, and Water Samples*. ACS Appl. Mater. Interfaces, 2011. **3**(3): p. 668-673.
8. Dang, Y.-Q., H.-W. Li, B. Wang, L. Li and Y. Wu, *Selective Detection of Trace Cr³⁺ in Aqueous Solution by Using 5,5'-Dithiobis (2-Nitrobenzoic acid)-Modified Gold Nanoparticles*. ACS Appl. Mater. Interfaces, 2009. **1**(7): p. 1533-1538.
9. Xu, X., J. Wang, K. Jiao and X. Yang, *Colorimetric detection of mercury ion (Hg²⁺) based on DNA oligonucleotides and unmodified gold nanoparticles sensing system with a tunable detection range*. Biosens. Bioelectron., 2009. **24**(10): p. 3153-3158.
10. Ai, K., Y. Liu and L. Lu, *Hydrogen-Bonding Recognition-Induced Color Change of Gold Nanoparticles for Visual Detection of Melamine in Raw Milk and Infant Formula*. J. Am. Chem. Soc., 2009. **131**(27): p. 9496-9497.
11. Obare, S.O., R.E. Hollowell and C.J. Murphy, *Sensing Strategy for Lithium Ion Based on Gold Nanoparticles*. Langmuir, 2002. **18**(26): p. 10407-10410.
12. Huang, D., Y. Qi, X. Bai, L. Shi, H. Jia, D. Zhang and L. Zheng, *One-Pot Synthesis of Dendritic Gold Nanostructures in Aqueous Solutions of Quaternary Ammonium Cationic Surfactants: Effects of the Head Group and Hydrocarbon Chain Length*. ACS Appl. Mater. Interfaces, 2012. **4**(9): p. 4665-4671.
13. Xie, J., Q. Zhang, J.Y. Lee and D.I.C. Wang, *The Synthesis of SERS-Active Gold Nanoflower Tags for In Vivo Applications*. ACS Nano, 2008. **2**(12): p. 2473-2480.
14. Han, X.X., B. Zhao and Y. Ozaki, *Surface-enhanced Raman scattering for protein detection*. Anal. Bioanal. Chem., 2009. **394**(7): p. 1719-1727.
15. Pienpinijtham, P., X.X. Han, T. Suzuki, C. Thammacharoen, S. Ekgasit and Y. Ozaki, *Micrometer-sized gold nanoplates: starch-mediated photochemical reduction synthesis*

- and possibility of application to tip-enhanced Raman scattering (TERS)*. PCCP, 2012. **14**(27): p. 9636-9641.
16. Deckert-Gaudig, T. and V. Deckert, *Ultraflat Transparent Gold Nanoplates—Ideal Substrates for Tip-Enhanced Raman Scattering Experiments*. Small, 2009. **5**(4): p. 432-436.
 17. Jia, W., J. Li, G. Lin and L. Jiang, *Two-Step Synthesis of Narrow Size Distribution Nanoflowers Using a Tree-Type Multi-Amine-Head Surfactant as a Template*. Cryst. Growth Des., 2011. **11**(9): p. 3822-3827.
 18. Huang, C.-C., W.-C. Lai, C.-Y. Tsai, C.-H. Yang and C.-S. Yeh, *Reversible Synthesis of Sub-10 nm Spherical and Icosahedral Gold Nanoparticles from a Covalent Au(CN)₂–Precursor and Recycling of Cyanide to form Ferric Ferrocyanide for Cell Staining*. Chem. Eur. J., 2012. **18**(13): p. 4107-4114.
 19. Zhou, M., S. Chen and S. Zhao, *Synthesis of Icosahedral Gold Nanocrystals: A Thermal Process Strategy*. J. Phys. Chem. B, 2006. **110**(10): p. 4510-4513.
 20. Li, C., K.L. Shuford, Q.H. Park, W. Cai, Y. Li, E.J. Lee and S.O. Cho, *High-Yield Synthesis of Single-Crystalline Gold Nano-octahedra*. Angew. Chem., 2007. **119**(18): p. 3328-3332.
 21. Ye, X., L. Jin, H. Caglayan, J. Chen, G. Xing, C. Zheng, et al., *Improved Size-Tunable Synthesis of Monodisperse Gold Nanorods through the Use of Aromatic Additives*. ACS Nano, 2012. **6**(3): p. 2804-2817.
 22. Kou, X., S. Zhang, C.-K. Tsung, Z. Yang, M.H. Yeung, G.D. Stucky, L. Sun, J. Wang and C. Yan, *One-Step Synthesis of Large-Aspect-Ratio Single-Crystalline Gold Nanorods by Using CTPAB and CTBAB Surfactants*. Chem. Eur. J., 2007. **13**(10): p. 2929-2936.
 23. Zijlstra, P., C. Bullen, J.W.M. Chon and M. Gu, *High-Temperature Seedless Synthesis of Gold Nanorods*. J. Phys. Chem. B, 2006. **110**(39): p. 19315-19318.
 24. Yamamoto, M., Y. Kashiwagi, T. Sakata, H. Mori and M. Nakamoto, *Synthesis and Morphology of Star-Shaped Gold Nanoplates Protected by Poly(N-vinyl-2-pyrrolidone)*. Chem. Mater., 2005. **17**(22): p. 5391-5393.
 25. Umar, A.A., M. Oyama, M.M. Salleh and B.Y. Majlis, *Formation of Highly Thin, Electron-Transparent Gold Nanoplates from Nanoseeds in Ternary Mixtures of Cetyltrimethylammonium Bromide, Poly(vinyl pyrrolidone), and Poly(ethylene glycol)*. Cryst. Growth Des., 2010. **10**(8): p. 3694-3698.

26. Fan, X., Z.R. Guo, J.M. Hong, Y. Zhang, J.N. Zhang and N. Gu, *Size-controlled growth of colloidal gold nanoplates and their high-purity acquisition*. *Nanotechnology*, 2010. **21**(10): p. 105602.
27. Beeram, S.R. and F.P. Zamborini, *Purification of Gold Nanoplates Grown Directly on Surfaces for Enhanced Localized Surface Plasmon Resonance Biosensing*. *ACS Nano*, 2010. **4**(7): p. 3633-3646.
28. Turkevich, J., P.C. Stevenson and J. Hillier, *The Formation of Colloidal Gold*. *J. Phys. Chem.*, 1953. **57**(7): p. 670-673.
29. Kimling, J., M. Maier, B. Okenve, V. Kotaidis, H. Ballot and A. Plech, *Turkevich Method for Gold Nanoparticle Synthesis Revisited*. *J. Phys. Chem. B*, 2006. **110**(32): p. 15700-15707.
30. Pienpinijtham, P., X.X. Han, S. Ekgasit and Y. Ozaki, *Highly Sensitive and Selective Determination of Iodide and Thiocyanate Concentrations Using Surface-Enhanced Raman Scattering of Starch-Reduced Gold Nanoparticles*. *Anal. Chem.*, 2011. **83**(10): p. 3655-3662.
31. Nootchanat, S., C. Thammacharoen, B. Lohwongwatana and S. Ekgasit, *Formation of large H₂O₂-reduced gold nanosheets via starch-induced two-dimensional oriented attachment*. *RSC Advances*, 2013. **3**(11): p. 3707-3716.
32. Vantasin, S., P. Pienpinijtham, K. Wongravee, C. Thammacharoen and S. Ekgasit, *Naked eye colorimetric quantification of protein content in milk using starch-stabilized gold nanoparticles*. *Sensors Actuators B: Chem.*, 2013. **177**(0): p. 131-137.
33. Petryayeva, E. and U.J. Krull, *Localized surface plasmon resonance: Nanostructures, bioassays and biosensing—A review*. *Anal. Chim. Acta*, 2011. **706**(1): p. 8-24.
34. Willets, K.A. and R.P. Van Duyne, *Localized Surface Plasmon Resonance Spectroscopy and Sensing*. *Annu. Rev. Phys. Chem.*, 2007. **58**(1): p. 267-297.
35. Barnes, W.L., A. Dereux and T.W. Ebbesen, *Surface plasmon subwavelength optics*. *Nature*, 2003. **424**(6950): p. 824-830.
36. Baba, A., K. Wakatsuki, K. Shinbo, K. Kato and F. Kaneko, *Increased short-circuit current in grating-coupled surface plasmon resonance field-enhanced dye-sensitized solar cells*. *J. Mater. Chem.*, 2011. **21**(41): p. 16436-16441.
37. Baba, A., N. Aoki, K. Shinbo, K. Kato and F. Kaneko, *Grating-Coupled Surface Plasmon Enhanced Short-Circuit Current in Organic Thin-Film Photovoltaic Cells*. *ACS Appl. Mater. Interfaces*, 2011. **3**(6): p. 2080-2084.

38. Homola, J., S.S. Yee and G. Gauglitz, *Surface plasmon resonance sensors: review*. *Sensors Actuators B: Chem.*, 1999. **54**(1–2): p. 3-15.
39. Homola, J., I. Koudela and S.S. Yee, *Surface plasmon resonance sensors based on diffraction gratings and prism couplers: sensitivity comparison*. *Sensors Actuators B: Chem.*, 1999. **54**(1–2): p. 16-24.
40. Homola, J., *Surface Plasmon Resonance Sensors for Detection of Chemical and Biological Species*. *Chem. Rev.*, 2008. **108**(2): p. 462-493.
41. Singh, R.P. and O.S. Kushwaha, *Polymer Solar Cells: An Overview*. *Macromolecular Symposia*, 2013. **327**(1): p. 128-149.
42. Tada, K., K. Hosoda, M. Hirohata, R. Hidayat, T. Kawai, M. Onoda, et al., *Donor polymer (PAT6) — acceptor polymer (CNPPV) fractal network photocells*. *Synth. Met.*, 1997. **85**(1–3): p. 1305-1306.
43. Yu, G. and A.J. Heeger, *Charge separation and photovoltaic conversion in polymer composites with internal donor/acceptor heterojunctions*. *J. Appl. Phys.*, 1995. **78**(7): p. 4510-4515.
44. Halls, J.J.M., C.A. Walsh, N.C. Greenham, E.A. Marseglia, R.H. Friend, S.C. Moratti and A.B. Holmes, *Efficient photodiodes from interpenetrating polymer networks*. *Nature*, 1995. **376**(6540): p. 498-500.
45. Granstrom, M., K. Petritsch, A.C. Arias, A. Lux, M.R. Andersson and R.H. Friend, *Laminated fabrication of polymeric photovoltaic diodes*. *Nature*, 1998. **395**(6699): p. 257-260.
46. Su, Y.-W., S.-C. Lan and K.-H. Wei, *Organic photovoltaics*. *Mater. Today*, 2012. **15**(12): p. 554-562.
47. Hoppe, H. and N.S. Sariciftci, *Organic solar cells: An overview*. *J. Mater. Res.*, 2004. **19**(07): p. 1924-1945.
48. Han, K.-S., J.-H. Shin, W.-Y. Yoon and H. Lee, *Enhanced performance of solar cells with anti-reflection layer fabricated by nano-imprint lithography*. *Sol. Energy Mater. Sol. Cells*, 2011. **95**(1): p. 288-291.
49. Forberich, K., G. Dennler, M.C. Scharber, K. Hingerl, T. Fromherz and C.J. Brabec, *Performance improvement of organic solar cells with moth eye anti-reflection coating*. *Thin Solid Films*, 2008. **516**(20): p. 7167-7170.
50. Lu, L., Z. Luo, T. Xu and L. Yu, *Cooperative Plasmonic Effect of Ag and Au Nanoparticles on Enhancing Performance of Polymer Solar Cells*. *Nano Lett.*, 2012. **13**(1): p. 59-64.

51. Chen, F.-C., J.-L. Wu, C.-L. Lee, Y. Hong, C.-H. Kuo and M.H. Huang, *Plasmonic-enhanced polymer photovoltaic devices incorporating solution-processable metal nanoparticles*. Appl. Phys. Lett., 2009. **95**(1): p. -.
52. Notarianni, M., K. Vernon, A. Chou, M. Aljada, J. Liu and N. Motta, *Plasmonic effect of gold nanoparticles in organic solar cells*. Solar Energy, 2014. **106**(0): p. 23-37.
53. Nalwa, K.S., J.-M. Park, K.-M. Ho and S. Chaudhary, *On Realizing Higher Efficiency Polymer Solar Cells Using a Textured Substrate Platform*. Adv. Mater., 2011. **23**(1): p. 112-116.
54. Li, X., W.C.H. Choy, L. Huo, F. Xie, W.E.I. Sha, B. Ding, et al., *Dual Plasmonic Nanostructures for High Performance Inverted Organic Solar Cells*. Adv. Mater., 2012. **24**(22): p. 3046-3052.

CHAPTER II

Investigation of localized surface plasmon/grating-coupled surface plasmon enhanced photocurrent in TiO₂ thin films

ABSTRACT

We fabricated plasmonic AuNP–TiO₂ nanocomposite films and measured the photocurrent that originates from the water-splitting reaction catalyzed by the AuNP–TiO₂ nanocomposite PEC electrode. The LSPR of the gold nanoparticles affected the generation of photocurrent by TiO₂ upon illumination with visible light. EIS revealed that the improvement in the photocurrent generation originates from an enhancement in electron–hole pair generation induced by the SPR of the plasmonic AuNPs than the extension of the electron lifetime. Moreover, we introduced a novel method to enhance the photocurrent of TiO₂ by a multiple plasmonic effect, i.e., LSPR of AuNPs and the GCSPP on a gold grating. We fabricated the AuNP–TiO₂ nanocomposites on a gold-coated BD-R. The enhancement of the photocurrent due to the combination of LSPR and the GCSPP was investigated

INTRODUCTION

The rapid development of economic systems today has led to an increase in global energy consumption, especially in large capital cities. Environmental pollution is increasing because of the release of byproducts into the atmosphere in the fossil fuel–electricity energy conversion process. Calculations performed in 2009 show that the expected time before the depletion of fossil fuels will be 107, 37, and 35 years for coal, gas, and oil, respectively [1]. Alternative energy sources, particularly solar energy, are therefore in demand for sustainable living. Photocatalysts have become important materials for solar energy harvesting. TiO₂ is a widely used photocatalyst due to its promising properties, which include physical and chemical stability, good photocatalytic activity, and low cost [2]. However, only solar photons in the UV region can excite this photocatalyst because of its large energy bandgap [3, 4]. In an effort to improve the photocatalytic activity, doping of TiO₂ with non-metal atoms such as N, C, and S or with transition-metal cations has been used to create an additional state in the bandgap and to extend the optical properties to the visible region [5, 6]. The doping of TiO₂ with noble metal nanoparticles has been of considerable interest. Noble metal nanoparticles provide strong optical extinction in the visible region because of the LSPR associated with the electromagnetic field surrounding nearby nanoparticle surfaces. The LSPR of metal nanoparticles can improve the photocatalytic activity of TiO₂ by three pathways, namely reradiation (scattering), transfer of energy to the adjacent semiconductors via plasmon resonance energy transfer (PRET), or production of hot electron transfer to nearby semiconductors [3, 7, 8]. As AuNPs provide an appropriate additional state, several

research groups reported the use of Au nanoparticles to study the optical activity of TiO₂ in the visible [3, 4, 6, 9, 10] and the near-infrared regions [7].

The GCSPR is another convenient propagating surface plasmon excitation method that does not involve the use of a prism. The grating structure provides light scattering and light trapping, both of which lead to an increase in the photocurrent event without SP excitation [11]. Our previous studies concerned the enhancement of the photocurrent of organic thin-film photovoltaic cells and dye-sensitized solar cells by using metal-coated gratings. The results showed high conversion efficiency for a gold grating substrate. Moreover, the corresponding results from simulations showed that the increase in the strong electric field with SP excitations leads to an increase in the photocurrent of the photovoltaic cells [12, 13].

In this study, we fabricated AuNP–TiO₂ nanocomposites and measured the photocurrent originating from the water-splitting reaction catalyzed by a AuNP–TiO₂ nanocomposite PEC electrode. The photocurrent properties were monitored under white light illumination to mimic real solar light. The LSPR of gold nanoparticles affected the generation of photocurrent in TiO₂ upon illumination with visible light. Moreover, a novel method was employed to enhance the photocurrent of TiO₂ by a multiple plasmonic effect, i.e., LSPR of plasmonic gold nanoparticles and the GCSPR on a gold grating. The AuNP–TiO₂ nanocomposites were fabricated on a gold-coated BD-R. The enhancement of the photocurrent due to the combination of the LSPR and the GCSPR was investigated.

EXPERIMENTAL

Chemicals and materials

Tetrachloroauric acid (HAuCl₄), sodium borohydride (NaBH₄), and titanium dioxide nanopowders (TiO₂, Aeroxides P25) were purchased from Sigma-Aldrich (Japan). Potassium chloride (KCl), polyvinyl alcohol (PVA), and methanol were acquired from Kanto Chemical Co. Ltd. All chemicals were used as received without additional purification. Deionized water (DI-water) was used as a solvent. Prior to use, all glassware and glass substrates were consecutively cleaned using a liquid detergent, tap water and DI-water in an ultrasonic bath (15 min for each step).

Synthesis and characterization of AuNP–TiO₂ nanocomposites

The AuNP–TiO₂ nanocomposites were synthesized by a simple wet chemical approach as reported elsewhere [14]. The percentage molar ratio of gold in the AuNP–TiO₂

nanocomposites (%Au–TiO₂) was varied by changing the concentration of gold ions, whereas the concentration of TiO₂ was kept constant at 6.3mM. In general, for the preparation of 4% Au–TiO₂, TiO₂ (0.05 g) was dispersed in DI-water with vigorous stirring for 10 min. The pH of the suspension was adjusted to 1 using 0.1 M HCl. The suspension was left in an ultrasonic bath for 1 h. After the dispersion process was complete, HAuCl₄ (0.5 mL, 50.8 mM) was added into the suspension with vigorous stirring for 1 h. A solution of NaBH₄ (0.4 M) was added dropwise to the suspension until the color of the suspension changed to purple. The suspension of AuNP–TiO₂ nanocomposites was aged overnight and preconcentrated to 250.4 mM by centrifugation. UV-visible absorption spectra of the AuNP–TiO₂ nanocomposites were recorded on a Jasco V650 UV-visible spectrophotometer and their morphologies were characterized by transmission electron microscopy (TEM) on a JEOL JEM-1200 EX microscope operating at 70 kV.

Fabrication of a AuNP–TiO₂ nanocomposite photocatalyst electrode on an ITO glass substrate

The suspension of AuNP–TiO₂ nanocomposites (5 mL, 250.4 mM), polyvinyl alcohol PVA (4.3 mL, 3.75% w/v), DI-water (0.7 mL), and methanol (10 mL) were mixed together with vigorous stirring for 2 h. The mixture was spin coated at 700 rpm onto indium-doped tin oxide (ITO) glass substrates. The spin-coating process was repeated 5 times. The film was dried under ambient conditions for 1 h and calcined at 400 °C for 2 h. A nanocomposite photocatalyst electrode with rough surfaces and a thickness of approximately 460 nm was obtained, as shown in Figure S1, APPENDIX A. Based on previous reports, [15-17] P25 TiO₂ is the combination of 70–80% of the anatase phase and 20–30% of the rutile phase.

Fabrication of the AuNP–TiO₂ nanocomposite photocatalyst electrode on a gold grating substrate

Diffraction gratings (L = 320 nm) were fabricated on BD-Rs (LTH type, TAIYO YUDEN), as described in our previous report [13]. The BD-Rs were cut into small rectangles (2.5 cm x 4.0 cm) and submerged in conc. HNO₃ for 20 min to remove the dye layer from the BD-Rs. After dye removal, the BD-Rs were consecutively cleaned with a liquid detergent, tap water, and twice in DI-water in an ultrasonic bath (15 min for each step) and dried under a stream of N₂. The clean BD-Rs were coated with a 150 nm gold film by thermal evaporation. The gold gratings were coated with the AuNP–TiO₂ nanocomposites dispersed in 50%

methanol by spin coating at 700 rpm. The photocatalyst electrodes were annealed at 90 °C for 30 min.

Characterization of photocurrent properties

The short-circuit photocurrent of the AuNP–TiO₂ nanocomposite photocatalyst electrode was collected using an HABF 5001 potentiostat from Hokuto Denko Corporation. The films were irradiated using an HAL-C100 solar simulator from Asahi Spectra USA Inc. The light intensity was 73 mW/cm². To study the photocurrent properties of the AuNP–TiO₂ nanocomposites, the AuNP–TiO₂ nanocomposite photocatalyst electrode (working electrode) and a platinum film (counter electrode) were mounted on a 1 cm-thick-Teflon cell, as shown in Figure S2, APPENDIX A. The reference electrode was Ag/AgCl, and the electrolyte was 0.1 M KCl. The active area of the cell was 2.7 cm². EIS was performed using a Parstat 4000 potentiostat from Princeton Applied Research at frequencies in the range 0.1–100 kHz and excitation amplitude of 15 mV. To measure the photocurrent of the nanocomposite/gold grating system, the AuNP–TiO₂ nanocomposite/gold grating photocatalyst electrode (working electrode) and platinum gauze fixed on a glass substrate (counter electrode) were mounted on a 0.3 cm-thick-Teflon cell, as shown in Figure S3, APPENDIX A. The electrolyte was 0.1 M KCl. The active area of the cell was 2.7 cm².

RESULTS AND DISCUSSION

Preparation of AuNP–TiO₂ nanocomposites

The AuNP–TiO₂ nanocomposites were synthesized by the reduction of gold ions on TiO₂ surfaces. It is known that the z-potential of dispersed TiO₂ particles becomes positive through the adsorption of H⁺ ions on the surface when the pH is lower than the isoelectric point (IEP) [18]. Therefore, the surface charge of the dispersed TiO₂ (IEP = 5.88) becomes positive when the pH of the solution is 1. The [AuCl₄]⁻ ions are attracted to positively charged TiO₂ through electrostatic interactions; consequently, they are reduced on the surface of TiO₂ by NaBH₄ [14, 19]. TEM images of TiO₂ and AuNP–TiO₂ nanocomposites are shown in Figure 1A and B, respectively. The size of the individual TiO₂ particles is in the range 15–20 nm. After the doping process, small spherical gold nanoparticles with a size range of 3–5 nm appear on the surface of TiO₂. The aggregation of the nanocomposite particles formed by the doping of AuNPs on the TiO₂ surface can be observed. A digital photograph of the AuNP–TiO₂ nanocomposites with various concentrations of AuNPs is shown in Figure 1C. The color of the dispersed nanocomposites gradually changed from

milky white to dark purple as the concentration of AuNPs increased from 0% to 8%. In addition, TiO₂ (P25), which is the composition between the anatase and rutile phases, has an absorption band in the UV region due to the approximately 3.2 eV band gap transition [20, 21]. Thus, the observed color change was caused by the existing gold nanoparticles on the TiO₂ surface. As the color of AuNP–TiO₂ nanocomposites changed to purple, the material should show optical activity in the visible region.

UV-visible absorption measurements were monitored to investigate the optical properties of the AuNP–TiO₂ nanocomposites. As shown in Figure 1D, the results reveal an improvement in the broad-band absorption in the visible region due to the LSPR phenomenon of AuNPs. As the Au–TiO₂ composition was increased from 0% to 8%, the absorption intensities at approximately 575 nm corresponding to the center of the SPR of AuNPs increased. As the LSPR peak of water-dispersed Au nanoparticles with the size of 3–5 nm is at around 520 nm, the observed LSPR peak is found to be red-shifted. This can be explained as follows: (i) the stabilizer-free system leads to the aggregation of those nanocomposites. The decrease of the inter-particle distance of adjacent plasmonic nanoparticles causes the coupling of LSPR. (ii) The aggregation of AuNP–TiO₂ affects the increase of the refractive index on the surface of nanoparticles [22, 23]. Furthermore, the band broadening of the SPR absorption peaks also implies the diversity of the shapes and sizes of the plasmonic nanoparticles because of the stabilizer-free system [24]. As the SPR of gold nanoparticles facilitates the optical activity of TiO₂ in the visible region, the photocatalytic activity of TiO₂, particularly for the photoinduced water-splitting reaction, is expected to be improved under white light irradiation.

Photocurrent properties of AuNP–TiO₂ nanocomposites

The photocatalytic properties of AuNP–TiO₂ nanocomposites were investigated by monitoring the photocurrents of the fabricated nanocomposite photocatalyst electrode. The films were irradiated with white light from a solar simulator without any UV-cutting filters. The light intensity was 73 mW/cm². As shown in Figure 2A and Figure S4 (APPENDIX A), the short-circuit photocurrent obtained from 0.5% Au–TiO₂ is optimum and approximately 1.5 times higher than that obtained from the original TiO₂ (0% of Au–TiO₂). During irradiation, transient decay of the photocurrent was observed. A reasonable explanation for this observation is the release of accumulated electrons, which are rapidly generated during irradiation, in the TiO₂ film [13, 25]. The I–V characteristics of TiO₂ and AuNP–TiO₂ nanocomposite films are shown in Figure 2B. The scanning potential range was between -0.5

V and +0.4 V versus open circuit potential under dark conditions with bare TiO₂. Positive photocurrents were observed for the TiO₂ and AuNP–TiO₂ nanocomposites upon illumination when the potential was more positive than -0.3 V. Higher photocurrent was obtained with AuNP–TiO₂ nanocomposites than with bare TiO₂. This result indicates the effect of AuNPs in enhancing the photocatalytic performance of TiO₂ under white light illumination.

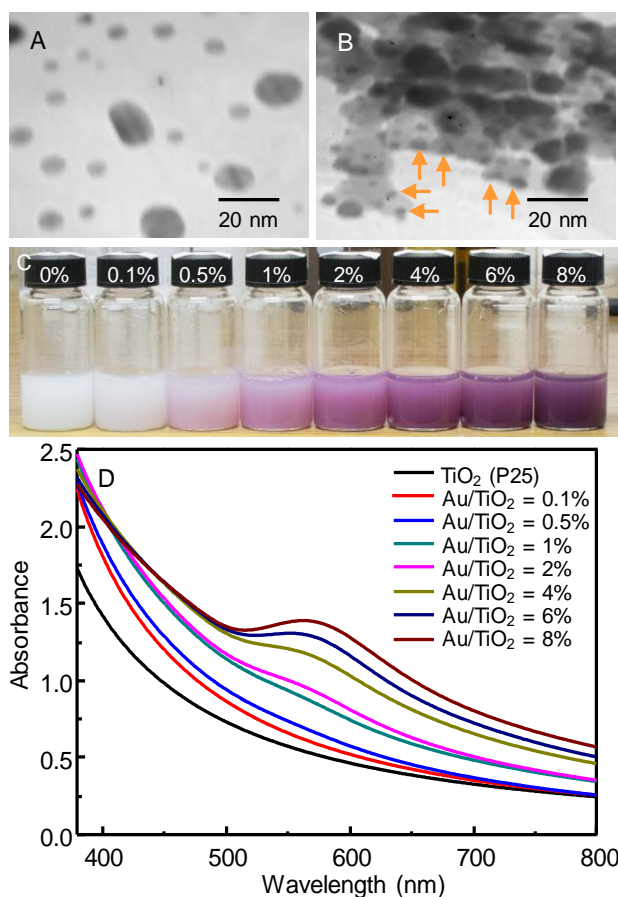


Figure 24 TEM images of (A) TiO₂ and (B) AuNP–TiO₂ nanocomposites with 0.5% of Au–TiO₂. The scale bars in (A) and (B) indicate 20 nm. The arrows indicate AuNPs on the TiO₂ surfaces. (C) Digital photograph and (D) UV-visible absorption spectra of AuNP–TiO₂ nanocomposites with various Au–TiO₂ ratios.

The relationship between short-circuit photocurrent and concentration of Au–TiO₂ nanocomposites is shown in Figure 2C. The results reveal that the photocurrent increased as the Au–TiO₂ increased, and a maximum current of approximately 17 mA was observed for 0.5% Au–TiO₂. However, an increase in the Au–TiO₂ level to more than 0.5% led to a decrease in the photocurrent of AuNP–TiO₂ nanocomposites. The decrease in the photocatalytic activities of AuNP–TiO₂ nanocomposites was observed for 2–8% Au–TiO₂ as the photocurrent was lower than the photocurrent from pure TiO₂. This result indicates that a

loading of gold nanoparticles with less than 1% Au–TiO₂ facilitates an improvement in the photocatalytic activity of TiO₂.

Under illumination, the photocatalytic activities of the AuNP–TiO₂ nanocomposites are dependent on separation of electron–hole pairs. In the UV region, TiO₂ handles the production of these charge carrier species through the absorption of high-energy photons in a process that provides the electrons in the conduction band and the holes in the valence band of the semiconductor [5]. The SPR of plasmonic nanoparticles induced by visible light establishes the localized electric field close to the surfaces of AuNPs, which facilitates the generation of electron–hole pairs in the adjacent semiconductor and the formation of hot electrons at AuNPs, which can then be injected into the conduction band of the semiconductor [5, 8]. The photocurrent properties under UV irradiation at $\lambda = 400$ nm, which does not include the wavelength region of LSPR, were studied first. As shown in Figure 3A, under UV illumination, the photocurrent obtained with 0%, 0.1%, and 0.5% Au–TiO₂ was 0.29, 0.50, and 0.34 mA, respectively. Photocurrents of less than 0.29 mA were observed for gold contents in the nanocomposites of more than 0.5% Au–TiO₂. The improvement and the decrease in the photocurrent of TiO₂ can be understood as the AuNPs capture the photoinduced electrons from TiO₂ and subsequently move these electrons from gold to the O₂ molecule on the semiconductor surface, thus leading to the formation of superoxide anion radicals, reduction in the recombination process, and enhancement of the dissociation of generated excitons. Conversely, excessive doping of AuNPs reduces the photocatalytic activity of TiO₂ because of the decrease in the number of titanol groups on the surface of TiO₂. Nevertheless, the high content of gold in the nanocomposite can act as a recombination center for the charge carrier species [26–28]. Another reasonable explanation for the improvement of photocurrent in those nanocomposite photocatalysts with 0.1% and 0.5% Au–TiO₂ under UV illumination is the SPR excitation of AuNPs by absorption of visible light emitted from TiO₂. It is known that the UV-excited anatase-phase TiO₂ can undergo visible luminescence [28, 29]. The plasmon excited AuNPs can create energetic electrons that can be injected into the conduction band of TiO₂ as it was observed with ZnO [30, 31]. However, the decrease of the photocurrent when increasing the percentage amount of gold in nanocomposites can be explained the observation that the doping of gold metal significantly diminishes the intensity as well as promotes the red-shift of the luminescence peak of TiO₂ [28]. The photocurrent induced by the LSPR of the plasmonic gold nanoparticles was studied upon illumination with polychromatic visible light ($\lambda = 530$ – 700 nm). As shown in Figure 3B, the photocurrents achieved increase as the gold content in the nanocomposites increases,

and a maximum photocurrent of 1.45 mA was obtained with 2% Au–TiO₂. The photocurrent decreases when the gold content is greater than 4% Au–TiO₂. This behavior can be attributed to the negative effect of the excessive amount of gold nanoparticles on the TiO₂ surface, as mentioned above. It was noted that the nanocomposite with 0.5% Au–TiO₂ did not produce the highest photocurrent under monochromatic UV and polychromatic visible illumination, in contrast to the illumination with white light (i.e., with the solar simulator without any cut-off filter), as can be seen from Figure 2C and 3. Therefore, the catalytic properties of AuNP–TiO₂ nanocomposites appear to originate from the synergistic effect of TiO₂ and plasmonic AuNPs under white light illumination.

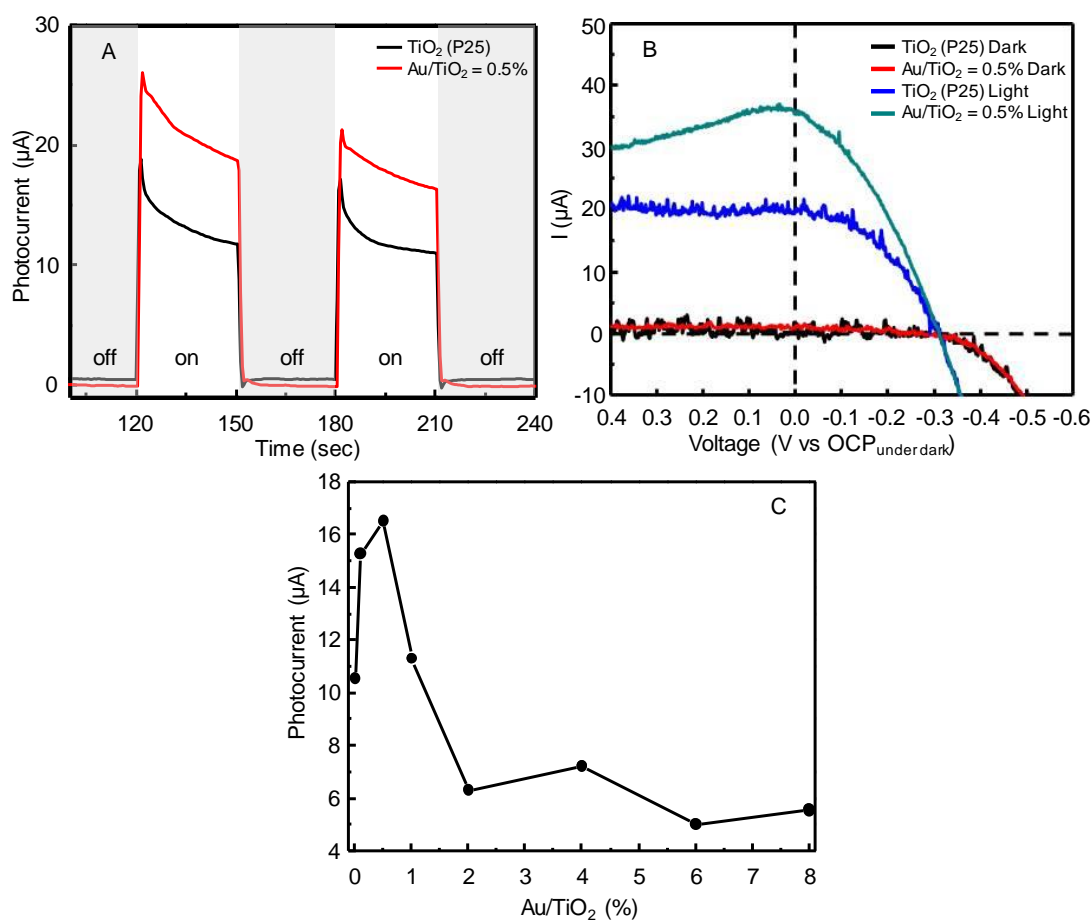


Figure 25 (A) Short-circuit photocurrent and (B) I–V characteristics of TiO₂ and AuNP–TiO₂ nanocomposites with 0.5% Au–TiO₂ with and without white light illumination. (C) Relationship between short-circuit photocurrent and the loading amount of gold nanoparticles in the nanocomposites.

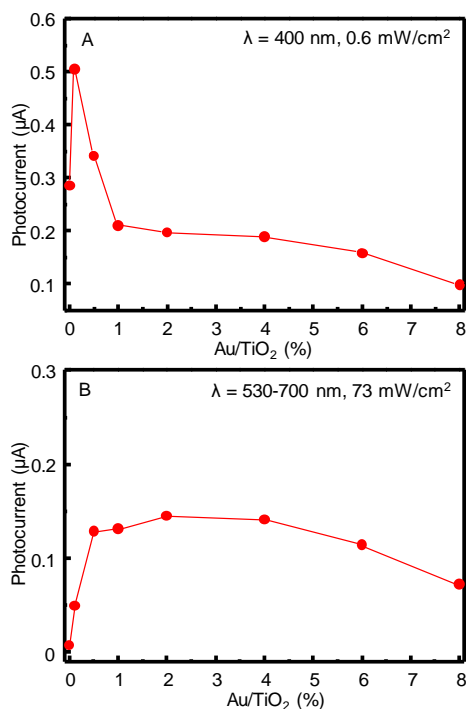


Figure 26 Short-circuit photocurrent of AuNP–TiO₂ nanocomposites with various amounts of gold nanoparticles upon irradiation with the wavelengths (A) 400 nm and (B) 530–700 nm.

Electrochemical impedance spectroscopy (EIS)

The photoinduced water-splitting reaction involves the photoelectrocatalytic reaction at the interface between the photocatalyst electrode and the electrolyte. As a consequence, we performed the EIS characterization upon white light illumination with respect to charge transfer resistance and electron–hole pair separation efficiency [32]. The Nyquist plots for the TiO₂ photocatalyst electrode are shown in Figure 4. Only one semicircle was observed in the low-frequency region of the Nyquist plots for TiO₂ and this can be attributed to the charge transfer step of the PEC reaction [33, 34]. The EIS results were analyzed using “ZSimpWin” software to achieve the equivalence circuit model containing ohmic resistance (R_s), charge transfer resistance (R_{ct}), and constant phase element (CPE).

The EIS spectra of the AuNP–TiO₂ nanocomposites with several gold loading amounts are shown in Figure 5 along with the Nyquist plot and the Bode phase plot. The detailed EIS parameters obtained from the Nyquist plot are shown in Table 1. The exchange current density (I_0) for the AuNP–TiO₂ nanocomposite electrode was calculated using eqn (1) and these values are also shown in Table 1 [35, 36].

$$I_0 = RT/nFR_{ct} \quad (1)$$

where R , T , n , and F are the gas constant, temperature, number of transferred electrons, and Faraday constant, respectively.

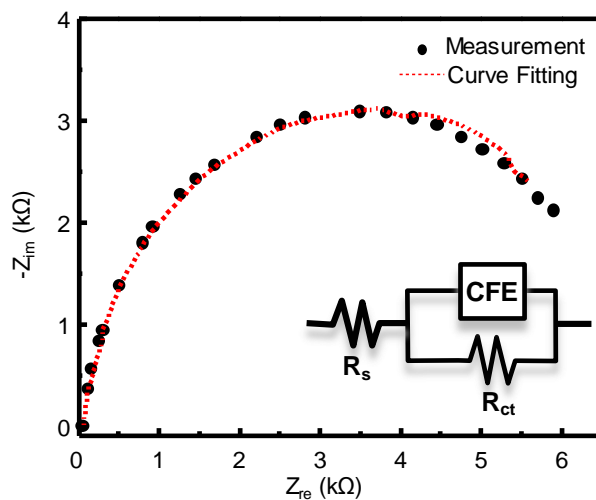


Figure 27 Nyquist plots for the TiO_2 photocatalyst electrode under white light illumination. The inset shows the equivalence circuit model obtained from the Nyquist curve fitting.

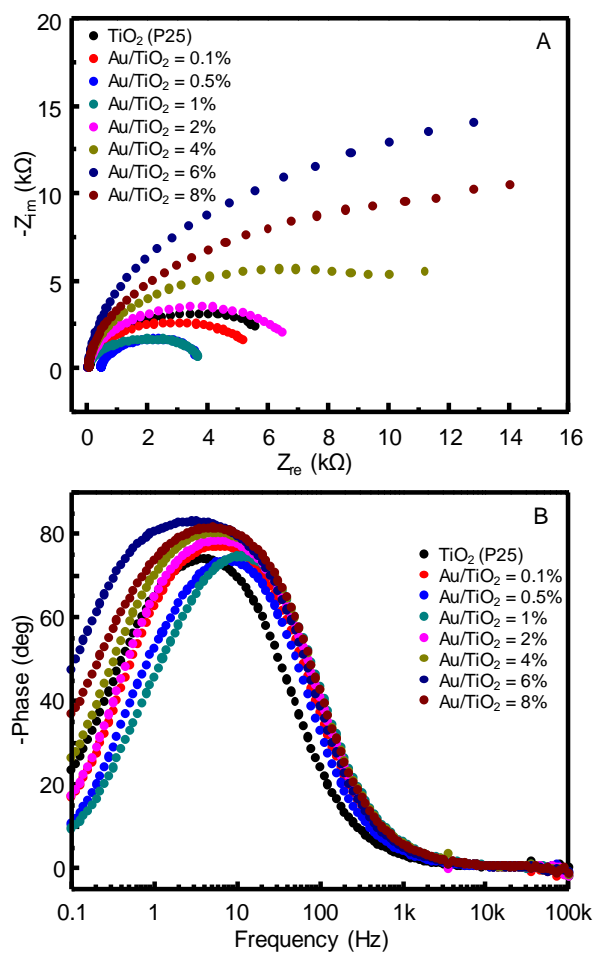


Figure 28 (A) Nyquist plot and (B) Bode phase plot for AuNP-decorated TiO_2 nanocomposite photocatalyst electrodes with various loading amounts of gold nanoparticles under illumination with white light.

Table 2 EIS parameters for AuNP-decorated TiO₂ nanocomposites

Au/TiO ₂	R _s (Ω)	R _{ct} (Ω)	I ₀ (μA/cm ²)	f _{peak}	τ (ms)
0	60	5,509	0.94	3.97	40
0.1	35	5,166	1.00	6.12	26
0.5	450	3,181	1.64	7.95	20
1	38	3,637	1.43	11.36	14
2	38	6,495	0.80	6.36	25
4	39	11,206	0.46	6.12	26
6	39	12,787	0.41	3.18	50
8	42	14,008	0.37	5.30	30

It can be seen from the results in Table 1 that the charge transfer resistance of the AuNP–TiO₂ nanocomposite photocatalyst electrodes decreases and reaches the lowest value of 3181 Ω at 0.5% Au–TiO₂. According to the charge transfer resistance, the highest exchange current density of 1.64 mA/cm² can be obtained from the same gold loading amount. In contrast, an increase in the charge transfer resistance and a decrease in the exchange current density are observed when Au–TiO₂ exceeds 0.5%. Based on the EIS results, the improvement in the PEC activities can be attributed to the effect of the SPR of the plasmonic gold nanoparticles, which enhances the electron–hole pair separation. Thus, the PEC reaction is promoted, resulting in an increase in the electrical current flow through the semiconductor/electrolyte interface. However, higher levels of gold loading cause recombination. Therefore, we assessed the lifetime of the photoinduced electrons of the nanocomposite electrodes. The Bode phase plot for the nanocomposite electrode reveals the single characteristic frequency peak (f_{\max}), which is related to the photoinduced electron lifetime (τ) in the nanocomposite electrodes, as described by the following equation [32, 37, 38]:

$$\tau = 1/(2\pi f_{\max}) \quad (2)$$

A decrease in the lifetime of the photoinduced electron together with an increase in the exchange current density was observed in the AuNP–TiO₂ nanocomposites as the concentration of AuNPs was increased from 0.1% to 1%. These changes in behavior could be

due to the effect of the SPR of gold nanoparticles in generating photoinduced electron–hole pairs with a high population. Thus, the recombination probabilities can increase as the electron lifetime decreases. However, compared to the pristine TiO₂, a decrease in the lifetime of the photoinduced electron together with a decrease in the exchange current density can be observed in the nanocomposites with Au–TiO₂ levels above 2%. The deterioration of the catalytic performance might be attributed to the decrease in the number of titanol groups on the TiO₂ surface and the increase in the number of recombination centers when a large amount of gold is present on the semiconductor. It should be noted that a slight increase in the electron lifetime was observed when the gold loading content exceeded 1%, and a low probability of recombination due to the generation of a small number of electron–hole pairs was recognized.

GCSPR-enhanced photocurrent properties of TiO₂ and AuNP-decorated TiO₂ nanocomposites

Our previous reports concerned the improvement of the short-circuit photocurrent of organic thin-film photovoltaic cells and dye-sensitized solar cells by using the GC-SPR technique [12, 13]. It was expected that a combination of the GCSPR of gold gratings and the LSPR of plasmonic AuNPs would lead to an enhancement in the photocatalytic activity of TiO₂. The gold grating substrate was fabricated by coating a 150 nm-thick gold film on a polycarbonate BD-R. An AFM image of the bare gold grating with a periodic grating pitch of ca. 320 nm is shown in Figure S5A, APPENDIX A. After the fabrication of the TiO₂ layer on the gold grating substrate, the AFM image clearly indicates that the periodic grating structure is covered by the TiO₂ layer, as shown in Figure S5B, APPENDIX A. The propagating SPR excitation on the grating substrate was studied by measuring the SPR reflectivity curve as a function of wavelength at various incident angles. Figure 6A and B show that the reflectivity curve on gold/grating clearly indicates that SPR can be obtained as the presence of the dip peaks in the reflection spectrum upon irradiation with p-polarized light. The redshift of the dip peaks from 520 nm to 638 nm upon increasing the incidence angle confirmed the SPR properties of the fabricated gold/grating substrate [39]. The SPR reflection spectra of the TiO₂–gold grating and the AuNP–TiO₂ nanocomposite/gold grating substrates are shown in Figure 6C and D, respectively.

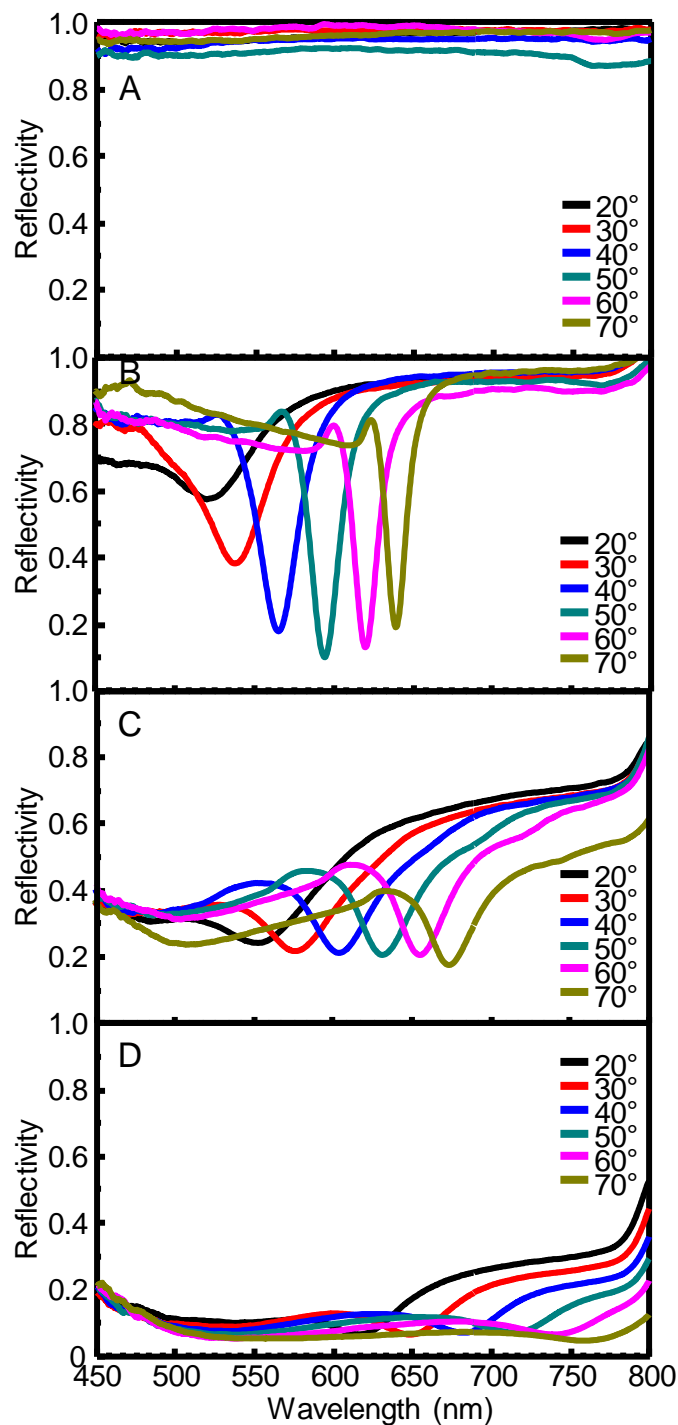


Figure 29 SPR reflectivity curves of the bare gold grating irradiated with (A) s-polarization and (B) p-polarization. SPR reflectivity curves of (C) TiO₂-gold grating photocatalyst electrode and (D) AuNP-TiO₂ nanocomposites/gold grating photocatalyst electrode irradiated with p-polarization.

The reflectivity curves are redshifted and the reflection intensity is decreased, as compared to the bare gold grating substrate. The change in the SPR reflection pattern is attributed to the modification of the reflective index of the casting layer [39, 40]. It should be

noted that the reflectivity of the AuNP–TiO₂ nanocomposite/gold grating substrate clearly decreased in the wide wavelength region studied, which indicates that the multiple plasmonic structure is a highly light-absorbing system. The reflectivity curves of the fabricated substrates irradiated with s-polarized light (without GCSPR excitation) indicated the decrease of the reflectivity (increase of light absorption) by adding AuNPs as shown in Fig. S6, APPENDIX A. However, as can be seen in Figure 6D and Figure S6B, APPENDIX A, the reflectivity with p-polarized light (with GCSPR) exhibits a further decrease (higher light absorption) as compared to that with s-polarized light (without GCSPR), clearly indicating that the multiple plasmonic effect, i.e. the combination of AuNPs and GCSPR, can improve the light absorption of the photocatalyst substrates. We previously reported that a strong electric field was generated from the AuNPs/Au grating film due to the interaction between LSPR of those plasmonic nanoparticles and GCSPR of gold grating [41–43]. Similar to our previous study, the interaction between LSPR of gold nanoparticles on TiO₂ surfaces and grating-coupled SPR of the gold grating substrate could be obtained. Upon direct light irradiation, plasmonic gold nanoparticles can generate a strong electric field by LSPR excitation on the surfaces of those plasmonic particles. Meanwhile, the GCSPR on gold grating is also excited by incident light, which also generates the strong electric field on the plasmonic gold particles deposited near the surface of gold grating. The strong electric field of GCSPR can further excite the LSPR on the gold nanoparticles. This interaction between LSPR and GCSPR could facilitate the multiple enhancement of electric field near the TiO₂ surface, resulting in the strong enhancement of the photocurrent of TiO₂.

To study the effect of SP-enhanced catalytic properties of the developed system, the photocurrent was monitored under white light illumination with s-polarization (without grating-coupled SP excitation) and p-polarization (with grating-coupled SP excitation). The incidence angles were varied from 0° to 40°. Incidence angles larger than 40° were neglected because of the limited experimental configuration of the photoelectrochemical cell. The photocurrent for the TiO₂–gold grating as a function of the incident angles is represented in Figure 7A. The results clearly indicate an improvement in the photocurrent for the TiO₂–gold grating with grating-coupled SP excitation for all incident angles. The lower photocurrents were obtained because low-temperature annealing was used in this experiment. Based on our previous simulation, which showed strong electric field intensity on the gold grating surface under p-pol illumination, [12, 13] the generation of electron–hole pairs for TiO₂ in the vicinity of the strong electric field is promoted, as shown schematically in Figure 7B.

The influence of GCSPR on the AuNP–TiO₂ nanocomposites was investigated further. The photocurrents of TiO₂–flat gold, TiO₂–gold grating, and AuNP–TiO₂–gold grating under p-polarization illumination (with GCSPR) are shown in Figure 8. The improvement in the photocurrent of the TiO₂–gold grating as compared to TiO₂–flat gold can be observed. Furthermore, a marked improvement in the photocurrent was obtained from the AuNP–TiO₂–gold grating with 0.5% Au–TiO₂ for all incident angles. The comparison of photocurrent after changing from s- to p-polarization is shown in Figure S7, APPENDIX A. This result indicates that the enhancement of the photocurrent from the AuNP–TiO₂–gold grating originates from the coupling effect of the LSPR and GCSPR of AuNPs and the gold grating substrate. As can be seen in Figure 7A and 8, the photocurrent decreased upon increasing the incident angle. This result is reasonable because the GCSPR excitation wavelength is far from the LSPR wavelength of AuNPs at higher incident angles, whereas the GCSPR wavelength at lower angles is closer to the LSPR wavelength. These results suggest that the multiple plasmonic effects, i.e., the GCSPR and LSPR complex system, are promising for the enhancement of photocurrent generation for the TiO₂ system.

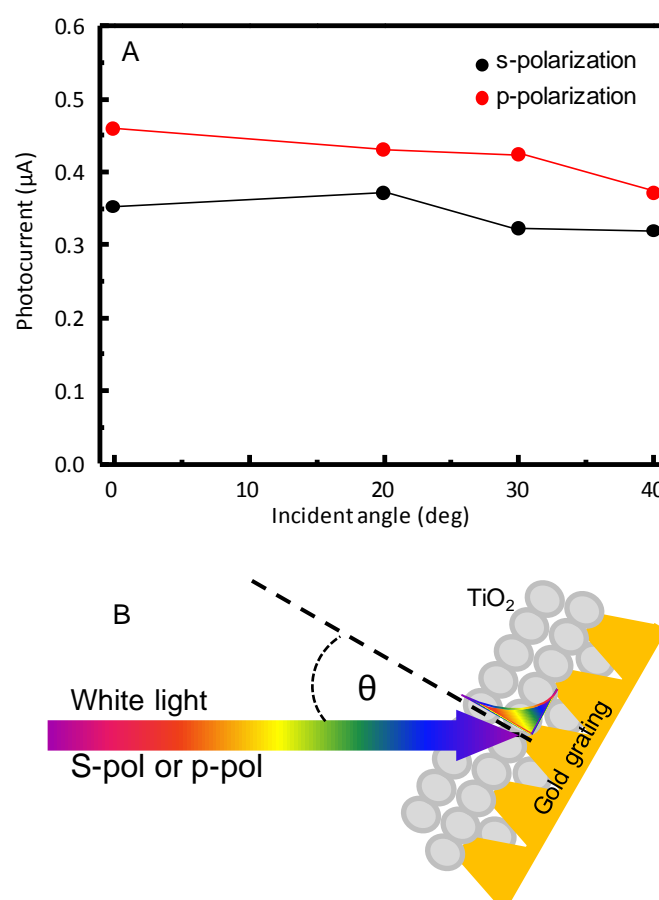


Figure 30 (A) Short-circuit photocurrent TiO₂–gold grating irradiated by white light with s- and p-polarization. (B) Schematic representation of the fabricated TiO₂–gold grating.

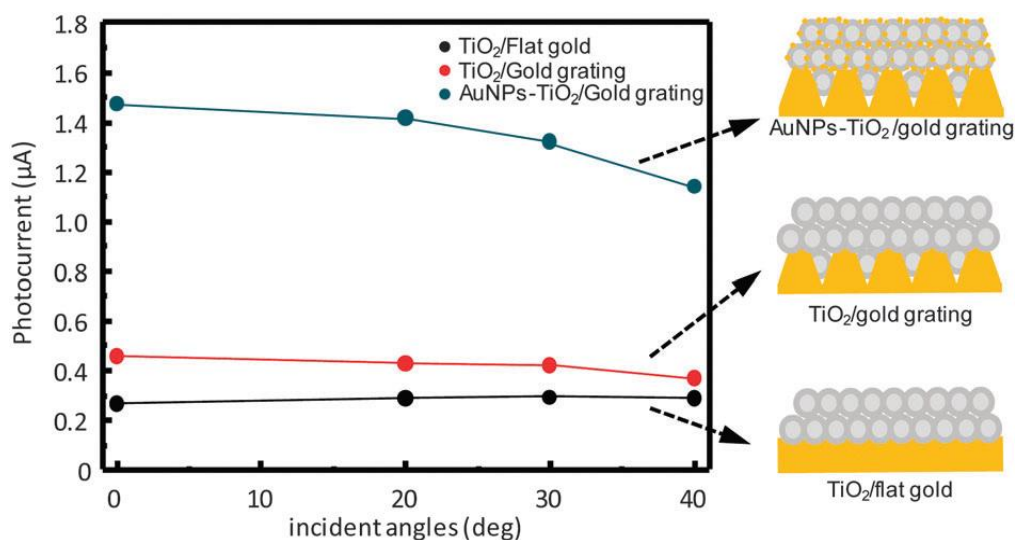


Figure 31 The short-circuit photocurrent of TiO₂-flat gold, TiO₂-gold grating, and AuNP-TiO₂ nanocomposite/gold grating irradiated by white light with p-polarization.

CONCLUSIONS

The AuNP-TiO₂ nanocomposites were fabricated by reducing gold ions on the TiO₂ surface, and the catalytic activity of this material was investigated by measuring the short-circuit photocurrent of the photocatalyst electrode under white light illumination. The AuNPs on the TiO₂ surface can extend the active photon range from only the UV region to both the UV and visible regions. The appropriate concentration of AuNPs in the nanocomposites was 0.5% Au-TiO₂ because this ratio provided the highest photocurrent signal in the UV-visible region. The use of higher amounts of gold in the AuNP-TiO₂ nanocomposites reduced the photocurrent properties and only low photocurrent production was observed. The results of the EIS study revealed that the improvement in the photocurrent originates from the enhancement of electron-hole pair generation induced by the SPR of the plasmonic gold nanoparticles rather than the extension of the electron lifetime. The photocurrent activity of the AuNP-TiO₂ nanocomposites can be further enhanced by surface plasmon resonance excitation from a gold grating substrate. The combination of the GCSPR from the gold grating and the LSRP from the gold nanoparticles provides a promising enhancement effect to increase the photocurrent. The results of this study could provide a greater understanding and basic knowledge of these systems as well as an enhancement of photocurrent intensity in photocatalytic devices for solar harvesting applications.

REFERENCES

1. Shafiee, S. and E. Topal, *When will fossil fuel reserves be diminished?* Energy Policy, 2009. **37**(1): p. 181-189.
2. Zhang, H., G. Wang, D. Chen, X. Lv and J. Li, *Tuning Photoelectrochemical Performances of Ag-TiO₂ Nanocomposites via Reduction/Oxidation of Ag.* Chem. Mater., 2008. **20**(20): p. 6543-6549.
3. Lee, J., S. Mubeen, X. Ji, G.D. Stucky and M. Moskovits, *Plasmonic Photoanodes for Solar Water Splitting with Visible Light.* Nano Lett., 2012. **12**(9): p. 5014-5019.
4. Mubeen, S., G. Hernandez-Sosa, D. Moses, J. Lee and M. Moskovits, *Plasmonic Photosensitization of a Wide Band Gap Semiconductor: Converting Plasmons to Charge Carriers.* Nano Lett., 2011. **11**(12): p. 5548-5552.
5. Gomes Silva, C., R. Juárez, T. Marino, R. Molinari and H. García, *Influence of Excitation Wavelength (UV or Visible Light) on the Photocatalytic Activity of Titania Containing Gold Nanoparticles for the Generation of Hydrogen or Oxygen from Water.* J. Am. Chem. Soc., 2010. **133**(3): p. 595-602.
6. Shi, X., K. Ueno, N. Takabayashi and H. Misawa, *Plasmon-Enhanced Photocurrent Generation and Water Oxidation with a Gold Nanoisland-Loaded Titanium Dioxide Photoelectrode.* J. Phys. Chem. C, 2012. **117**(6): p. 2494-2499.
7. Nishijima, Y., K. Ueno, Y. Yokota, K. Murakoshi and H. Misawa, *Plasmon-Assisted Photocurrent Generation from Visible to Near-Infrared Wavelength Using a Au-Nanorods/TiO₂ Electrode.* The Journal of Physical Chemistry Letters, 2010. **1**(13): p. 2031-2036.
8. Warren, S.C. and E. Thimsen, *Plasmonic solar water splitting.* Energy & Environmental Science, 2012. **5**(1): p. 5133-5146.
9. Chandrasekharan, N. and P.V. Kamat, *Improving the Photoelectrochemical Performance of Nanostructured TiO₂ Films by Adsorption of Gold Nanoparticles†.* J. Phys. Chem. B, 2000. **104**(46): p. 10851-10857.
10. Tian, Y. and T. Tatsuma, *Mechanisms and Applications of Plasmon-Induced Charge Separation at TiO₂ Films Loaded with Gold Nanoparticles.* J. Am. Chem. Soc., 2005. **127**(20): p. 7632-7637.
11. Zeng, L., P. Bermel, Y. Yi, B.A. Alamariu, K.A. Broderick, J. Liu, et al., *Demonstration of enhanced absorption in thin film Si solar cells with textured photonic crystal back reflector.* Appl. Phys. Lett., 2008. **93**(22): p. -.

12. Baba, A., N. Aoki, K. Shinbo, K. Kato and F. Kaneko, *Grating-Coupled Surface Plasmon Enhanced Short-Circuit Current in Organic Thin-Film Photovoltaic Cells*. ACS Appl. Mater. Interfaces, 2011. **3**(6): p. 2080-2084.
13. Baba, A., K. Wakatsuki, K. Shinbo, K. Kato and F. Kaneko, *Increased short-circuit current in grating-coupled surface plasmon resonance field-enhanced dye-sensitized solar cells*. J. Mater. Chem., 2011. **21**(41): p. 16436-16441.
14. Dawson, A. and P.V. Kamat, *Semiconductor–Metal Nanocomposites. Photoinduced Fusion and Photocatalysis of Gold-Capped TiO₂ (TiO₂/Gold) Nanoparticles*. J. Phys. Chem. B, 2001. **105**(5): p. 960-966.
15. Ohtani, B., O.O. Prieto-Mahaney, D. Li and R. Abe, *What is Degussa (Evonik) P25? Crystalline composition analysis, reconstruction from isolated pure particles and photocatalytic activity test*. J. Photochem. Photobiol. A: Chem., 2010. **216**(2–3): p. 179-182.
16. Zhang, J., M. Li, Z. Feng, J. Chen and C. Li, *UV Raman Spectroscopic Study on TiO₂. I. Phase Transformation at the Surface and in the Bulk*. J. Phys. Chem. B, 2005. **110**(2): p. 927-935.
17. Fernandes Machado, N.R.C. and V.S. Santana, *Influence of thermal treatment on the structure and photocatalytic activity of TiO₂ P25*. Catal. Today, 2005. **107–108**(0): p. 595-601.
18. Bae, H.S., M.K. Lee, W.W. Kim and C.K. Rhee, *Dispersion properties of TiO₂ nanopowder synthesized by homogeneous precipitation process at low temperatures*. Colloids Surf. Physicochem. Eng. Aspects, 2003. **220**(1–3): p. 169-177.
19. Subramanian, V., E.E. Wolf and P.V. Kamat, *Influence of Metal/Metal Ion Concentration on the Photocatalytic Activity of TiO₂–Au Composite Nanoparticles*. Langmuir, 2002. **19**(2): p. 469-474.
20. López, R. and R. Gómez, *Band-gap energy estimation from diffuse reflectance measurements on sol–gel and commercial TiO₂: a comparative study*. J. Sol-Gel Sci. Technol., 2012. **61**(1): p. 1-7.
21. Wang, H., T. You, W. Shi, J. Li and L. Guo, *Au/TiO₂/Au as a Plasmonic Coupling Photocatalyst*. J. Phys. Chem. C, 2012. **116**(10): p. 6490-6494.
22. Chen, H., X. Kou, Z. Yang, W. Ni and J. Wang, *Shape- and Size-Dependent Refractive Index Sensitivity of Gold Nanoparticles*. Langmuir, 2008. **24**(10): p. 5233-5237.
23. Wang, G. and W. Sun, *Optical Limiting of Gold Nanoparticle Aggregates Induced by Electrolytes*. J. Phys. Chem. B, 2006. **110**(42): p. 20901-20905.

24. DeSario, P.A., J.J. Pietron, D.E. DeVantier, T.H. Brintlinger, R.M. Stroud and D.R. Rolison, *Plasmonic enhancement of visible-light water splitting with Au-TiO₂ composite aerogels*. *Nanoscale*, 2013. **5**(17): p. 8073-8083.
25. Liu, Z., W. Hou, P. Pavaskar, M. Aykol and S.B. Cronin, *Plasmon Resonant Enhancement of Photocatalytic Water Splitting Under Visible Illumination*. *Nano Lett.*, 2011. **11**(3): p. 1111-1116.
26. Primo, A., A. Corma and H. Garcia, *Titania supported gold nanoparticles as photocatalyst*. *PCCP*, 2011. **13**(3): p. 886-910.
27. Wu, Y., H. Liu, J. Zhang and F. Chen, *Enhanced Photocatalytic Activity of Nitrogen-Doped Titania by Deposited with Gold*. *J. Phys. Chem. C*, 2009. **113**(33): p. 14689-14695.
28. Li, X.Z. and F.B. Li, *Study of Au/Au³⁺-TiO₂ Photocatalysts toward Visible Photooxidation for Water and Wastewater Treatment*. *Environ. Sci. Technol.*, 2001. **35**(11): p. 2381-2387.
29. Shi, J., J. Chen, Z. Feng, T. Chen, Y. Lian, X. Wang and C. Li, *Photoluminescence Characteristics of TiO₂ and Their Relationship to the Photoassisted Reaction of Water/Methanol Mixture*. *J. Phys. Chem. C*, 2006. **111**(2): p. 693-699.
30. Shao, D., H. Sun, M. Yu, J. Lian and S. Sawyer, *Enhanced Ultraviolet Emission from Poly(vinyl alcohol) ZnO Nanoparticles Using a SiO₂-Au Core/Shell Structure*. *Nano Lett.*, 2012. **12**(11): p. 5840-5844.
31. Lin, H.Y., C.L. Cheng, Y.Y. Chou, L.L. Huang, Y.F. Chen and K.T. Tsen, *Enhancement of band gap emission stimulated by defect loss*. *Opt. Express*, 2006. **14**(6): p. 2372-2379.
32. Chen, K., X. Feng, R. Hu, Y. Li, K. Xie, Y. Li and H. Gu, *Effect of Ag nanoparticle size on the photoelectrochemical properties of Ag decorated TiO₂ nanotube arrays*. *J. Alloys Compd.*, 2013. **554**(0): p. 72-79.
33. Liu, H., X.Z. Li, Y.J. Leng and W.Z. Li, *An Alternative Approach to Ascertain the Rate-Determining Steps of TiO₂ Photoelectrocatalytic Reaction by Electrochemical Impedance Spectroscopy*. *J. Phys. Chem. B*, 2003. **107**(34): p. 8988-8996.
34. Leng, W.H., Z. Zhang, J.Q. Zhang and C.N. Cao, *Investigation of the Kinetics of a TiO₂ Photoelectrocatalytic Reaction Involving Charge Transfer and Recombination through Surface States by Electrochemical Impedance Spectroscopy*. *J. Phys. Chem. B*, 2005. **109**(31): p. 15008-15023.
35. Wan, C., Y. Nuli, J. Zhuang and Z. Jiang, *Synthesis of spinel LiMn₂O₄ using direct solid state reaction*. *Mater. Lett.*, 2002. **56**(3): p. 357-363.

36. Yang, S., H. Song and X. Chen, *Electrochemical performance of expanded mesocarbon microbeads as anode material for lithium-ion batteries*. *Electrochem. Commun.*, 2006. **8**(1): p. 137-142.
37. Hsu, C.-P., K.-M. Lee, J.T.-W. Huang, C.-Y. Lin, C.-H. Lee, L.-P. Wang, S.-Y. Tsai and K.-C. Ho, *EIS analysis on low temperature fabrication of TiO₂ porous films for dye-sensitized solar cells*. *Electrochim. Acta*, 2008. **53**(25): p. 7514-7522.
38. Jiang, W., H. Liu, L. Yin and Y. Ding, *Fabrication of well-arrayed plasmonic mesoporous TiO₂/Ag films for dye-sensitized solar cells by multiple-step nanoimprint lithography*. *Journal of Materials Chemistry A*, 2013. **1**(21): p. 6433-6440.
39. Homola, J., I. Koudela and S.S. Yee, *Surface plasmon resonance sensors based on diffraction gratings and prism couplers: sensitivity comparison*. *Sensors Actuators B: Chem.*, 1999. **54**(1-2): p. 16-24.
40. Homola, J., *Surface Plasmon Resonance Sensors for Detection of Chemical and Biological Species*. *Chem. Rev.*, 2008. **108**(2): p. 462-493.
41. Lertvachirapaiboon, C., C. Supunabut, A. Baba, S. Ekgasit, C. Thammacharoen, K. Shinbo, K. Kato and F. Kaneko, *Transmission Surface Plasmon Resonance Signal Enhancement via Growth of Gold Nanoparticles on a Gold Grating Surface*. *Plasmonics*, 2013. **8**(2): p. 369-375.
42. Baba, A., K. Imazu, A. Yoshida, D. Tanaka and K. Tamada, *Surface plasmon resonance properties of silver nanoparticle 2D sheets on metal gratings*. *SpringerPlus*, 2014. **3**(1): p. 284.
43. Lertvachirapaiboon, C., A. Baba, S. Ekgasit, C. Thammacharoen, K. Shinbo, K. Kato and F. Kaneko, *Distance-Dependent Surface Plasmon Resonance Coupling Between a Gold Grating Surface and Silver Nanoparticles*. *Plasmonics*, 2014. **9**(4): p. 899-905.

CHAPTER III

Grating-coupled SPR Enhanced NIR Activities of Organic Photovoltaic Devices Originated by BD-R and BD Grating Structures.

ABSTRACT

In this report, we studied the GCSPR enhanced thin film organic solar cells. The device with structure of Al/P3HT:PCBM/PEDOT:PSS:ITO/glass were fabricated. BD-R and BD grating patterns were produced on the top of the active layer, following by the formation of Al film to obtain the grating back electrode for each solar cell. The presence of diffraction grating patterns shows the improvement of light absorption of the solar cell which can be described to the effect of light scattering and GCSPR. Our results show that the enhancement of photocurrent and efficiency of solar cells can be obtained from the solar cells with BD and BD-R grating structures compared with our device without grating. The improvement of the photocurrents from the BD-R and BD solar cells are 11.05% and 10.6%, respectively. Nevertheless, the enhancement of efficiency of BD-R and BD solar cell are obtained with 19.28% and 3.21%, respectively.

INTRODUCTION

BHJ solar cell exhibits a promising performance of light-electricity conversion efficiency together with several advantages, for example light weight, being flexible, inexpensive, etc [1]. The BHJ concept was introduced by blending of two polymers having donor and acceptor properties together in order to achieve the active layer of the solar cell with the elevated existing of donor-acceptor interfacial area for exciton dissociation. This reduce the diffusion distance that the photogenerated exciton needs to move before reaching the donor-acceptor interface, resulting in the reduce of recombination and increase the charge photo generation. [1-4]. Upon irradiation, the photocurrent is generated by the absorption of light over the absorption region of the blended polymers. The increase of the thickness of the active layer can increase the light absorption, but decrease the efficiency of the BHJ solar cell. This limitation is due to the short diffusion length of the photogenerated excitons in the blended polymer layer which is typically less than 20 nm [5, 6]. Thus, increase the thickness of the active layer can increase the possibility of recombination. Numerous techniques have been developed aiming to improve the light trapping ability of the BHJ solar cells. Introducing of nanostructures into the BHJ solar cells can create the light trapping layer and improve the performance of the devices by reduce the reflected light [7, 8]. The fabrication of the solar cell on the textured substrate, in particular V-shaped light trapping configuration, can be an interesting way to improve the solar cell performance with the 52% efficiency enhancement via multiple reflection of incident light [9].

The use of plasmonic structures in the solar cells is a promising approach to create

additional light trapping layer facilitating the improvement light absorption capability and efficiency of the solar cells without increase of the active layer thickness. Plasmonic nanoparticles, such as Au and Ag [10-14] offer the enhancement of the efficiency via light scattering effect that can couple and trap the light into the active layer, and LSPR effect that can provide the strong near field enhancement near the surface of the particle to increase the absorption of the absorber near by [15, 16]. Similar to plasmonic nanoparticles, metallic-corrugated nanostructure can be an efficient light-trapping element for the solar cells by coupling of the incident light into GCSPP which cause the trapping and guiding of light into semiconductor [15-21]. Several groups have reported the benefit of using of periodic [16, 17] and non-periodic [18, 22] diffraction grating to enhancement of the efficiency of the solar cells. In the same way, our previous works also showed that the GCSPP can enhance short-circuit photocurrent of photovoltaic devices as well as dye-sensitized solar cells which were fabricated on top of metal-coated BD-R [23, 24].

In this work, we investigate the GCSPP enhanced BHJ solar cells. The solar cell Al/P3HT:PCBM/PEDOT:PSS/ITO/glass was fabricated. The subwavelength diffraction grating pattern was transferred from a master template to the active layer of the solar cell using PDMS mould. The formation of the grating structure in the surface of the blended polymer was studied. The effect of two different diffraction gratings, in particular periodic (BD-R) and non-periodic (BD) were studied. Using of used BD-R and BD can be an alternative way to reduce electronic wastes yet benefit the energy industry. The SPR reflectivity results reveal the increase of trapped light as a broad band absorption from 400 nm to 650 nm in the device with grating structure which can be the effect of light scattering. The increase of the absorption at the wavelength long than 650 nm can be observed and assigned to the GCSPP of Al grating as the presence of redshifted dip when increase the incident angle. The introducing of BD and BDR diffraction grating as the additional light trapping layer can increase the short-circuit photocurrent and the efficiency of the solar cells. To gain more insight understanding on how diffraction grating enhance the performance of the solar cells, spectral-photocurrent experiments were conducted under illumination of polarized light. The enhancement of photocurrent originated from the light scattering effect and GCSPP were studied.

EXPERIMENTAL

Chemicals and Materials

Poly(3-hexylthiophene-2,5-diyl) (P3HT), 1-(3-methoxycarbonyl)propyl-1-

phenyl[6,6]C₆₁ (PCBM), and 1,2-dichlorobenzene were purchased from Sigma-Aldrich (Japan). CleviosTM HTL Solar, which used as hole-transport material, was obtained from Heraeus Precious Metals GmbH & Co. KG (Germany). Polydimethylsiloxane (PDMS, Sylgard® 184 silicone elastomer kit) was acquired from Dow Corning Corporation (United States). All chemicals were used as received without additional purification. ITO-coated glasses (10 Ω/cm²) were purchased from Furuuchi chemical (Japan). To prepare a transparent electrode for a solar cell, the ITO coated glass was cut into small pieces with the size of 2 × 2.5 cm. ITO patterns were formed by HCl etching method. The patterned ITO electrodes were stepwise cleaned by liquid detergent, tap water, and two times of deionized water in an ultrasonic bath, 15 minutes for each step, and dried by blowing of N₂. BD-R and BD were used as periodic and non-periodic diffraction grating templates, respectively. The BD-R and BD were cut into several pieces and immersed them in conc. HNO₃ to eliminate the dye layer deposited on the polycarbonate grating substrate. The BD-R and BD were cleaned and dried. As shown in Figure S1, APPENDIX B, the BD-R provide a periodic rectangular grating pattern with a 330 nm grating pitch and a ~39 nm grating height while the BD provide a discontinuous pit array with pitch length and depth of 330 nm and ~48 nm, respectively. To prepare PDMS moulds, the cleaned BD-R and BD were used as master templates. The liquid PDMS was casted on top of the BD-R and BD and then placed in vacuum chamber for 2 hours in order to remove air bubbles in the liquid PDMS, followed by curing at 79 °C for 3 hours. After curing, the PDMS moulds could be easily removed from the master templates and used for transferring of diffraction grating pattern to the active layer of the solar cells.

Device Fabrication

The P3HT:PCBM blended polymer solution was prepared by dissolving of P3HT (0.015 g) and PCBM (0.012) in DB (1.3g) and left it in the ultrasonic bath overnight. The concentration of blended polymer solution was 27 mg/mL with the P3HT:PCBM weight ratio of 1:0.8. To fabricate the solar cell, the ITO substrate was treated with UV/O₃ for 50 minutes in order to remove any dirt and improve the wettability of the ITO surface. The hole transport layer was formed on the ITO electrode by spin coating of the CleviosTM HTL Solar solution at 3000 rpm and dried at 120 °C for 11 minutes. The active layer was applied on the hole transport layer by spin-coating at 1500 rpm. Figure S2, APPENDIX B, shows the fabrication of grating structure on the solar cell. The PDMS mould was carefully applied on the surface of active layer. Note that, any air bubbles trapped between the PDMS mould and the substrate must be eliminated. Then, the whole substrate was left in an oven at 100 °C for 60 minutes

and cooled down to room temperature before detachment of the PDMS mould. A 150 nm-thick aluminum film was formed on the P3HT:PCBM blended polymer layer using thermal evaporation. The device Al/P3HT:PCBM/PEDOT:PSS/ITO/glass was anneal at 150 °C in a vacuum chamber before characterizations.

Characterization

The morphologies of fabricated devices were studied by an atomic force microscope (AFM, SPM-9600 from Shimadzu Corporation). For the SPR-reflectivity characterization, the solar cell was fixed on a θ - 2θ goniometer stage. The device was irradiated by polarized white light generated from a halogen light source. The zero-order reflected light was detected by a monochromatic light detector. The SP excitation was examined as a function of the wavelength at a specific incident angle. To characterize the electrical properties of the fabricated solar we conducted an electrometer (B2901 from Agilent Technology). The devices were illumined by a solar simulator (HAL-C100 from Asahi Spectra USA Inc.) with the intensity of 75 mW/cm². For the spectral-photocurrent study, the solar cells were irradiated using a monochromatic light source (MLS-1510 from Asahi Spectra USA Inc.). To study the electrical properties of the solar cells with different angles of illumination, the devices were mounted on a rotatable stage as shown in Figure S3, APPENDIX B. For illumination of polarized light, a linear polarizer was applied between light source and the solar cell, Figure S3 (B), APPENDIX B.

RESULTS AND DISCUSSION

Formation of diffraction grating pattern on the solar cell.

To fabricate the grating structure on the solar cell devices, we transfered the BD-R and BD grating patterns to the active layer of the solar cells using the PDMS moulds. The moulds were carefully placed on the active layer in order to create the nanoconfinement contact between the grating grooves and the surface of the polymer film. In addition, the mobility of the blended polymer plays an important role in the formation of grating structure as it needs to flow into the grooves of the PDMS mould to created the corrugate pattern. Our results show that the solvent left in the polymer film and the thermal annealing at the temperature slightly above the glass transition temperature (T_g) of P3HT:PCBM blended polymer, particularly at 100 °C, can promote the formation of the grating pattern by changing the solid-state polymer film to viscous-state polymer film during the nanoimprinting process[25, 26]. Thus, the polymer can flow into the grating grooves of the moulds, resulting in the

formation of grating structure. An experimental design indicated the role of solvent and the thermal annealing in nanoimprinting process was conducted. Without thermal annealing, the BD-R grating pattern can be obtained from the nanoimprinting of the damp polymer film with the grating height of 2.9 nm, Figure S4 (A) and (D), APPENDIX B. Unlike damp polymer film, the nanoimprinting of the dry polymer film does not provide the grating pattern, Figure S4 (B) and (E), APPENDIX B. This indicates that the solvent in the polymer film can promote the formation of grating pattern in the nanoimprinting process. Besides, with thermal annealing, the BD-R grating pattern with the grating height as high as ~15 nm can be obtained from the nanoimprinting of dry polymer film (Figure S4 (C) and (F) in APPENDIX B). Therefore, we accompanied the nanoimprinting process of damp polymer film with thermal annealing. Figure 1 (A), (C), and (E) show the AFM images of the surfaces of blended polymer film on PEDOT:PSS/ITO/glass after nanoimprinting. Compared with the flat device, the BD-R and BD imprinted devices show the homogeneous periodic and discontinuous diffraction grating pattern, respectively. The BD-R grating height is approximately 27.2 nm while the BD grating depth is approximately 32.4 nm. By using the patterned active layer as the template, Al back electrode with grating structures can be obtained after the formation of Al film. Figure 1 (D) and (F) show the AFM images of the Al surfaces obtained from the solar cells with BD-R and BD grating structure. The BD-R grating height slightly increases to ~32 nm while the BD grating depth slightly decreases to ~32 nm. Note that, the formation of aluminum film on the flat active layer can produce only the flat aluminum electrode as shown in Figure 1B. Figure S5, APPENDIX B, shows the digital photographs of the fabricated solar cells. The appearance of the rainbow color on the devices upon illumination suggests the iridescent scattering by BD-R and BD grating structure layer in the devices close to the blended polymer layer. This phenomenon can be attributed to the modification of the light traveling direction inside the solar cell with grating structures compared with the flat device. The change of the light traveling direction could benefit the improvement of the performance of the solar cell due to the increase in the light path inside the active layer which causes the improvement of the light absorption and the efficiency of the solar cells.

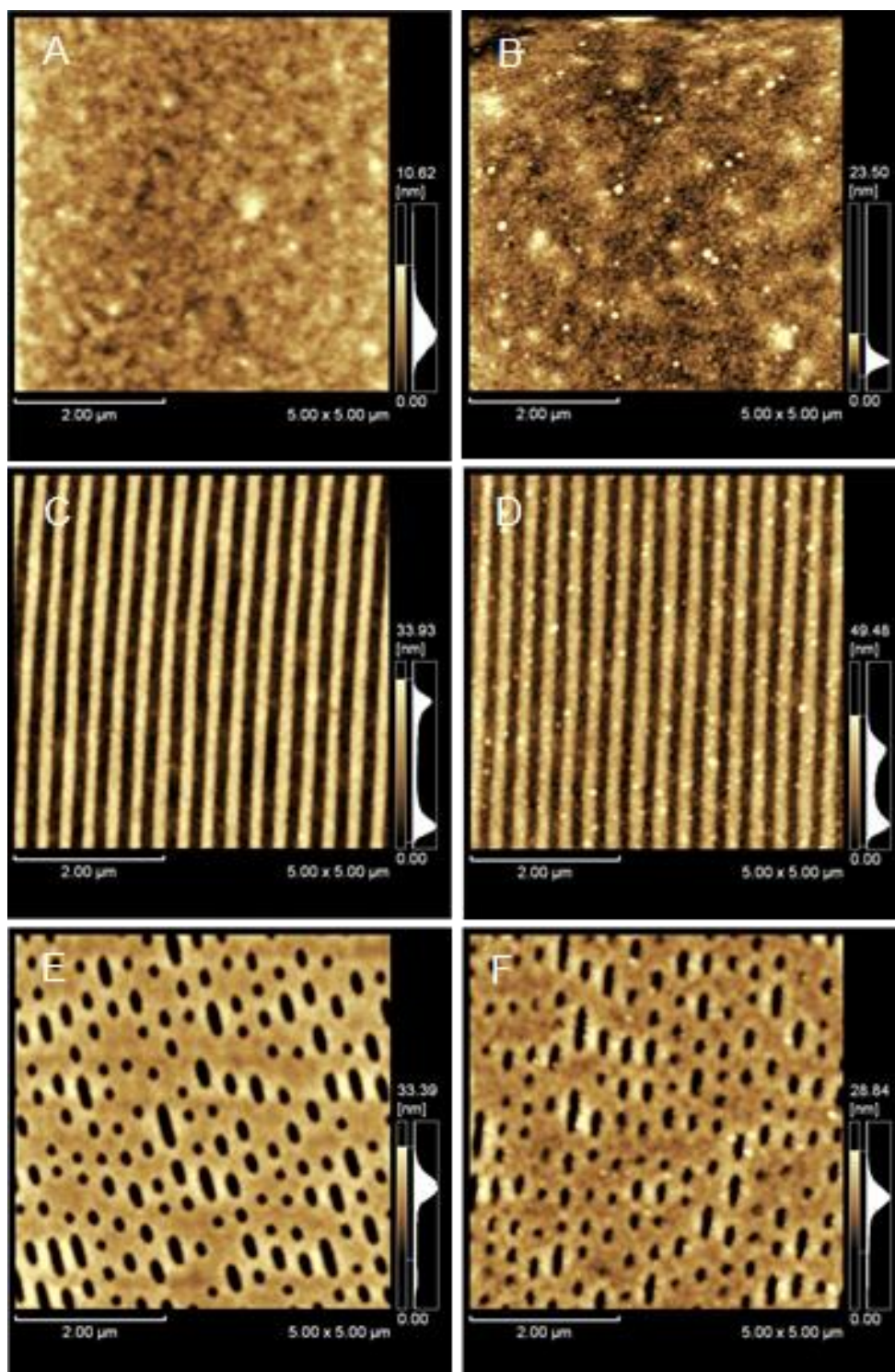


Figure 32 AFM micrographs of the surface of P3HT:PCBM film of (A) flat solar cell, (C) solar cell imprinted with BD-R grating pattern, and (E) solar cell imprinted with BD grating pattern. The AFM images of the surface of Al back electrode of (B) flat solar cell, (D) solar cell with BD-R grating pattern, and (F) solar cell with BD grating pattern.

GCSPR enhanced light tripping in solar cells

It is known that the diffraction grating structure of conductors can couple the incident light into SP [20, 23, 24]. The GCSPR excitation on the fabricated solar cells were monitored by collecting the SPR reflection spectrum as a function of wavelength at different incident angles. Figure S6, APPENDIX B, shows the SPR reflectivity curves of the solar cells with BD-R and BD structures collected from the Al electrode side. The results clearly show that the SPR excitation can be obtained as the presence of sharp dip peaks in the reflection spectra under illumination of p-polarized light. The presence of the dip can be observed at 420 nm with the incident angle of 20° . When the incident angle increases from 20° to 70° , the redshift of the dip peaks from 420 nm to 623 nm can be observed and assigned to the SPR properties of the BD-R and BD diffraction grating [20, 27]. It needs to note that, the intensity of the GCSPR excitation from the BD-R grating is stronger than those obtained from the BD, Figure S6 (B) and (D), APPENDIX B. Under irradiation of s-polarized light (without GCSPR excitation), the reflection spectra obtained from BD structure show scattering effect more than the BD-R structure as the presence of lower broad-band reflection spectra for all incident angles, Figure S6 (A) and (C), APPENDIX B. This indicates that the periodic grating structure of BD-R can couple the incident light into SP more than that of non-periodic grating structure of BD. However, the structure of BD provides the scattering more than those of BD-R. The GCSPR excitation collaborated with the absorption of the active layer of the solar cells were studied by measuring the reflection spectra from the ITO electrode side of the devices. Figure 2 shows the reflectivity curves of the fabricated devices under irradiation of p-polarized light. For the flat device, Figure 2 (A), the decrease of the reflectivity curves at 400–650 nm are attributed to the absorption of P3HT:PCBM layer which can be observed for all fabricated devices. Remarkably, the devices with BD-R and BD grating structures show the broad-band improvement of the absorption at 400–650 nm, which can be due to the scattering effect of the BD-R and BD grating structures, Figure 2 (B) and (C). Nevertheless, the GCSPR excitation could be also obtained at the active layer/aluminum grating structure interface as the presence of the dips at the wavelength longer than 650 nm. The redshift of the dip peaks from 670 nm to NIR region can be observed as the increase of the incident angle. The dip intensities obtained from the solar cell with BD-R grating structure are stronger than those of BD for all incident angles. Besides, the double dips can be observed for the reflection spectra of the BD-R solar cells. This is due to the curvature of the BD-R pattern. In addition, the BD-R patterns that were used as the master templates have the straight-line and curve-line pattern. The straight-line pattern can directly couple the incident light into GCSPR

under illumination p-polarized light. Meanwhile, the curve-line pattern can also couple the incident light into GCSPR, but at different excitation polarization. Thus, the double dips could be obtained. Another reasonable explanation is the coupling of the incident light into waveguide mode. In addition, we also studied the influence of illumination of p- and s-polarized light. Figure S7, S8, and S9, APPENDIX B, show the reflectivity curves of flat solar cell, BD-R solar cell, and BD solar cell, respectively. At the incident angle larger than 20° , the reflectivity curves show the change of the absorption of P3HT:PCBM layer at 400–650 nm when the polarization of the incident light changes from p- to s-polarization for all devices. For the BD-R and BD solar cells, the GCSPR excitation can be obtained only for p-polarized light as the existing of dip peaks. Based on these results, the effect of light scattering and GCSPR on photocurrent can be quantified.

Electrical properties of the fabricated devices

Figure 3 and Table S1, APPENDIX B, show the I-V curves and electrical parameters of the fabricated solar cells measured under illumination of non-polarized light at normal incident angle. The results clearly show the improvement of the performance for the BD-R and BD devices. By introducing the grating structure into the solar cells, the short-circuit photocurrent property was improved from the flat device with 6.07 ± 0.17 mA, to 6.68 ± 0.05 mA (11.05% improvement) and 6.41 ± 0.21 mA (10.6% improvement) for the BD-R device and the BD device, respectively. The photoconversion efficiency of the solar cells was also improved from $2.49 \pm 0.22\%$ to $2.97 \pm 0.20\%$ (19.28% improvement) for the device with BD-R pattern and $2.57 \pm 0.19\%$ (3.21% improvement) for the device with BD pattern. Note that, the nanoimprinting of the diffraction grating pattern on the surfaces of the P3HT:PCBM blended polymer did not show a significant effect on the open-circuit voltage property of the fabricated device.

Next, we studied the relationship between the electrical properties and the incident angles. Figure 4 (A) shows the relationship between the short-circuit photocurrents and the incident angles of the fabricated devices. The results clearly show the decrease of the photocurrents when the incident angle increases. This can be due to the decrease of the light intensity. The BD-R solar cell can produce higher photocurrent than the BD solar cell and the flat solar cell for all incident angles. For the BD solar cell, the improvement of the photocurrent compared with the flat device can be obtained from the incident angle of 0° to 50° . At the incident angle larger than 50° , imprinting of BD grating does not provide the significant improvement of the photocurrent compared with the flat device.

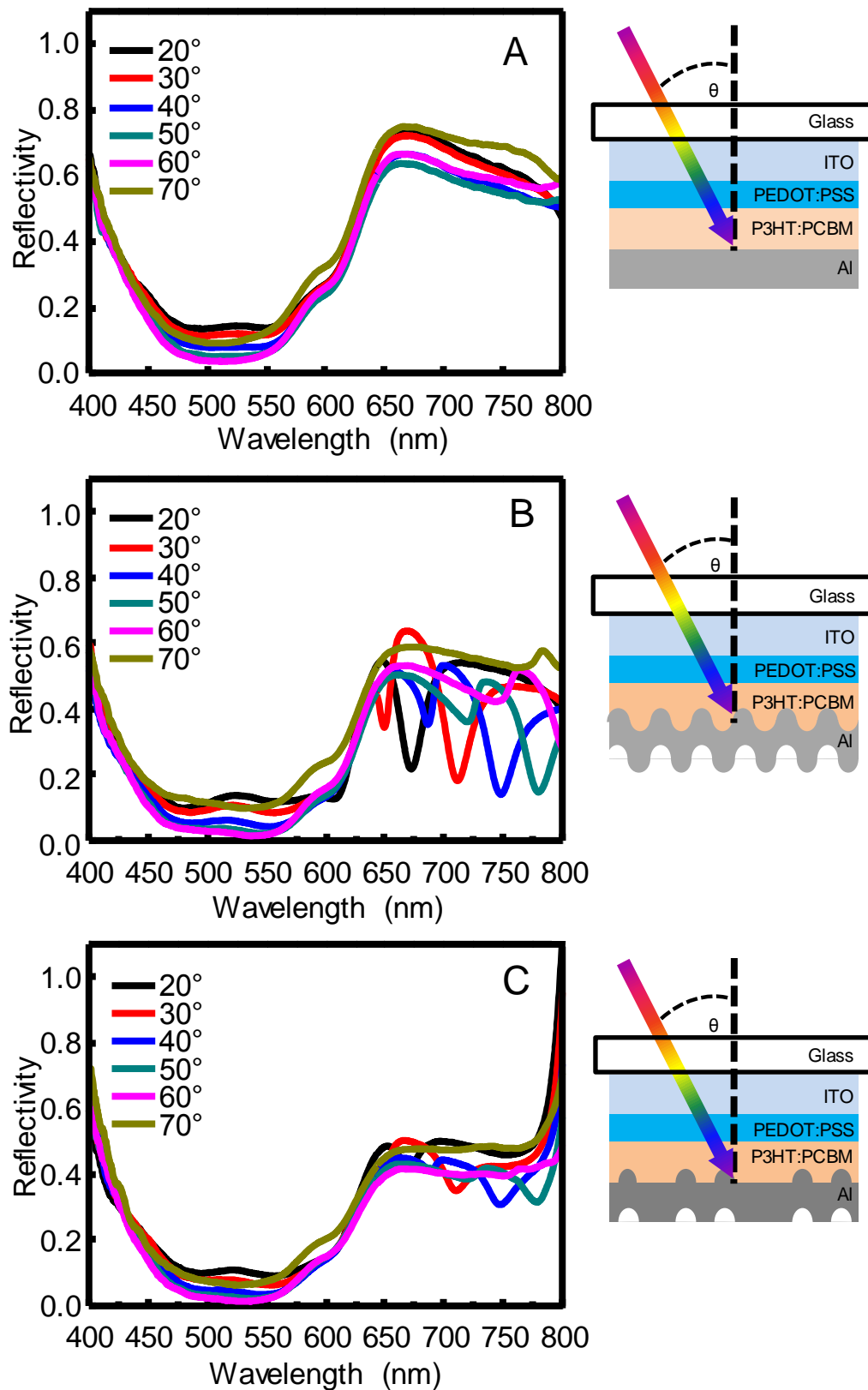


Figure 33 The SPR reflectivity curves and its schematic represented the structure of the fabricated solar cells with (A) flat solar cell (B) BD-R solar cell (C) BD solar cell. spectra were collected from ITO side under irradiation of p-polarized light.

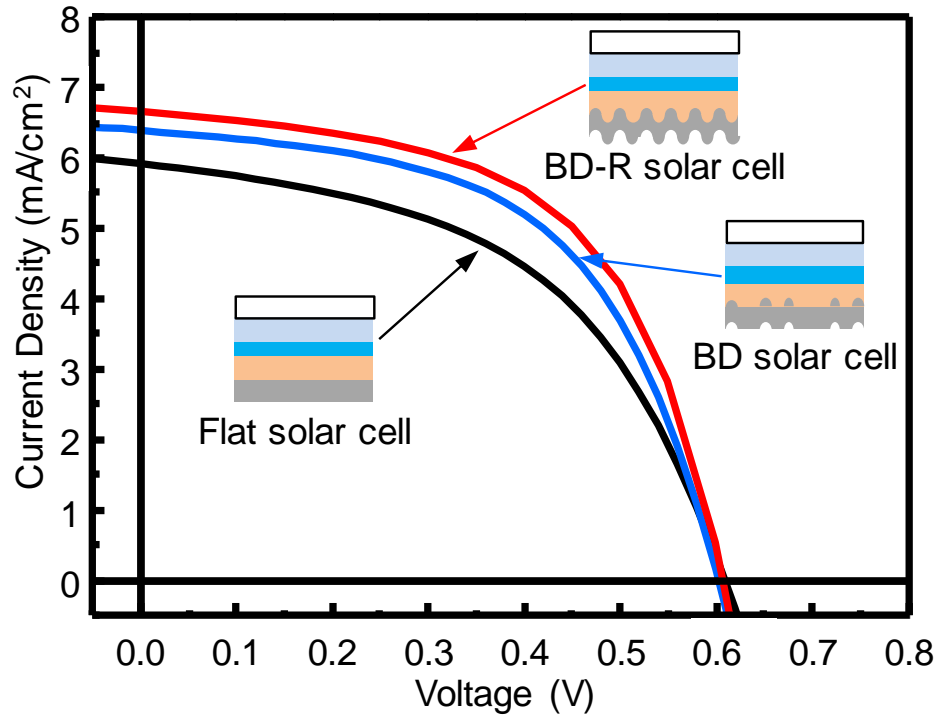


Figure 34 I-V characteristic and the schematic of the fabricated solar cells under illumination of non-polarized light with normal incident angle.

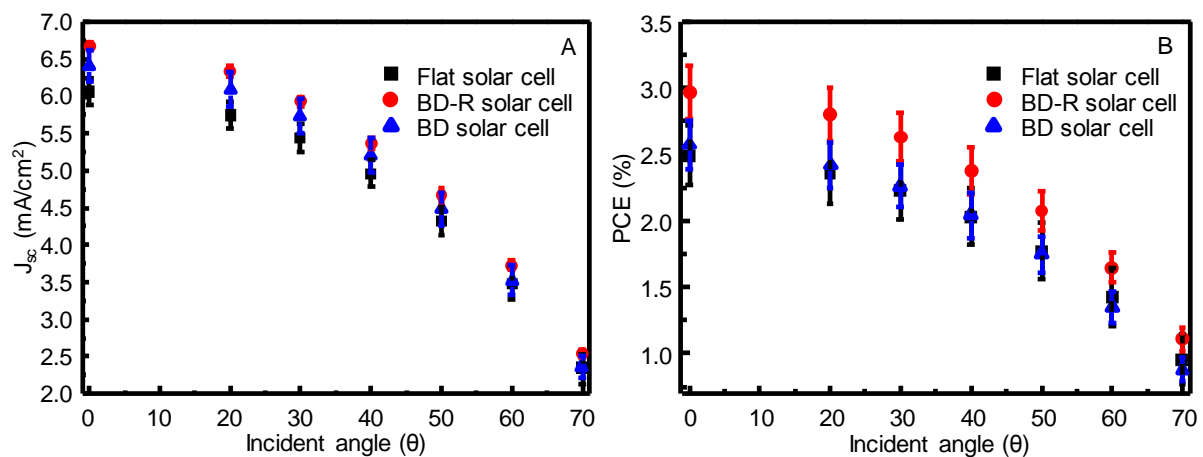


Figure 35 Relationships of (A) short-circuit photocurrent (J_{sc}) and incident angle and (B) photoconversion efficiency (PCE) and incident angle of the fabricated solar cells. The solar cells were illuminated with non-polarized light during electrical characterization.

Figure 4 (B) shows the relationship between PCE and the incident angle of the fabricated solar cell. The results show indicate the improvement of the PCE for the BD-R device compared with the flat device for all incident angle. The decrease of the PCE can be observed when the incident angle increase. For the BD solar cell, the slight improvement of

the PCE can be obtained at the incident angle of 0° and 20° . At the incident angle larger than 20° , there are no significant improvements of the PCE from the device with BD grating. Compared with the flat device, the deterioration of the PCE originated from the BD solar cell can be observed at 60° and 70° .

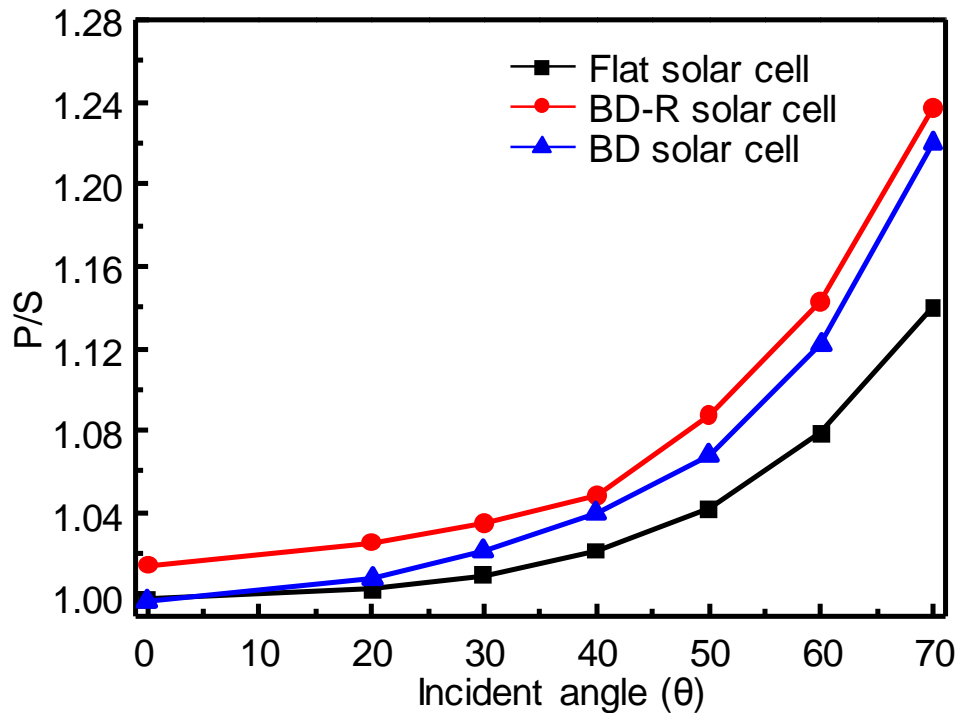


Figure 36 P/S enhancement factors of the fabricated devices. The enhancement factor is the ratio of the short-circuit photocurrent under illumination of p-polarized light to the short-circuit photocurrent under illumination of s-polarized light.

Upon the non-polarized light illumination, GCSPR excited by the p-polarization component in non-polarized light can be obtained for the BD-R and BD devices. Thus, the overall photocurrents obtained from BD-R and BD devices are the combination between the photocurrent with GCSPR and the photocurrent without GCSPR. To evaluate the effect of GCSPR on the generation of photocurrent, we conducted the measurement of photocurrent under illumination of polarized light at various incident angles. Figure S10 shows the short-circuit photocurrents at various incident angles of the fabricated devices under illumination of s- and p-polarized light. We calculated the enhanced factor p/s , which is the ratio of the photocurrent with SP excitation (p-polarization) to the photocurrent without SP excitation (s-polarization). Figure 5 shows the enhancement factor p/s of the photocurrent at various incident angles. At normal angle of incidence, only the BD-R device provides $\sim 2\%$ increase of the photocurrent when the polarization of the incident light change from s- to p-

polarization. At 20° , the change of the photocurrents is observed for the BD-R and BD devices. Based on the reflection spectra of the fabricated devices, Figure S7, S8, and S9, APPENDIX B, the GCSPPR excitation can be obtained for the BD-R and BD. Note that, the change of the absorption originated from the light scattering effect does not occur when the polarization of the incident light change from s- to p-polarization for all devices. Thus, the increase of the photocurrent observed in the BD-R and BD device could be due to the effect of the GCSPPR of the diffraction grating. At the incident angle larger than 30° , for the BD-R and BD devices, the increase of the photocurrents are observed and assigned to the increase of the light absorption originated from the change of light scattering properties of s- and p-polarized light inside the solar cells, and GCSPPR. For the flat device, the change of the photocurrent originates from the difference of the light scattering properties of s- and p-polarized light.

Enhancement of incident photon-to-current efficiency

To gain more understanding how GCSPPR enhances the performance of the organic solar cell, we conducted the incident photon to current conversion efficiency (IPCE) experiment under illumination of non-polarized light. The IPCE enhancement factor, which is the ratio of the IPCE of the device with grating to the flat device, was evaluated. Figure 6 shows IPCE enhancement spectra of the BD-R and BD solar cells. The results clearly show that the IPCE enhancement spectra consists of 3 enhancement regions, included i) The IPCE enhancement that was observed at 400–450 nm and might be attributed to the LSPR [28], ii) The IPCE enhancement by light scattering effect at 450–650 nm, and iii) The IPCE enhancement by GCSPPR of Al grating at 650–830 nm. For the IPCE enhanced by GCSPPR, we observed a broadband enhancement peak from 650–830 nm at normal incident angle. When we increase the incident angle to 20° , a sharp enhancement peak is observed at 675 nm. The redshift of the enhancement peak from 675 to 839 nm is observed when increase the incident angle from 20° to 70° . In addition, as show in Figure 6, BD-R and BD grating structure provide the difference IPCE enhancement pattern. Compared with the BD, the BD-R grating structures provide the IPCE enhancement by GCSPPR more than the BD. Meanwhile, the BD grating structure shows the better enhancement by the light scattering effect.

To confirm the enhancement of the IPCE of the solar cells by GCSPPR, we conducted the measurement of the spectral photocurrent under illumination of polarized light. We find the IPCE enhancement spectra p/s by the calculation of the ratio between the IPCE with the

SP excitation (p-polarization) and without SP excitation (s-polarization). Figure 7 shows the IPCE enhancement spectra p/s of the fabricated solar cells. For the flat device, the results show only the IPCE enhancement by the light scattering corresponding to the change of the reflection pattern of the flat device when the polarization of the incident light change from s- to p-polarization, Figure S7, APPENDIX B. The GCSPR enhanced IPCE can be obtained from the solar cells with BD-R and BD grating structures as the appearance of the incident angle dependent enhancement peaks at the wavelength longer than 650 nm under illumination of p-polarized light.

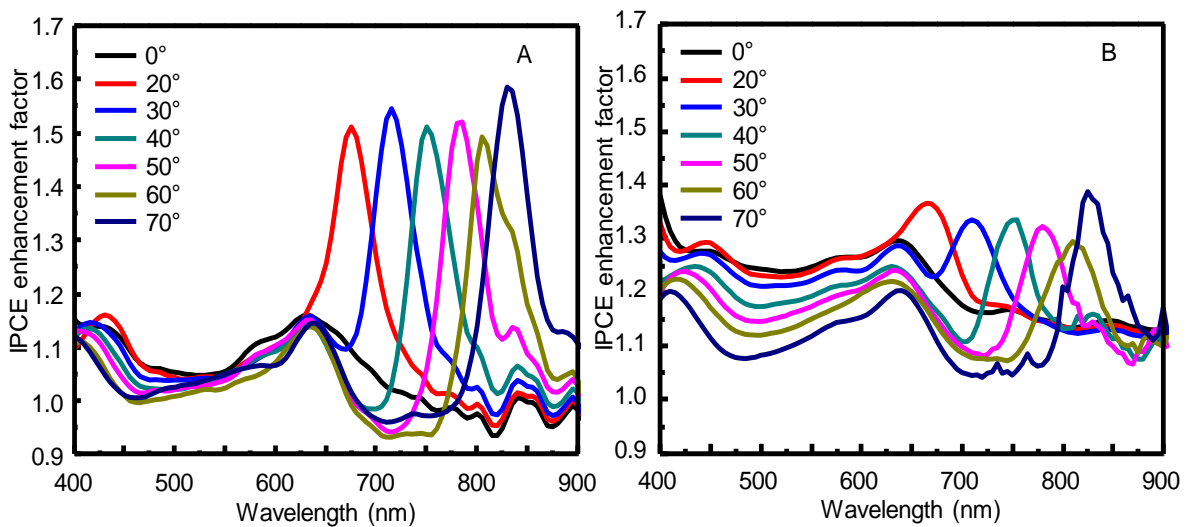


Figure 37 IPCE enhancement spectra of (A) BD-R solar cell and (B) BD solar cell under illumination of non-polarized light. The IPCE enhancement is the ratio of the IPCE of imprinted device to the IPCE of the flat device.

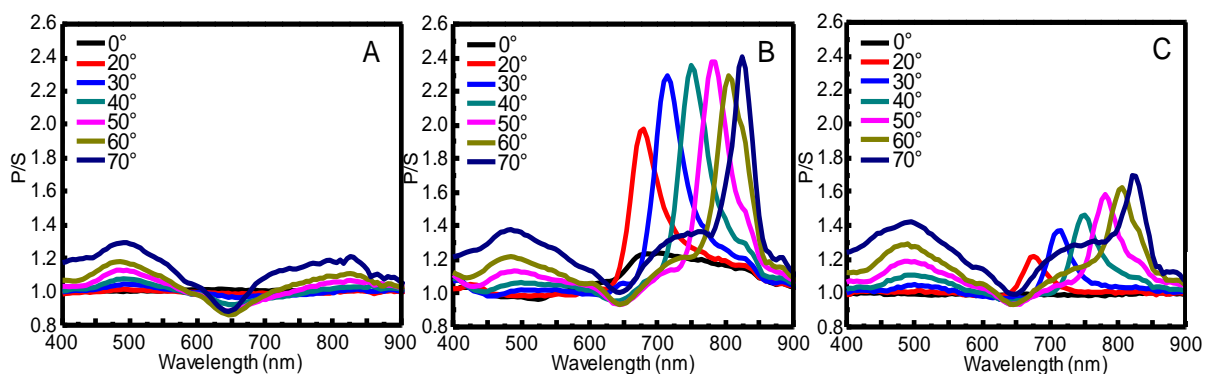


Figure 38 IPCE enhancement spectra P/S of (A) flat solar cell, (B) BD-R solar cell, and (C) BD solar cell. The IPCE enhancement p/s is the ratio between the IPCE with the SP excitation (p-polarization) and without SP excitation (s-polarization).

Evaluation of the enhancement of incident photon to current conversion efficiency by GCSPR

Our results in previous section are clearly show that the introduction of the BD-R and BD diffraction grating into the solar cells delivers the enhancement of the photocurrent properties as well as the efficiency via light scattering and GCSPR effect. In addition, the difference of the morphology of diffraction grating influences the appearance of light diffraction property and the ability to couple the incident light into SP. We individually study about the enhancement originating from light scattering and GCSPR effect, compared between the BD solar cell and BD-R solar cell. We conducted the IPCE experiment under illumination of non-polarized light. The incident angles were fixed at 0° and 20° in order to avoid the decrease of the intensity of the incident light when irradiated at the large incident angles. Figure 8 shows IPCE spectra of BD and flat solar cells. The results clearly show the improvement of the IPCE at 400–650 nm on the BD solar cell. In addition, the P3HT:PCBM blended polymer express the characteristic light absorption at 400–650 nm, Figure S7-S9, APPENDIX B. Thus, it is reasonable to explain that the increase of the IPCE in this region can be attributed to the increase of effective light path inside the device due to the light scattering by BD grating structure. Moreover, we observed the increase of the IPCE spectrum at the wavelength of 650–675 nm in the BD device compared with the flat solar under illumination at normal incident angle. The IPCE of BD at 650–675 region slightly increase when the angle of illumination change from 0° to 20° corresponding to the present of GCSPR excitation dip peak of the BD solar cell at the incident angle of 20° as shown in Figure 2 (C). Thus, we recognized that the GCSPR of the BD grating could enhance the IPCE of the solar cell.

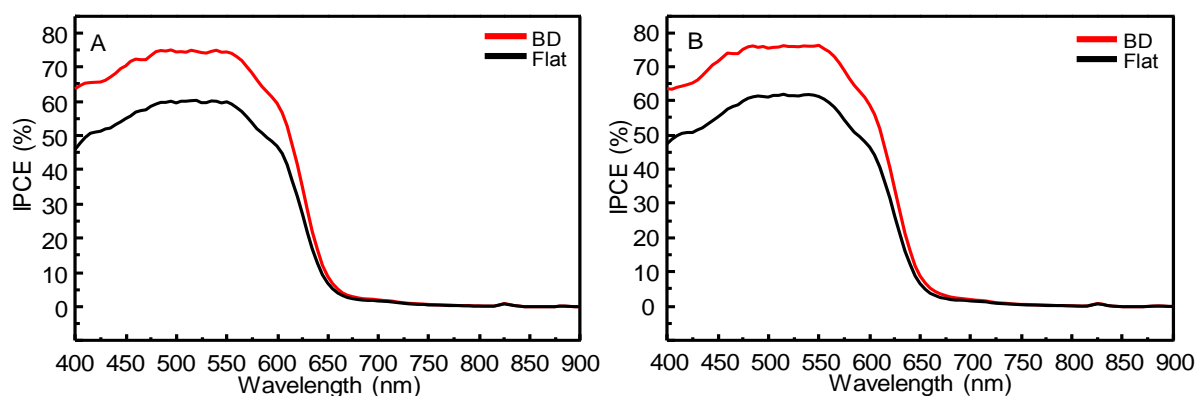


Figure 39 IPCE spectra of the BD and flat solar cells irradiated with non-polarized light at the incident angle of (A) 0° and (B) 20° .

For the BD-R solar cell, we observed the same enhancement pattern of the IPCE as we observed in the BD devices. However, compared with the BD solar cell, the BD-R device provides the smaller improvement of the IPCE in 400–650 nm, Figure 9. When the incident angle increase from 0° to 20° , the increase of the IPCE spectra of the BD–R can be observed and attributed to the effect of the GCSPR of BD-R grating.

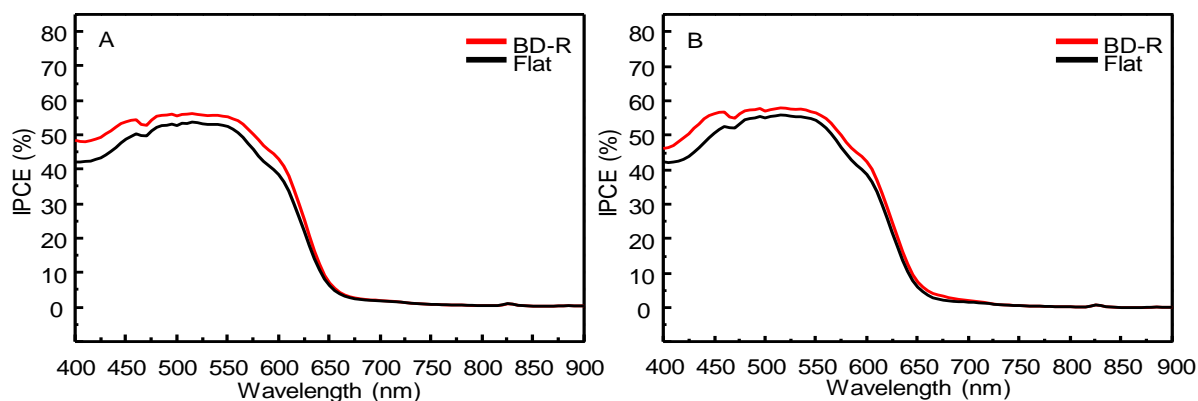


Figure 40 IPCE spectra of the BD-R and flat solar cells irradiated with non-polarized light at the incident angle of (A) 0° and (B) 20° .

Consider to the IPCE spectra of those fabricated solar cells, Figure 8 and 9, the improvement of the IPCE observing in the BD and BD-R solar cells is the cooperative effect between light scattering and GCSPR. The results show that the scattering effect plays the major role while the GCSPR provides just the minor role in the overall IPCE enhancement, Figure 6 to 9. The BD grating structure provides the higher light scattering effect while the BD-R grating delivers higher GCSPR. In addition, the GCSPR excitation wavelengths of the BD and BD-R devices are located out of the absorption region of the P3HT:PCBM, Figure 2. This might be the main reason that why the GCSPR play the minor effect on the enhancement of the performance of the solar cells. Thus, it is very interesting to estimate how much GCSPR involve in the generation of photocurrent.

We calculated the percentage of the IPCE integration area at 400–650 nm and 650–900 nm which match to the IPCE enhancement regions inducing by light scattering and GCSPR, respectively. This could be implied the effective illumination wavelength for the production of photocurrent of the solar cell. Figure S11 and S12, APPENDIX B, show the curves of IPCE integration area as the function of illumination wavelength. The percentages of the integration area of the IPCE spectra were calculated show in Table S2 and S3, APPENDIX B. The results show that more than 97% of the photocurrents of the fabricated

solar cells are produced under illumination of 400–650 nm corresponding to the absorption peak of the P3HT:PCBM. For the BD device, a 1.89% of the photocurrent is generated in the region of 650–900 nm under illumination at normal incident angle. An insignificant increase of the generation of the photocurrent was observed when the incident angle increase from 0° to 20° . In the case of BD-R solar cell, we observed the higher generation of the photocurrent in the same illumination wavelength. The significant increase of the photocurrent creation from 2.04% to 2.35% were obtained when the incident angle change from 0° to 20° .

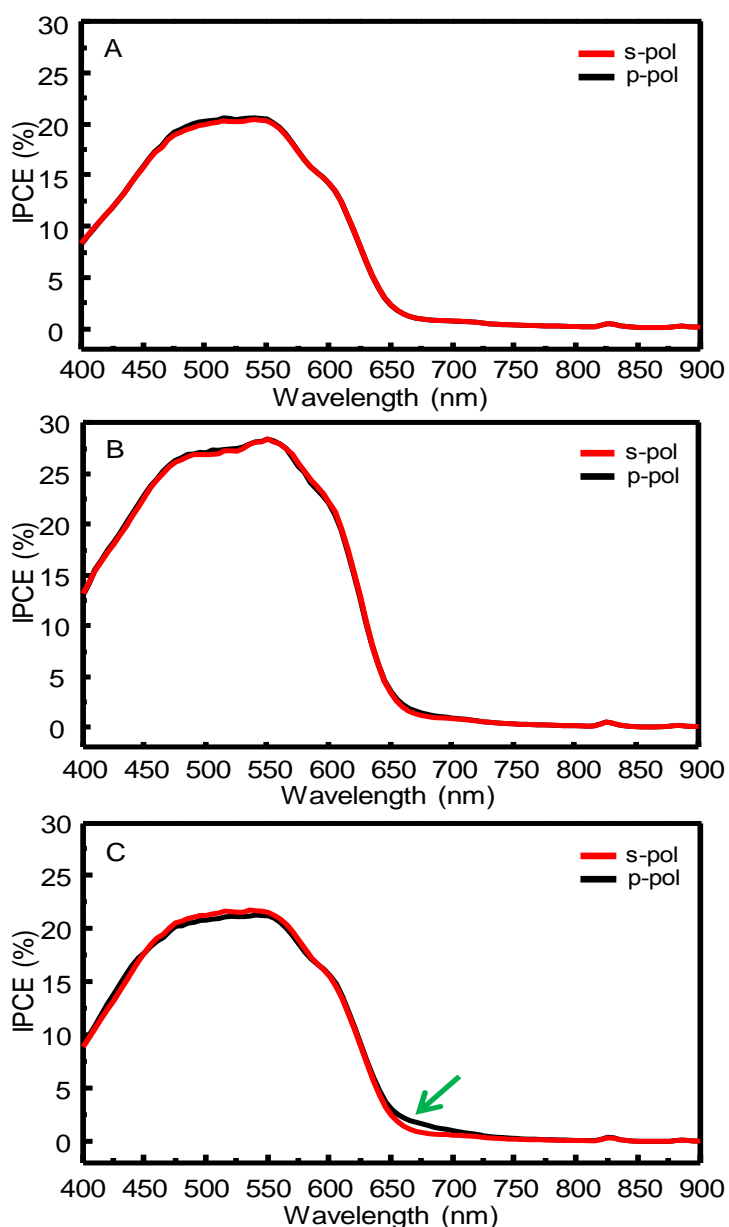


Figure 41 IPCE spectra of (A) flat solar cell, (B) BD solar cell, and (C) BD-R solar cells under illumination of polarized light at the incident angle of 20° . The arrow in (C) indicates the increase of the IPCE enhancement by GCSPR.

To gain more insight about the GCSPR enhanced the photocurrent generation of the solar cells, we conducted the IPCE measurement under illumination of polarized light. The angle of illumination was fixed at 20°. Figure 10 show the IPCE spectra obtained from the experiment. The percentage of integration area calculated from the IPCE spectra were calculated and showed in Table 1. For the flat solar cell, we did not observe the significant change of the photocurrent generation in the region of 650–900 nm when the polarization of the incident light changes from s- to p-polarization. For the imprinted devices, we observed a 1.12% and a 0.21% increase of the photocurrent production for BD-R and BD solar cells, respectively. Moreover, the results show that the BD-R solar cell offers the highest photocurrent generation under illumination of 650 –900 nm with GCSPR excitation with the amount up to 3.30% of overall produced photocurrent.

Table 3 The percentage of integration area calculated from the IPCE spectra of the fabricated devices under illumination of polarized light at the incident angle of 20°.

Device, at 20°	% Integration area (%)	
	400–650 nm	650–900 nm
Flat, s-pol	97.52	2.48
Flat, p-pol	97.55	2.45
BD-R, s-pol	97.78	2.22
BD-R, p-pol	96.70	3.30
BD, s-pol	97.76	2.24
BD, p-pol	97.57	2.43

 -0.03 %
 +1.12 %
 +0.21 %

CONCLUSIONS

We investigated the GCSPR effect that can enhance the performance of organic photovoltaic cells. BD-R and BD grating structure was created on the active layer using pressure-less nanoimprinting technique. The SP reflectivity curves of the fabricated devices clearly showed the improvement of light absorption in the device with BD-R and BD structures compared with the flat device due to the light scattering and GCSPR of the grating structures. The results clearly showed that the introducing metal grating to the photovoltaic device benefited the improvement of photocurrent as well as the efficiency. The improvement

of the photocurrents from the BD-R and BD solar cells are 11.05% and 10.6%, respectively, while the BD-R and BD solar cell provide the enhancement of the PCE for 19.28% and 3.21%, respectively. The IPCE results clearly show that the scattering effect plays the major role while the GCSPR provides just the minor role in the overall IPCE enhancement. By comparison of BD and BD-R diffraction grating, the results show the difference of enhancement characteristic of the performance of the solar cell. The BD grating structure provides the higher light scattering enhancement while the BD-R grating delivers the better GCSPR enhancement. The results of this study deliver the greater understanding of these systems which benefit as the basic knowledge to the enhancement of photocurrent intensity in high performance solar harvesting application in the future.

REFERENCES

1. Singh, R.P. and O.S. Kushwaha, *Polymer Solar Cells: An Overview*. Macromolecular Symposia, 2013. **327**(1): p. 128-149.
2. Tada, K., K. Hosoda, M. Hirohata, R. Hidayat, T. Kawai, M. Onoda, et al., *Donor polymer (PAT6) — acceptor polymer (CNPPV) fractal network photocells*. Synth. Met., 1997. **85**(1–3): p. 1305-1306.
3. Yu, G. and A.J. Heeger, *Charge separation and photovoltaic conversion in polymer composites with internal donor/acceptor heterojunctions*. J. Appl. Phys., 1995. **78**(7): p. 4510-4515.
4. Halls, J.J.M., C.A. Walsh, N.C. Greenham, E.A. Marseglia, R.H. Friend, S.C. Moratti and A.B. Holmes, *Efficient photodiodes from interpenetrating polymer networks*. Nature, 1995. **376**(6540): p. 498-500.
5. Günes, S., H. Neugebauer and N.S. Sariciftci, *Conjugated Polymer-Based Organic Solar Cells*. Chem. Rev., 2007. **107**(4): p. 1324-1338.
6. Mayer, A.C., S.R. Scully, B.E. Hardin, M.W. Rowell and M.D. McGehee, *Polymer-based solar cells*. Mater. Today, 2007. **10**(11): p. 28-33.
7. Han, K.-S., J.-H. Shin, W.-Y. Yoon and H. Lee, *Enhanced performance of solar cells with anti-reflection layer fabricated by nano-imprint lithography*. Sol. Energy Mater. Sol. Cells, 2011. **95**(1): p. 288-291.
8. Forberich, K., G. Dennler, M.C. Scharber, K. Hingerl, T. Fromherz and C.J. Brabec, *Performance improvement of organic solar cells with moth eye anti-reflection coating*.

- Thin Solid Films, 2008. **516**(20): p. 7167-7170.
9. Rim, S.-B., S. Zhao, S.R. Scully, M.D. McGehee and P. Peumans, *An effective light trapping configuration for thin-film solar cells*. Appl. Phys. Lett., 2007. **91**(24): p. -.
 10. Lu, L., Z. Luo, T. Xu and L. Yu, *Cooperative Plasmonic Effect of Ag and Au Nanoparticles on Enhancing Performance of Polymer Solar Cells*. Nano Lett., 2012. **13**(1): p. 59-64.
 11. Chen, F.-C., J.-L. Wu, C.-L. Lee, Y. Hong, C.-H. Kuo and M.H. Huang, *Plasmonic-enhanced polymer photovoltaic devices incorporating solution-processable metal nanoparticles*. Appl. Phys. Lett., 2009. **95**(1): p. -.
 12. Notarianni, M., K. Vernon, A. Chou, M. Aljada, J. Liu and N. Motta, *Plasmonic effect of gold nanoparticles in organic solar cells*. Solar Energy, 2014. **106**(0): p. 23-37.
 13. Hsiao, Y.-S., S. Charan, F.-Y. Wu, F.-C. Chien, C.-W. Chu, P. Chen and F.-C. Chen, *Improving the Light Trapping Efficiency of Plasmonic Polymer Solar Cells through Photon Management*. J. Phys. Chem. C, 2012. **116**(39): p. 20731-20737.
 14. Kalfagiannis, N., P.G. Karagiannidis, C. Pitsalidis, N.T. Panagiotopoulos, C. Gravalidis, S. Kassavetis, P. Patsalas and S. Logothetidis, *Plasmonic silver nanoparticles for improved organic solar cells*. Sol. Energy Mater. Sol. Cells, 2012. **104**(0): p. 165-174.
 15. Atwater, H.A. and A. Polman, *Plasmonics for improved photovoltaic devices*. Nat Mater, 2010. **9**(3): p. 205-213.
 16. You, J., X. Li, F.-x. Xie, W.E.I. Sha, J.H.W. Kwong, G. Li, W.C.H. Choy and Y. Yang, *Surface Plasmon and Scattering-Enhanced Low-Bandgap Polymer Solar Cell by a Metal Grating Back Electrode*. Advanced Energy Materials, 2012. **2**(10): p. 1203-1207.
 17. An, C.J., C. Cho, J.K. Choi, J.-M. Park, M.L. Jin, J.-Y. Lee and H.-T. Jung, *Highly Efficient Top-Illuminated Flexible Polymer Solar Cells with a Nanopatterned 3D Microresonant Cavity*. Small, 2014. **10**(7): p. 1278-1283.
 18. Pala, R.A., J.S.Q. Liu, E.S. Barnard, D. Askarov, E.C. Garnett, S. Fan and M.L. Brongersma, *Optimization of non-periodic plasmonic light-trapping layers for thin-film solar cells*. Nat Commun, 2013. **4**.
 19. Li, X., W.C.H. Choy, L. Huo, F. Xie, W.E.I. Sha, B. Ding, et al., *Dual Plasmonic Nanostructures for High Performance Inverted Organic Solar Cells*. Adv. Mater., 2012. **24**(22): p. 3046-3052.
 20. Homola, J., *Surface Plasmon Resonance Sensors for Detection of Chemical and Biological Species*. Chem. Rev., 2008. **108**(2): p. 462-493.
 21. Homola, J., S.S. Yee and G. Gauglitz, *Surface plasmon resonance sensors: review*.

- Sensors Actuators B: Chem., 1999. **54**(1–2): p. 3-15.
22. Smith, A.J., C. Wang, D. Guo, C. Sun and J. Huang, *Repurposing Blu-ray movie discs as quasi-random nanoimprinting templates for photon management*. Nat Commun, 2014. **5**: p. 5517.
 23. Baba, A., N. Aoki, K. Shinbo, K. Kato and F. Kaneko, *Grating-Coupled Surface Plasmon Enhanced Short-Circuit Current in Organic Thin-Film Photovoltaic Cells*. ACS Appl. Mater. Interfaces, 2011. **3**(6): p. 2080-2084.
 24. Baba, A., K. Wakatsuki, K. Shinbo, K. Kato and F. Kaneko, *Increased short-circuit current in grating-coupled surface plasmon resonance field-enhanced dye-sensitized solar cells*. J. Mater. Chem., 2011. **21**(41): p. 16436-16441.
 25. Zhao, J., A. Swinnen, G. Van Assche, J. Manca, D. Vanderzande and B.V. Mele, *Phase Diagram of P3HT/PCBM Blends and Its Implication for the Stability of Morphology*. J. Phys. Chem. B, 2009. **113**(6): p. 1587-1591.
 26. Yang, Y., K. Mielczarek, M. Aryal, A. Zakhidov and W. Hu, *Nanoimprinted Polymer Solar Cell*. ACS Nano, 2012. **6**(4): p. 2877-2892.
 27. Homola, J., I. Koudela and S.S. Yee, *Surface plasmon resonance sensors based on diffraction gratings and prism couplers: sensitivity comparison*. Sensors Actuators B: Chem., 1999. **54**(1–2): p. 16-24.
 28. Baba, A., K. Imazu, A. Yoshida, D. Tanaka and K. Tamada, *Surface plasmon resonance properties of silver nanoparticle 2D sheets on metal gratings*. SpringerPlus, 2014. **3**(1): p. 284.

CHAPTER IV

CONCLUSIONS

SP is a promising method to couple the incident light into the surface of the conductor via the interaction against the electrons at the surface of the conductor. The SP provides the intense near-field near the surface of the conductor. This can be act as near-field light source for the applications of photocatalyst and photovoltaic. Thus, we have studied and developed the system that uses the LSPR property of AuNPs and GCSPR to enhance the photocatalytic activity of TiO₂ under UV-Visible illumination. AuNPs were created on TiO₂ surfaces by a simple chemical reduction using NaBH₄ as a reducer to obtain AuNP-TiO₂ nanocomposites. The catalytic activity of this material was investigated by measuring the short-circuit photocurrent originated from water-splitting reaction catalyzed by AuNP-TiO₂ nanocomposites film under UV-Visible illumination. The results show that the photocurrent of the nanocomposite photocatalyst electrode can be enhanced by LSPR property of plasmonic AuNPs with the appropriate concentration of AuNPs in the nanocomposites of 0.5% Au-TiO₂ as this ratio gave the highest photocurrent signal. The excess doping amounts of gold in the AuNP-TiO₂ nanocomposites caused the decrease the photocurrent properties. The EIS results indicate that the improvement in the photocurrent can be the reason of the enhancement of electron-hole pair generation induced by the LSPR of AuNPs instead of the extension of the electron lifetime. Moreover we have showed the novel method to enhance the photocatalytic property of TiO₂ using the combination of LSPR of plasmonic AuNPs and GCSPR of gold grating. The results indicated the further improvement of the photocurrent of AuNP-TiO₂ nanocomposite film can be obtained from GCSPR gold grating. This suggests that the photocatalytic activity of TiO₂ can be enhanced by multiple plasmonic effects. The study provides a greater understanding of LSPR and GCSPR enhanced photocurrent in photocatalyst. For the use of SP in solar harvesting application, we have studied the GCSPR enhanced the performance of thin-film organic photovoltaic cells. BD-R and BD grating structure was created on the active layer using pressure-less nanoimprinting technique. The SP reflectivity curves of the fabricated devices clearly showed the improvement of light trapping light in the device with BD-R and BD structures compared with the flat device. The improvement of trapping light can be attributed to the effects of i) light scattering by the diffraction grating which can be observed as the increase of broad band absorption at 400-

650 nm. ii) The GCSPR which can be observed as the shape dip peaks at the wavelength longer than 650 nm. By introducing the BD-R and BD grating, at normal incident angle, the photocurrents increase for 11.05% and 10.6%, for the BD-R and BD device, respectively. Moreover the BD-R and BD solar cells provide the PEC enhancement for 19.28% and 3.21%, respectively.

SUGGESTIONS FOR FUTURE WORK

1. LSPR and GCSPR for photocatalyst application
 - 1.1 We have investigated the effect of LSPR of spherical AuNPs on the photocatalytic property of TiO₂. To gain more understanding about the effect of LSPR of plasmonic AuNPs on TiO₂, variation of the shape of AuNPs for example rod, wire, and prism, should be consider.
 - 1.2 The effect of other plasmonic metal nanoparticles, for example silver nanoparticles, should be investigated.
 - 1.3 Other photocatalyst, for example ZnO should be studied.
2. GCSPR for photocatalyst application
 - 2.1 We have investigated the GCSPR enhanced thin film solar cells using only 2-D grating structures. The 3-D grating structure should be considered.
 - 2.2 The influent of the thickness of the active layer should be studied.
 - 2.3 The cooperative effect of LSPR of plasmonic nanoparticles and GCSPR of metallic grating should be studied.

APPENDICES

APPENDIX A

SUPPORTING INFORMATION FOR CHAPTER II

**Investigation of localized surface plasmon/grating-coupled
surface plasmon enhanced photocurrent in TiO₂ thin films**

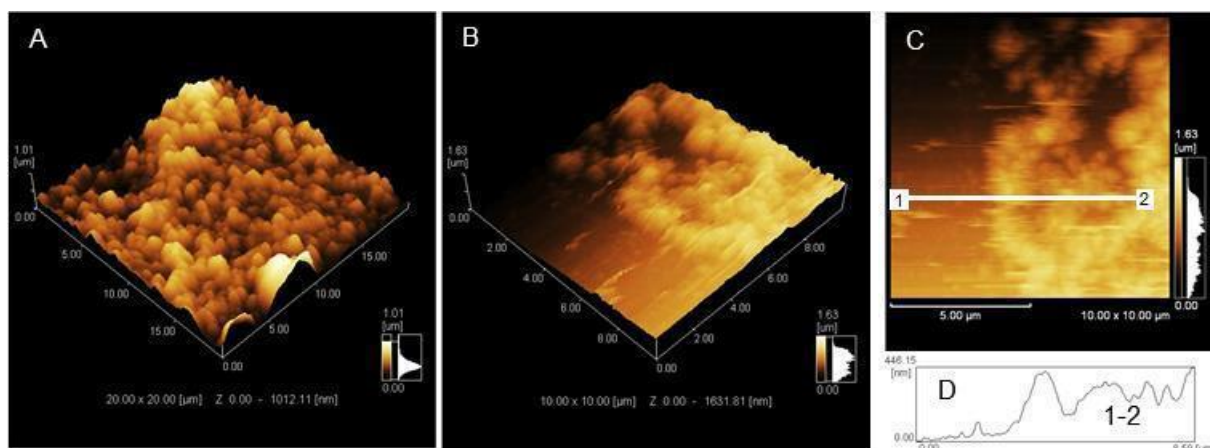


Figure S1 (A) The AFM micrograph of the AuNP–TiO₂ nanocomposites coated on an ITO-glass substrate. (B) and (C) are the AFM micrograph at the scratch edge on the film of the AuNP–TiO₂ nanocomposites. (D) The cross section profile corresponded to the line 1-2 in in (C)

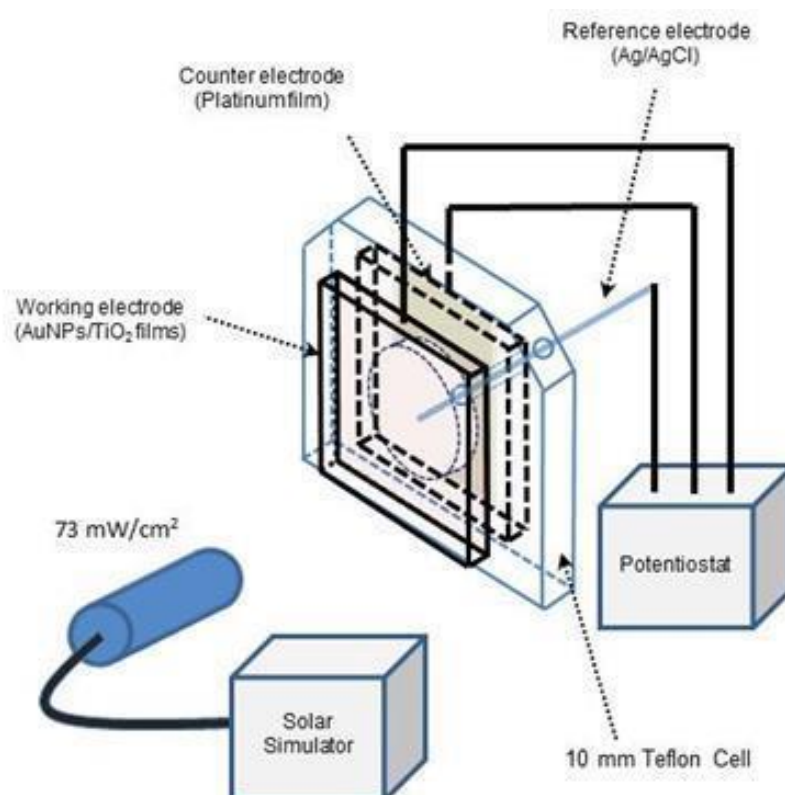


Figure S2 The photocurrent measurement apparatus for the AuNP–TiO₂ nanocomposites coated on ITO-glass substrates.

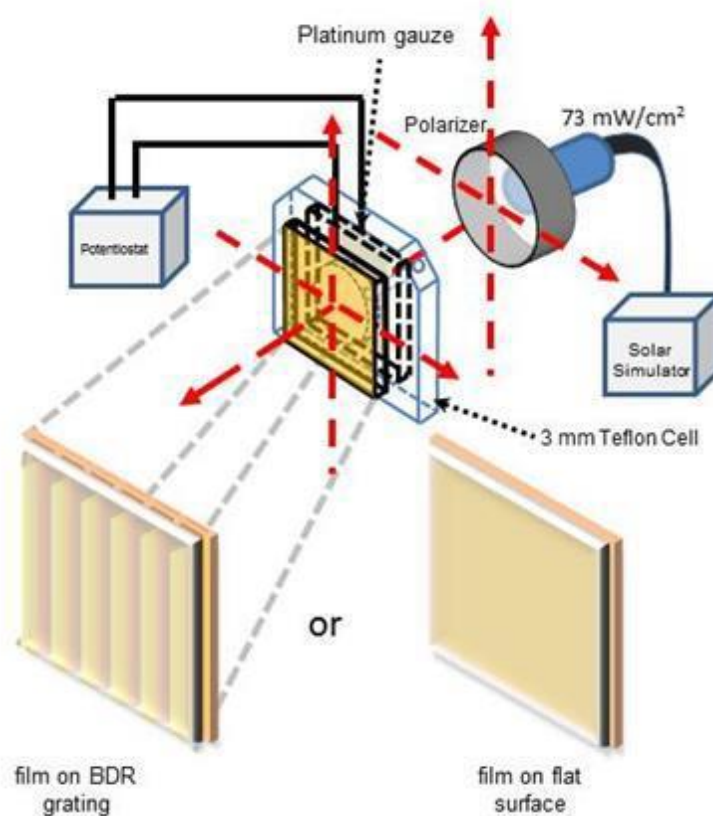


Figure S3 The photocurrent measurement apparatus for the AuNP–TiO₂ nanocomposites coated on gold grating pattern.

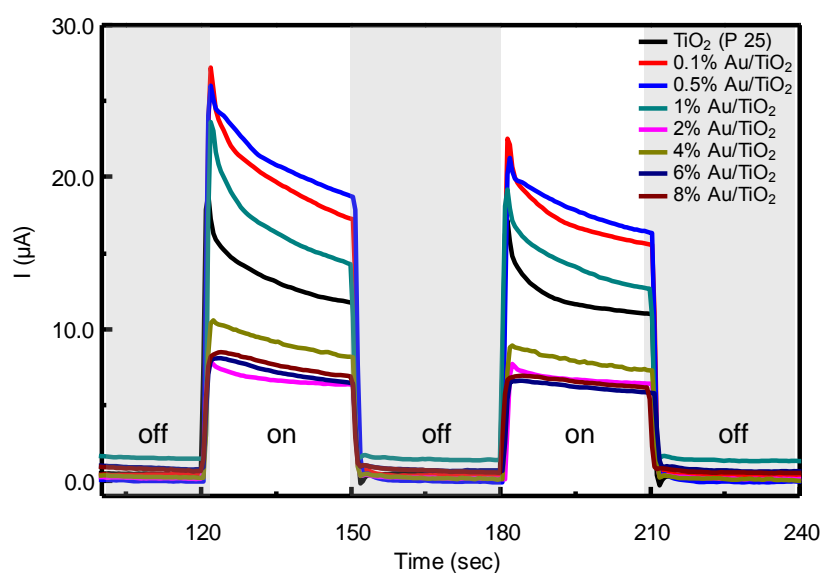


Figure S4 Short-circuit photocurrent TiO₂ and AuNP–TiO₂ nanocomposites with various amount of percentage Au/TiO₂ with and without white light illumination.

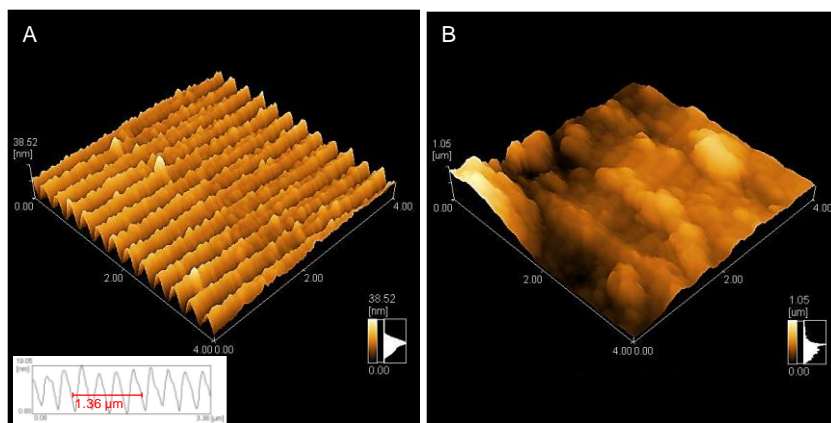


Figure S5 (A) The AFM micrograph of a bare gold grating substrate. The inset in (A) indicates the grating pitch of 330 nm. (B) The AFM micrograph of fabricated TiO_2 /gold grating.

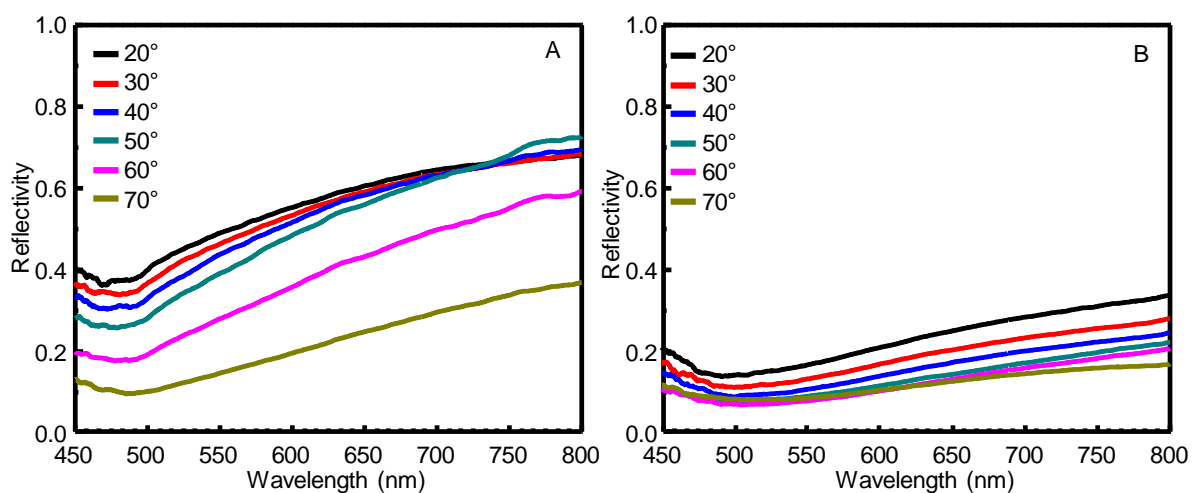


Figure S6 The SPR reflectivity curves of (A) TiO_2 /gold grating photocatalyst electrode and (B) AuNPs- TiO_2 nanocomposites/gold grating photocatalyst electrode irradiated with s-polarization.

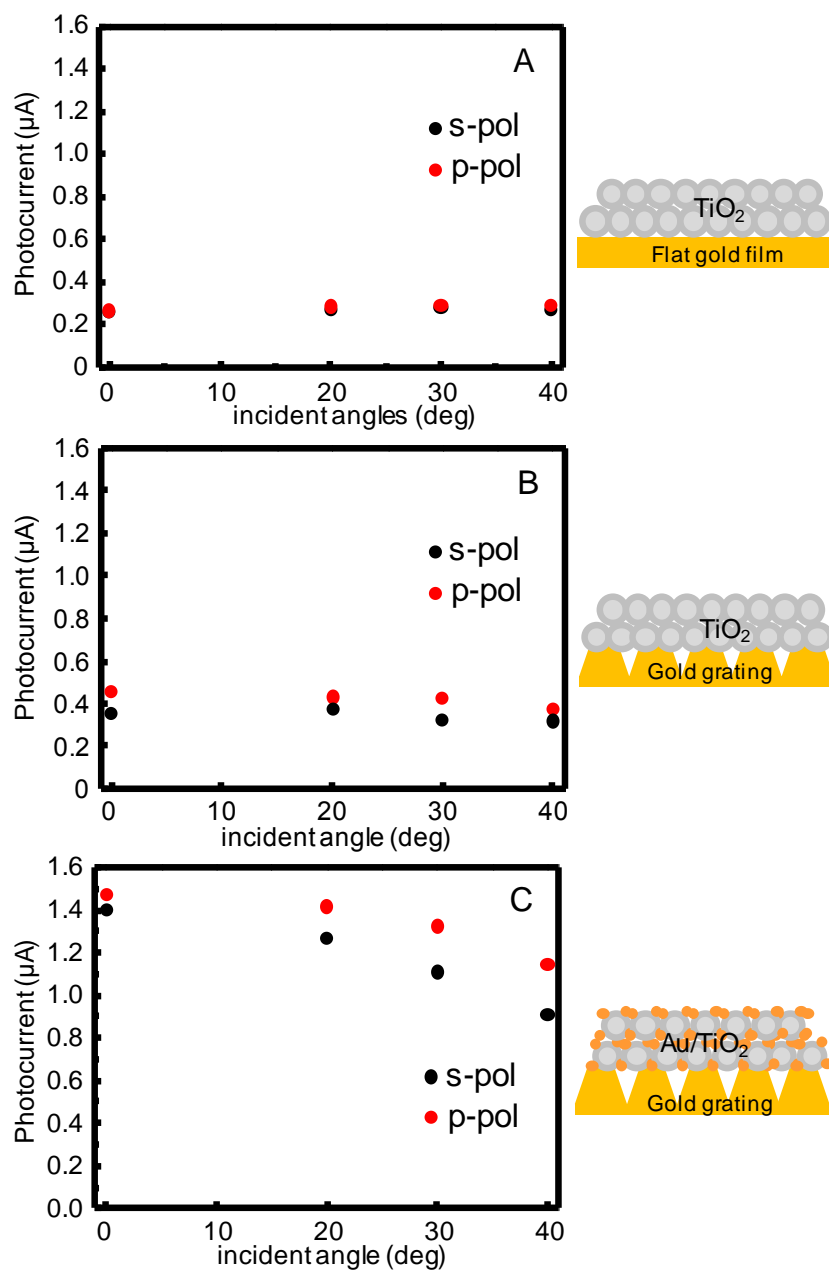


Figure S7 The short-circuit photocurrent of (A) TiO₂/flat gold, (B) TiO₂/gold grating, and (C) AuNP-TiO₂ nanocomposites/gold grating compared between s- and p-polarization .

APPENDIX B

SUPPORTING INFORMATION FOR CHAPTER III

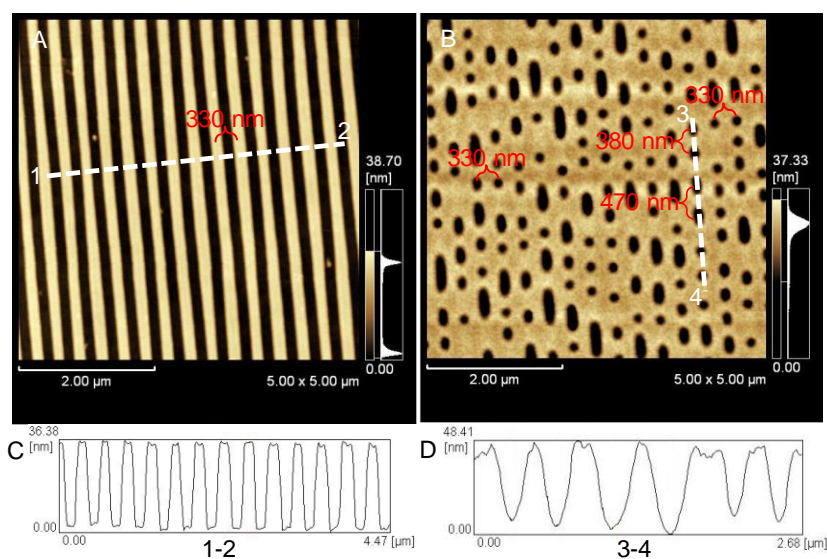


Figure S8 The AFM images of cleaned (A) BD-R and (B) BD substrate. (C) and (D) The cross section profile corresponded to the line 1-2 and 3-4 in (A) and (B), respectively

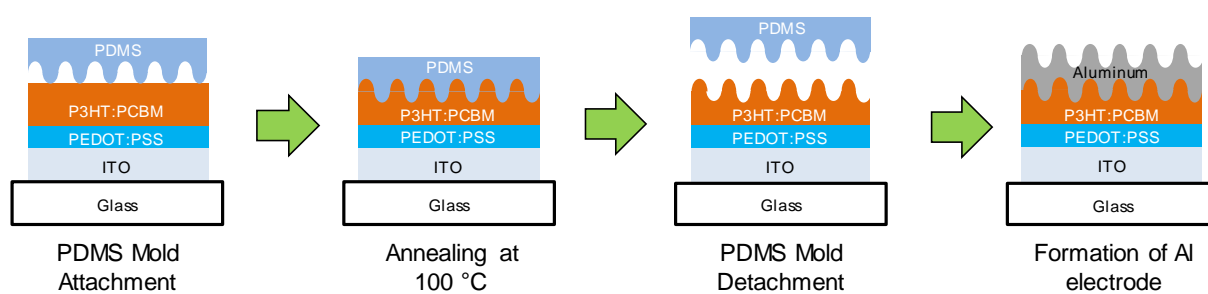


Figure S9 Schematic illustrates the fabrication of the solar cell with diffraction grating pattern on the active layer.

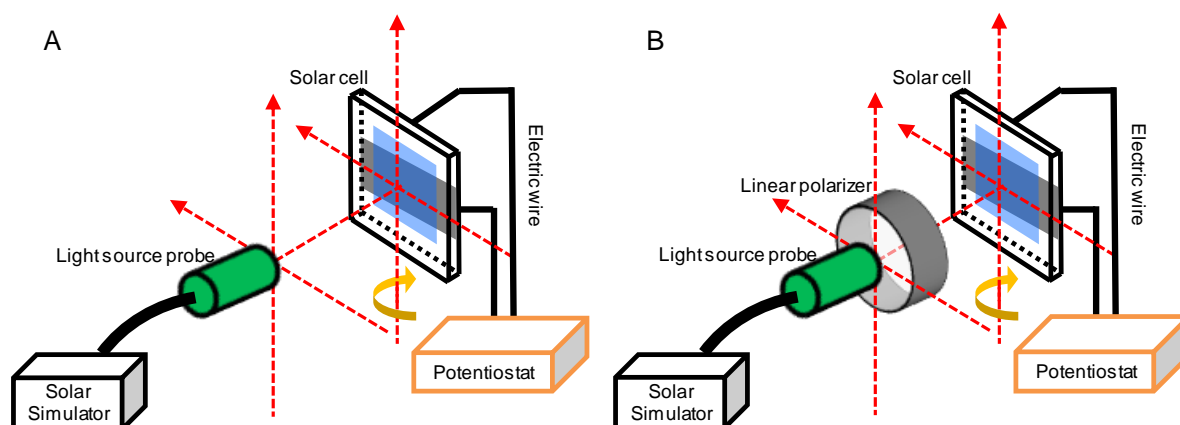


Figure S10 The photocurrent measurement apparatus for the AuNP–TiO₂ nanocomposites coated on gold grating pattern.

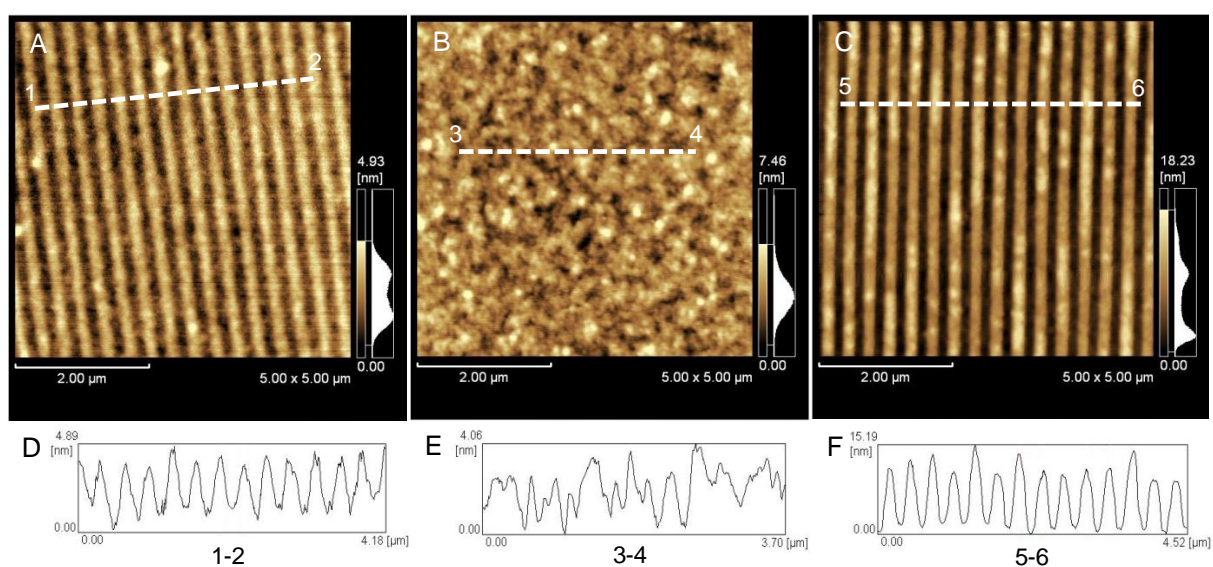


Figure S11 The AFM images of P3HT:PCBM films imprinting of BD-R pattern with different imprinting condition. (A) BD-R imprinting on the damp P3HT:PCBM film without thermal annealing, (B) BD-R imprinting on the dried P3HT:PCBM film without thermal annealing, and (C) BD-R imprinting on the dried P3HT:PCBM film with thermal annealing at 100 °C for 30 minutes.

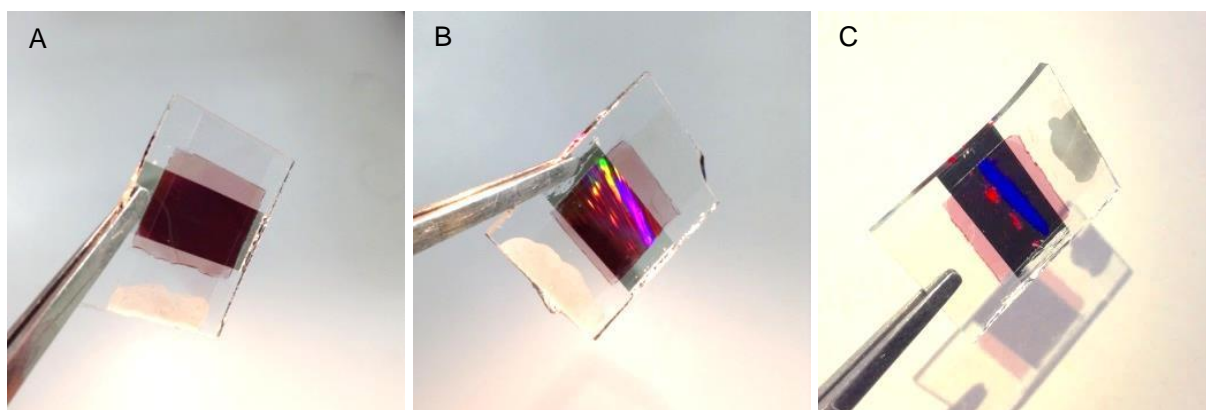


Figure S12 Digital photographs demonstrate the iridescent scattering of (A) a reference solar cell, (B) a solar cell with BD-R grating pattern, and (E) a solar cell with BD grating pattern.

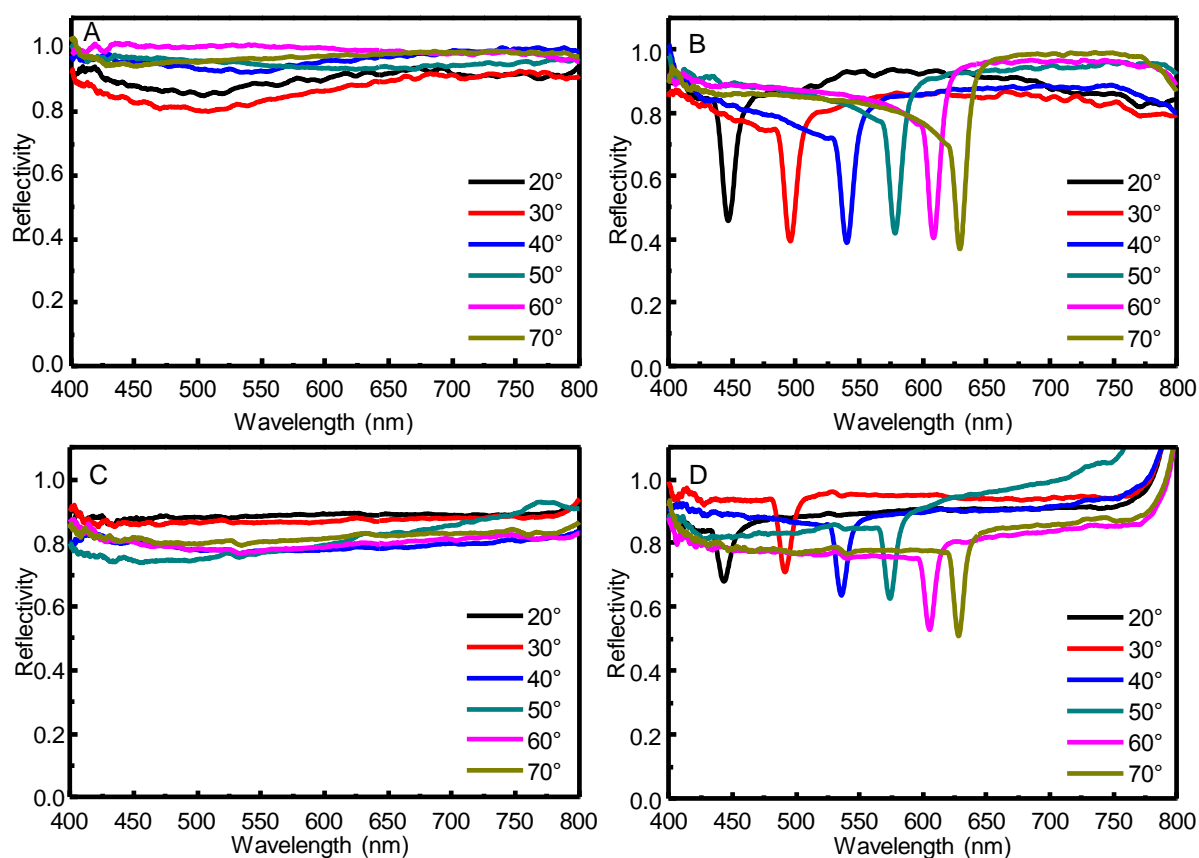


Figure S13 SPR reflectivity curves of the solar cell with periodic grating structure irradiated with (A) s-polarized and (B) p-polarized light. The SPR reflectivity curves of the solar cell with random grating structure irradiated with (E) s-polarized and (F) p-polarized light. The SPR reflectivity spectra were collected from the Al electrode side.

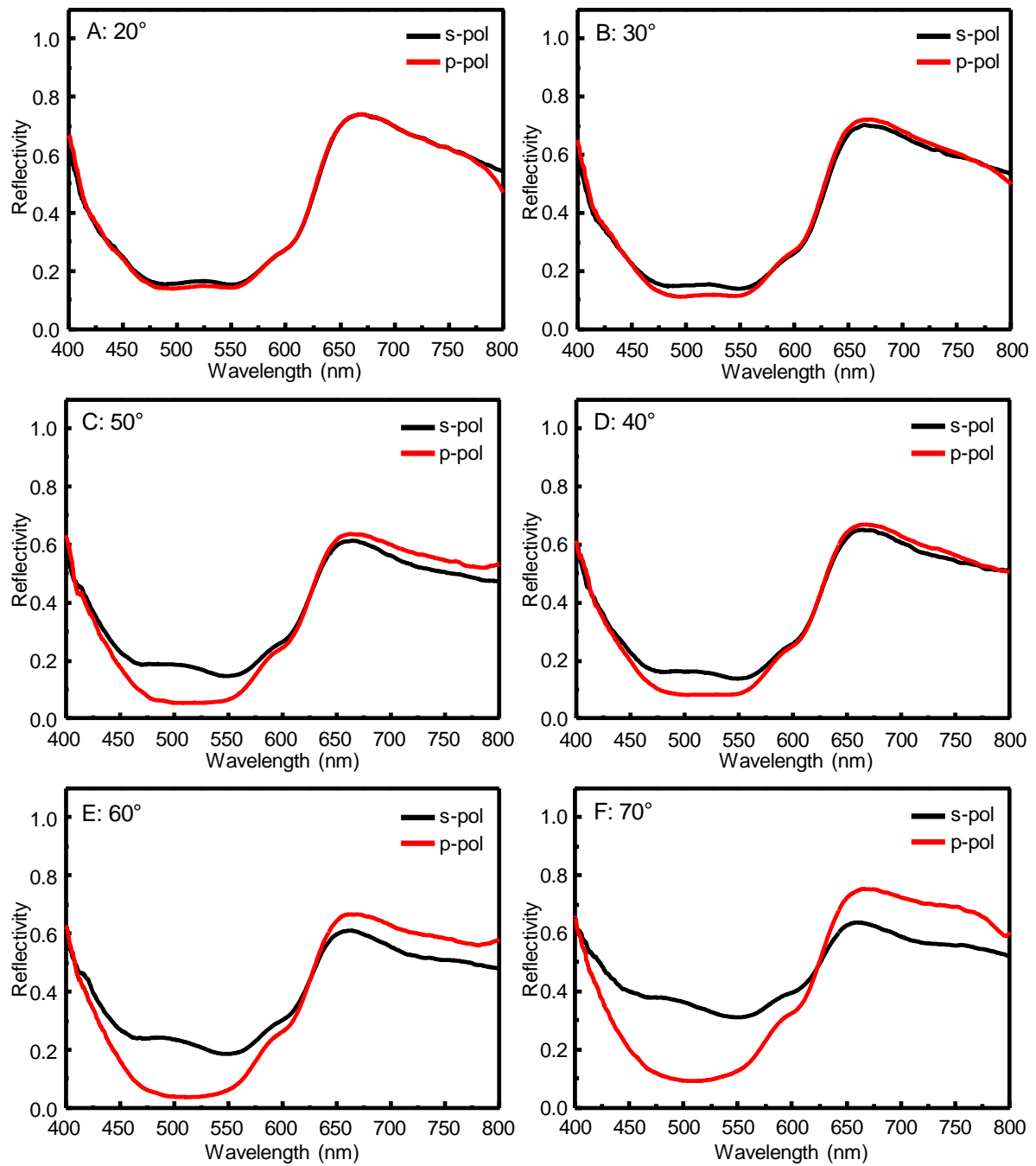


Figure S14 The reflectivity curves of the flat solar cell measured at different incident angles at (A) 20°, (B) 30°, (C) 40°, (D) 50°, (E) 60°, and (F) 70°.

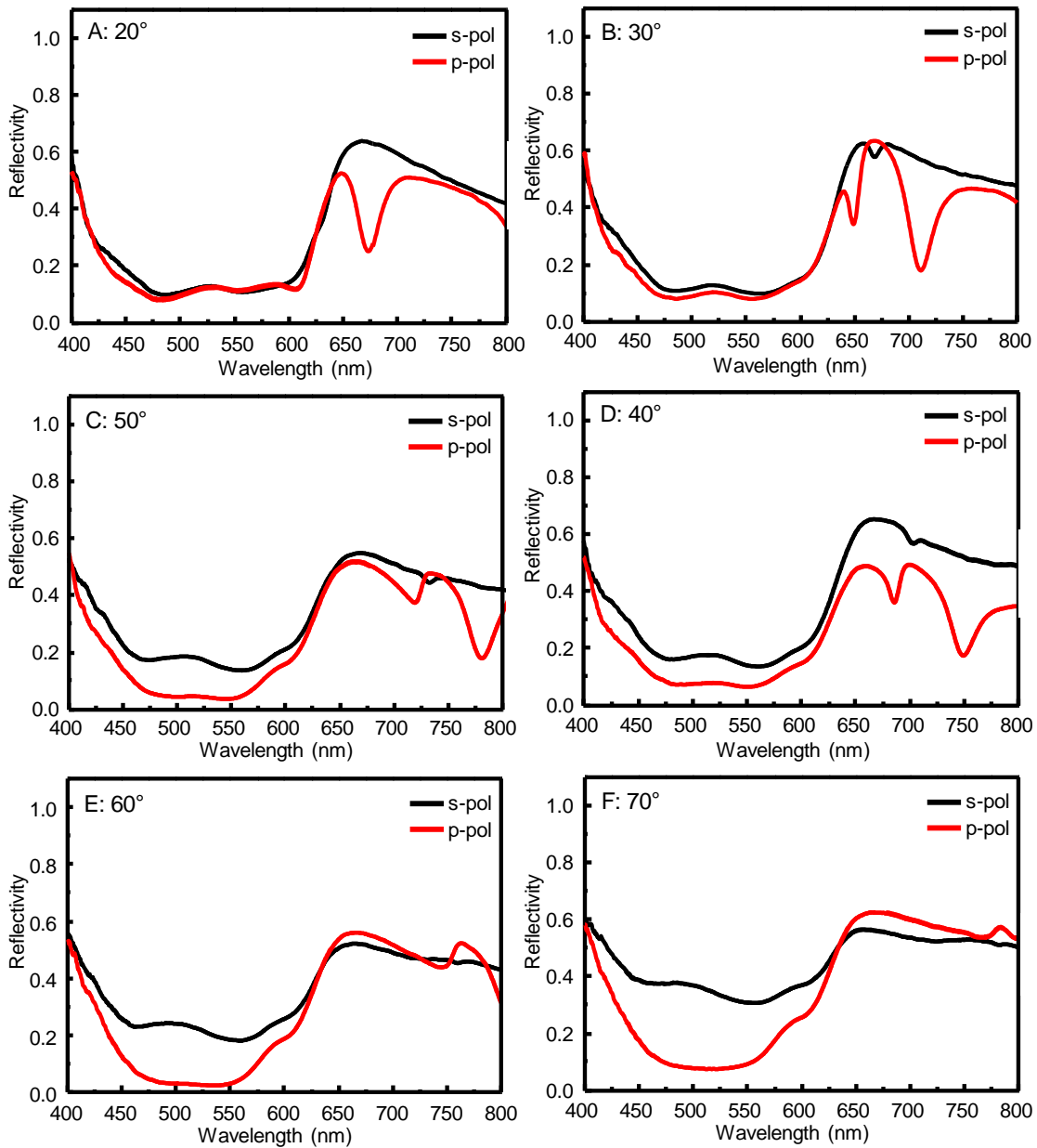


Figure S15 The reflectivity curves of the BD-R solar cell measured at different incident angles at (A) 20°, B) 30°, (C) 40°, (D) 50°, (E) 60°, and (F) 70°.

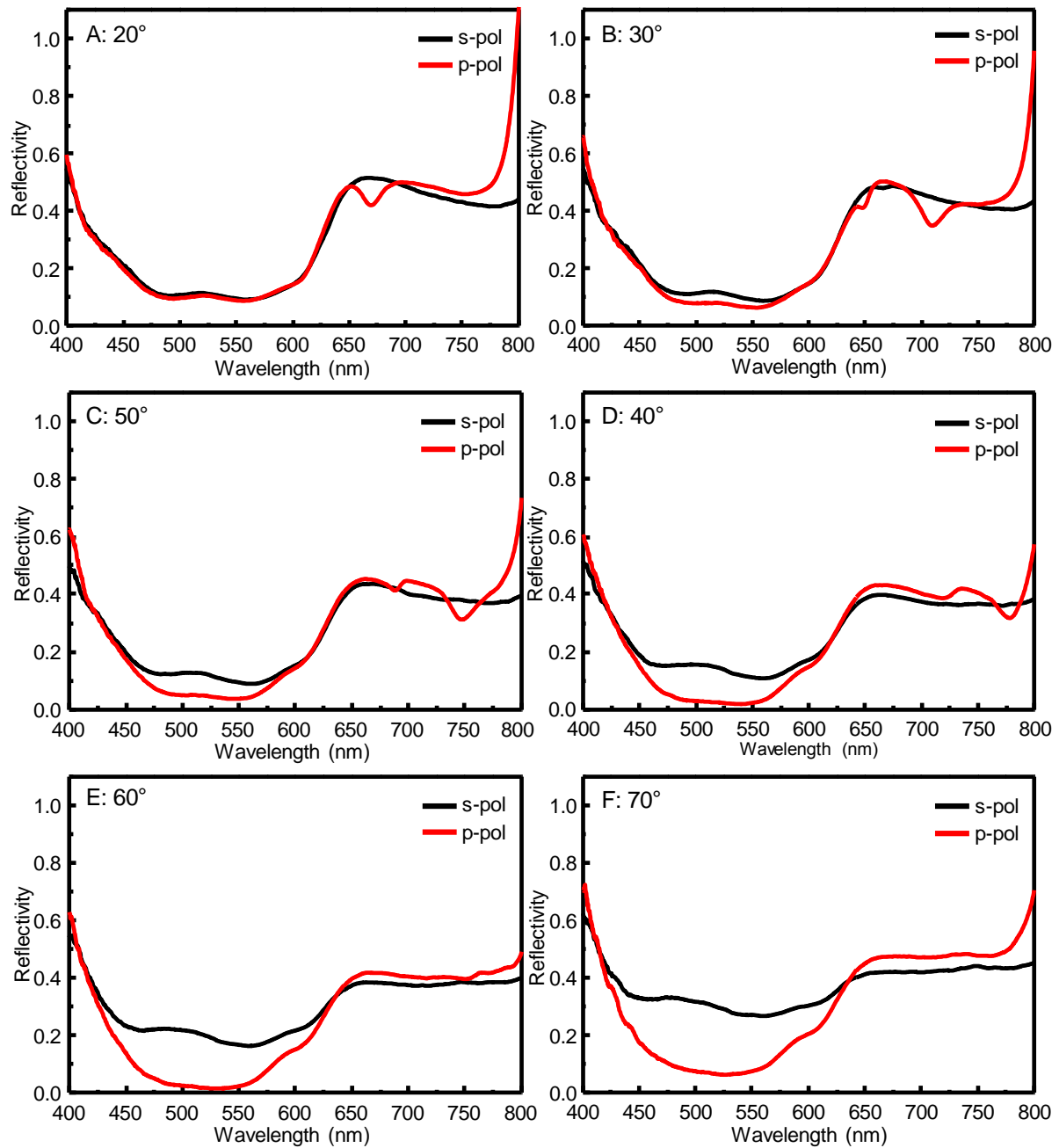


Figure S16 The reflectivity curves of the BD solar cell measured at different incident angles at (A) 20°, (B) 30°, (C) 40°, (D) 50°, (E) 60°, and (F) 70°.

Table S4 The electrical parameter of the fabricated solar cell included J_{sc} , V_{oc} , PCE, and FF. The electrical parameters were measured at normal incident angle with irradiation of non-polarized light.

Device	J_{sc} (mA/cm ²)	V_{oc} (vol)	PCE (%)	FF (%)
Flat	6.07±0.17	0.59±0.02	2.49±0.22	0.54±0.04
BD-R	6.68±0.05	0.60±0.02	2.97±0.20	0.57±0.03
BD	6.41±0.21	0.60±0.01	2.57±0.19	0.50±0.04

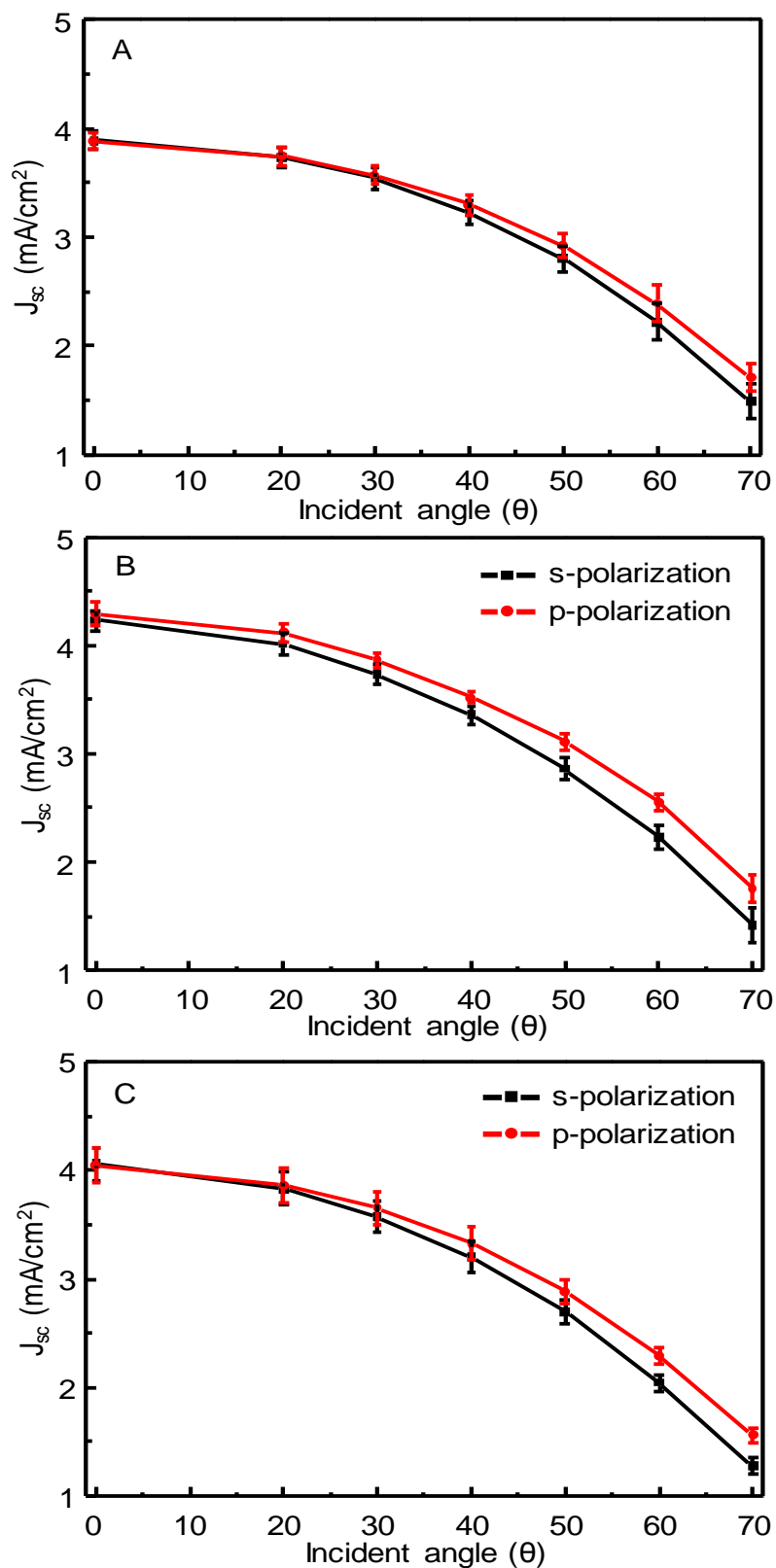


Figure S17 The short-circuit photocurrent obtained from various incident angles of (A) flat solar cell, (B) BD-R solar cell, and (C) BD solar cell under irradiation of s- and p-polarized light.

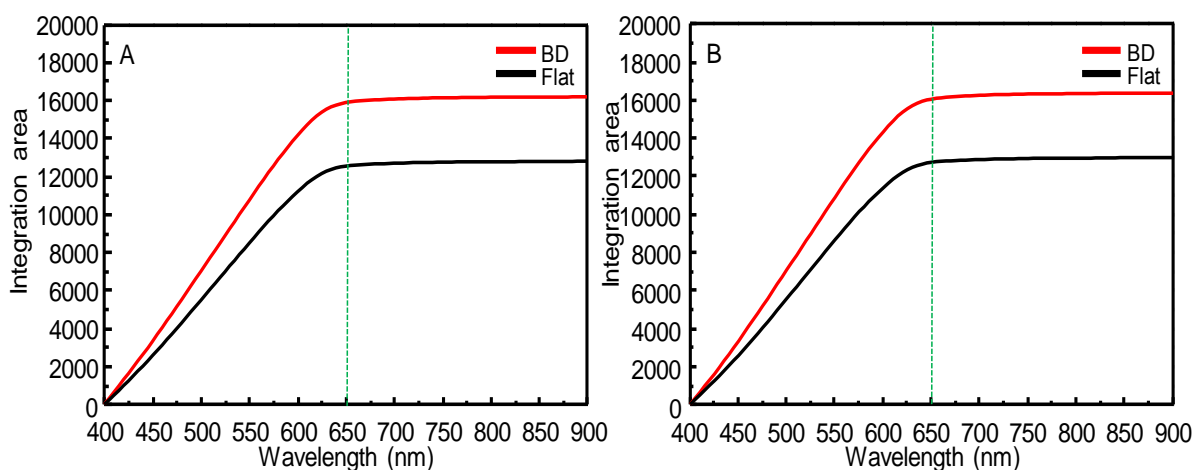


Figure S18 The relationship between the IPCE integration area and scanning wavelength of BD solar cell and flat solar cell at the incident angle of (A) 0° and (B) 20°. The solar cells were irradiated by non-polarized light.

Table S5 The percentage of IPCE integration area calculated from the IPCE spectra of BD solar cell and flat solar cell at the incident angle of 0° and 20° under illumination of non-polarized light.

Devices	% Integration area (%)	
	400–650 nm	650–900 nm
Flat, at 0°	98.02	1.98
BD, at 0°	98.11	1.89
Flat, at 20°	98.10	1.90
BD, at 20°	98.08	1.92

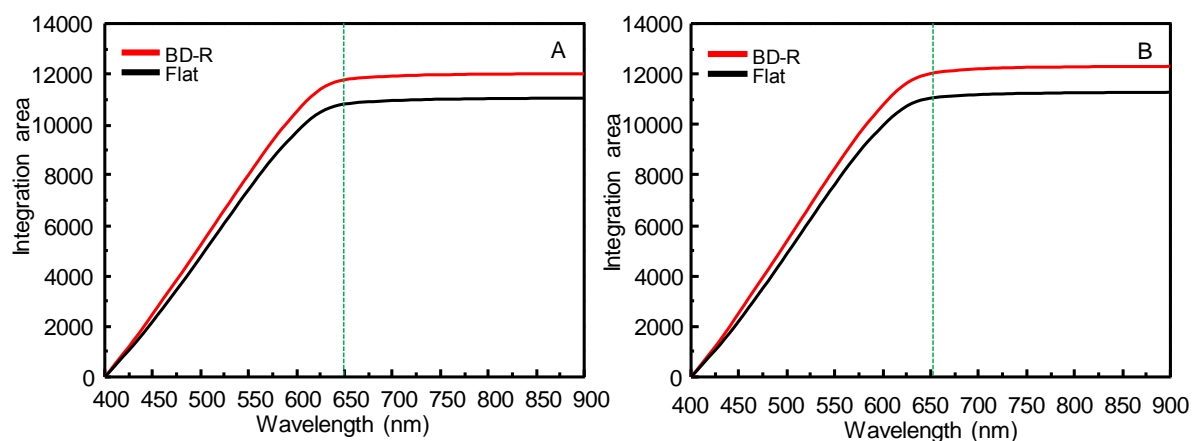


Figure S19 The relationship between the IPCE integration area and scanning wavelength of BD-R solar cell and flat solar cell at the incident angle of (A) 0° and (B) 20° . The solar cells were irradiated by non-polarized light.

Table S6 The percentage of IPCE integration area calculated from the IPCE spectra of BD-R solar cell and flat solar cell at the incident angle of 0° and 20° under illumination of non-polarized light.

Devices	% Integration area (%)	
	400–650 nm	650–900 nm
Flat, at 0°	97.91	2.09
BD-R, at 0°	97.96	2.04
Flat, at 20°	97.97	2.03
BD-R, at 20°	97.65	2.35

VITAE



Name: Mr. Supeera Nootchanat

Address: Sensor Research Unit (SRU), Department of Chemistry,
Faculty of Science Chulalongkorn University

254 Phayathai Road Patumwan Bangkok 10330 Thailand

Tel/fax: (+66)2-218-7585, **E-mail:** magiga_@hotmail.com

Education

- 2008 B.Sc. (1st Class Honours) in Chemistry, Silpakorn University, Nakornphatom, Thailand
- 2008-Present Ph.D. student in physical chemistry at Chulalongkorn University, Bangkok, Thailand
- 2011-Present Ph.D. student in physical chemistry at Niigata University, Niigata, Japan

Advisors

Assoc. Prof. Dr. Sanong Ekgasit (Thailand)

Assoc. Prof. Dr. Akira Baba (Japan)

Research field

1. Synthesis and characterization of metals (gold) nanoparticles
2. Structural-controlled synthesis of metal nanoparticles
3. Application of metal nanoparticles
4. Photovoltaic devices
5. Plasmonic thin film organic solar cells

Instrumental skills

1. Thermo scientific DXR Raman microscope: **administrative user**
2. JEOL JSM-6510A scanning electron microscope equipped with EDS detector: **administrative user**
3. Zeiss Axio Scope.A1 stereomicroscope with dark field adapter, polarized adapter, and DIC

adapter: **administrative user**

4. Princeton applied research Parstat 4000 potentiostat: **administrative user**
5. SII SPA400 scanning probe microscope with NanoNavi station controller: **General user**
6. Shimadzu SPM-9600 scanning probe microscope: **General user**
7. Jasco V-650 spectrophotometer with a photomultiplier tube (PMT) detector: **General user**
8. Nicolet 6700 infrared spectrometer equipped with Continuum FT-IR microscope: **General user**
9. Ocean Optics USB4000 portable UV-visible spectrometer: **General user**
10. Ocean Optics QE65000 portable Raman spectrometer: **General user**
11. Ocean Optics NIR256-2.5 portable NIR spectrometer: **General user**

Publications

1. **S. Nootchanat**, C. Thammacharoen, B. Lohwongwatana, S. Ekgasit, Formation of large H₂O₂-reduced gold nanosheets via starch-induced two-dimensional oriented attachment, RSC Adv., 3, 3707–3716 (2013).
2. **S. Nootchanat**, H. Ninsonti, A. Baba, S. Ekgasit, C. Thammacharoen, K. Shinbo, K. Kato, F. Kaneko, Investigation of localized surface plasmon/grating-coupled surface plasmon enhanced photocurrent in TiO₂ thin films, PCCP, 16, 24484-24492 (2014).
3. H. Ninsonti, K. Hara, **S. Nootchanat**, W. Chomkitichai, A. Baba, S. Phanichphant, K. Shinbo, K. Kato, F. Kaneko, Enhanced Photocurrent Generation at a Spiro-OMeTAD/AuNPs-TiO₂ Interface with Grating-coupled Surface Plasmon Excitation, IEICE Transactions on Electronics, E98C, 104-109 (2015).

Conferences

- 2009 Poster presentation “Green Synthesis of Precious Metal (Ag, Au, Pt, Pd) Nanoparticles” at ChinaNANO 2009, Beijing, **China**
- 2010 Poster presentation “Nanostructure Assembly of Golden Apple Snail’s Egg Shell” at PACCON 2010, Ubon Ratchathani, **Thailand**
- 2010 Poster presentation “Gold Nanoplates prepared by Green Nanotechnology” at Joint symposium on advanced polymers and nanomaterials by Chulalongkorn University - Inha University, Bangkok, **Thailand**
- 2010 Oral presentation “Nanostructure Assembly of Golden Apple Snail’s Egg Shell” at The Science Forum 2010, 11-12 March 2010, Faculty of Science, Chulalongkorn University Bangkok, **Thailand**

- 2011 Poster presentation “Investigation of the Surface Modification of 2-D Gold Nanoplates by the Simple Wet Chemical Method” at The 28th Annual Conference of The Microscopy Society of Thailand, 5-7 January 2011, Chiang Rai, **Thailand**
- 2011 Poster presentation “Structural Evolution of Gold Nanoplates to Gold Nanoflowers Initiated by Hydrogen Peroxide Induced Degradation of Starch” at The Science Forum 2011, 10-11 March 2011, Faculty of Science, Chulalongkorn University Bangkok, **Thailand**
- 2011 Poster presentation “Gold Nanoparticles Modified-2D Gold Nanoplates: Novel SERS Substrates for Chemical Sensing Applications” at 14th Asian Chemical Congress 2011, 5-8 September 2011, Queen Sirikit National Convention Center, Bangkok, **Thailand**
- 2012 Oral presentation “Structural Evolution from Gold Nanoplates to Flower-like Gold Nanostructures” at The 29th Annual Conference of The Microscopy Society of Thailand, 30 January-1 February 2012, Prachuap Khiri Khan, **Thailand**
- 2013 Oral presentation “Gold Nanosheets and Flower-Like Gold Nanostructures: Synthesis and Structural Evolution” at 2013 Niigata Graduate Research Forum, Niigata, **Japan**.
- 2013 Poster presentation “Fabrication and Photocurrent Properties of Gold Nanoparticle-decorated TiO₂ nanocomposite Films” at The 4th International Symposium on Organic and Inorganic Electronic Materials and Related Nanotechnology (EM-NANO 2013), Kanazawa, **Japan**
- 2013 Poster presentation “Fabrication and Photocurrent Properties of Gold Nanoparticle-decorated TiO₂ nanocomposite Films” at The 2013 KJF International Conference on Organic Materials for Electronics & Photonics (KJF-ICOMEPE), Busan, **Korea**
- 2014 Poster presentation “Investigation of Grating-coupled SPR Enhanced Organic Solar Cell fabricated by Nanoimprint Technique” at 11th International Conference on Nano-Molecular Electronics (ICNME 2014), Kobe, **Japan**
- 2014 Poster presentation “Investigation of LSPR and LSPR – grating couple SPR enhanced photocurrent of TiO₂ (P25)” at International Conference on Solid State Devices and Materials 2014 (SSDM 2014), Tsukuba, **Japan**
- 2014 Oral presentation “Investigation of LSPR and LSPR – grating couple SPR enhanced photocurrent of TiO₂ (P25)” at JSAP 75th Autumn Meeting 2014, Hokkaido, **Japan**

Awards

- 2010 Consolation oral presentation award in The Science Forum 2010, Entitled “Nanostructure Assembly of Golden Apple Snail’s Egg Shell”
- 2010 The outstanding poster award in Pure and Applied Chemistry International Conference 2010, Entitled “Nanostructure Assembly of Golden Apple Snail’s Egg Shell”
- 2011 The third prize of poster presentation in The 28th Annual Conference of The Microscopy Society of Thailand, Entitled “Investigation of the Surface Modification of 2-D Gold Nanoplates by the Simple Wet Chemical Method”
- 2011 The second prize of microscope picture competition in The 28th Annual Conference of The Microscopy Society of Thailand
- 2011 Consolation poster presentation award in The Science Forum 2011, Entitled “Structural Evolution of Gold Nanoplates to Gold Nanoflowers Initiated by Hydrogen Peroxide Induced Degradation of Starch”
- 2011 The Best prize in Sci & Tech Innovation and Sustainability Award: Innovative Chemical Processes & Produce 2011, Entitled “Gold Nanocrystals 99.99% for Cosmetic and Thai spa business”
- 2012 The third award in oral presentation in The 29th Annual Conference of The Microscopy Society of Thailand, Entitled “Structural Evolution from Gold Nanoplates to Flower-liked Gold Nanostructures”
- 2012 Gold medal in 40th International Exhibition of Inventions of Geneva 2012, Entitled “Reflective Gold Nanocrystals”
- 2013 The Honor award from the senate of Thailand for using of scientific knowledge to benefit Thai.